Lithos
April 2023, Volume 442-443, Pages 107084 (18p.)
https://doi.org/10.1016/j.lithos.2023.107084 https://archimer.ifremer.fr/doc/00821/93297/

Archimer
https://archimer.ifremer.fr

Hydrous fluids down to the semi-brittle root zone of detachment faults in nearly amagmatic ultra-slow spreading ridges

Bickert Manon [1,*], Cannat M. [2], Brunelli D. [1,3]

[1] Dipartimento di Scienze Chimiche e Geologiche, Università di Modena e Reggio Emilia, Modena, Italy
[2] Université Paris Cité, Institut de Physique du Globe de Paris, CNRS-UMR, 7154, France
[3] IGAG-CNR, Istituto di Geologia Ambientale e Geoingegneria, Rome, Italy

* Corresponding author : Manon Bickert, email address : Manon.Bickert@ifremer.fr

Abstract :

At the Eastern part of the Southwest Indian Ridge (SWIR), plate divergence is accommodated by large offset normal faults, also called detachment faults, that exhume mantle-derived rocks on the seafloor. A third of the ultramafic samples dredged on- and off-axis in this nearly amagmatic ridge setting present amphibole-bearing secondary mineralogical assemblages indicative of hydration, and for the most part predating the growth of serpentine minerals. The deepest evidence of hydration is the occurrence of small amounts of syn-kinematic amphibole in microshear zones with strongly reduced grain size, which record deformation at high stress and high temperatures (>800 °C) at the root zone of the detachment. The composition of these amphiboles is consistent with a hydrothermal origin, suggesting that seawater derived fluids percolated down to the root of detachment faults, at the Brittle-Ductile Transition (BDT). We propose that the constant exhumation of new mantle material to the seafloor, and the limited lifetime of each detachment (1–3 Myrs) prevent a more pervasive deep hydration of mid-ocean ridge detachment root regions, as proposed at transform fault plate boundaries.

Highlights

► Synkinematic amphiboles crystallized at the root of Eastern SWIR axial detachments. ► Seawater-derived fluids percolate along the detachment down to the BDT. ► Variations in amphibole composition are controlled by the protolith. ► Deep fluid percolation is controlled by detachment fault activity.

Keywords : Southwest Indian Ridge, plate boundary faulting, deformation processes, hydration, amphiboles, fluid-rock interaction, brittle-ductile transition

Please note that this is an author-produced PDF of an article accepted for publication following peer review. The definitive publisher-authenticated version is available on the publisher Web site.

Journal Pre-proof

1. Introduction

At slow spreading-ridges, large offset normal faults exhume serpentinized mantle-derived rocks on the seafloor (Cann et al., 1997; Cannat, 1993; Escartín et al., 2008; Sauter et al., 2013; Smith et al., 2006; Tucholke et al., 2008). These faults, also called detachment faults, dip steeply at depth (Chen et al., 2023; deMartin et al., 2007; Parnell-Turner et al., 2017) and emerge at low angle on the seafloor (Cannat et al., 2019; Smith et al., 2006), conferring them a convex-downward profile. Detachment faults root into ductile fresh peridotites in the deep axial lithosphere, and bring these rocks to shallower depths, where seawater-derived fluids circulate through cracks and fissures and along grain boundaries, leading to extensive hydration and alteration.

Fracturing associated with the development of faults is a key mechanism that focuses fluid flow through the lithosphere at the axis of slow-spreading ridges. The deep microseismicity recorded at slow spreading ridges suggests that detachment faults root at depths down to 12 km at the Mid-Atlantic Ridge (MAR; de Martin et al., 2007; Parnell-Turner et al., 2020) and to 15-20 km at the Southwest Indian Ridge (SWIR; Chen et al., 2023; Grevemeyer et al., 2019; Schlindwein and Schmid, 2016; Yu et al., 2018).

The permeability created by networks of microfractures formed due to cooling of the exhuming mantle, close to the brittle-ductile transition (BDT), may also enhance the hydrothermal alteration of peridotites (de Martin et al., 2004; Fruh-green et al., 2004; Rouméjon and Cannat, 2014). As fluids interact with the exhuming mantle, hydrous minerals form, such as serpentine, brucite, talc, chlorite, and amphibole ranging from tremolite to Mg-hornblende and pargasitic compositions (Fruh-green et al., 2004; Fumagalli et al., 2009). Experimental studies have related these mineralogical assemblages to specific temperature ranges (Bach et al., 2004; Escartin et al., 1997; Klein et al., 2009). Hydrated assemblages, particularly those rich in phyllosilicates, are generally weaker than the anhydrous paragenesis, especially olivine, and therefore decrease the strength along the fault ($\mu<0.6$; Escartín et al., 2003). Hydration reactions are indeed observed to control strain localization in the upper brittle lithosphere at the axis of slow-spreading ridges, where hydrothermal alteration is pervasive and and where the ultramafic rocks are extensively serpentinized (Boschi et al., 2006; Escartin et al., 2003; Picazo et al., 2012; Schroeder and John, 2004). Deeper in the lithosphere, below the serpentinized domain, both higher confining pressure and temperature lead to the transition from brittle to ductile deformation and are expected to prevent vigorous hydrothermal circulation.

The presence of hydrous fluids in peridotites deforming at BDT conditions is, however, supported by several petrological studies reporting syntectonic Mg-hornblende to pargasitic amphiboles in deformed peridotites from oceanic detachment faults (Albers et al., 2019; Bickert et al., 2021; Boschi et al., 2006; Patterson et al., 2021; Picazo et al., 2012; Schroeder and John, 2004), oceanic transform faults (Cannat and Seyler, 1995; Cipriani et al., 2009;

Journal Pre-proof

Kakihata et al., 2022; Kohli and Warren, 2020; Prigent et al., 2020), orogenic massifs and ophiolites (Hidas et al., 2016; Prigent et al., 2018; Vieira Duarte et al., 2020). Petrographically, these amphiboles predate serpentine, hence suggesting their crystallization to occur at temperatures higher than the serpentine stability limit (Schroeder & John, 2004; Boschi et al., 2006; Fumagalli et al., 2009; Cannat et al., 2012; Picazo et al., 2012; Patterson et al., 2021). Several microstructural studies also show that these amphiboles formed in a semi-brittle rheology composed of brittle orthopyroxene and mostly crystal-plastic olivine, which would be consistent with deformation conditions close to the BDT, at the root zone of trans-lithospheric faults (Cannat and Seyler, 1995; Kohli and Warren, 2020; Prigent et al., 2020; Vieira Duarte et al., 2020). The origin of the fluids involved has also been investigated, and proposed to be primarily hydrothermal (Patterson et al., 2021; Prigent et al., 2020; Vieira Duarte et al., 2020).

Here, we study high-temperature amphiboles found in ultramafic samples dredged in two nearly-amagmatic corridors at the eastern Southwest Indian Ridge (SWIR, 62-65°E; Cannat et al., 2006; Sauter et al., 2013). This area is characterized by a very low melt supply and has an axial seismogenic lithosphere at least 15 km-thick (Chen et al., 2023; Grevemeyer et al., 2019; Schlindwein and Schmid, 2016). Successive detachment faults with flipping polarity (flip-flop detachments; Reston, 2018; Reston & McDermott, 2011) accommodate most of the plate divergence (Sauter et al., 2013), which contrast with the longer-lived detachments forming corrugated surfaces on one flank of the ridge only, in more magmatic and faster spreading contexts (Cann et al., 1997; Escartín et al., 2017; MacLeod et al., 2002; Smith et al., 2006). Rocks recovered along the steep footwalls of these successive detachment faults are mainly variably serpentinized peridotites, with minor amounts of basalts and gabbros (Fig. 1; Sauter et al., 2013; Rouméjon et al., 2015). The earliest lithospheric deformation recorded in the variably serpentinized samples collected in this region of the SWIR combines crystal-plastic and brittle mechanisms, with anastomosing zones of grain size reduction (GSR) formed under high stress (80-270 MPa) and high temperature conditions (>800°C; Fig. 2a, 3; Bickert et al., 2020; 2021). This heterogeneous high stress deformation has been interpreted as characteristic of the root zone of the axial detachment faults (Bickert et al., 2021) and is very different from the high temperature, low stress deformation microstructures expected in the asthenospheric mantle or in the deep lithosphere, and recorded by ultramafic samples from more magmatic detachments (Albers et al., 2019; Ceuleneer and Cannat, 1997; Harigane et al., 2016; Seyler et al., 2007). Among samples with GSR, a few contain small amounts of amphibole that crystallized during GSR formation (Fig. 3b-d). Our primary objective here is to better constrain the origin of the fluids that crystallized these amphiboles: are they derived from small amounts of water in the residual lherzolitic mantle or formed from hydrous magmatic fluids? Are they evidence for deep penetration of seawater-derived fluids? To this aim, we provide a detailed textural, microstructural, and chemical analysis of these amphiboles, and compare these results with those obtained from GSR-free amphibole-bearing peridotite samples from the same region, in which amphiboles are more clearly of hydrothermal origin. This comparison leads us to discuss the suite of hydration processes in the magma-poor root of the eastern SWIR flip-flop detachment faults, and the similarities and differences with hydration processes that have been documented down to similar to greater depths in the root zone of oceanic transform faults (Brunelli et al., 2020; Cipriani et al., 2009; Prigent et al., 2020).

2. Diversity and estimated abundance of eastern SWIR amphibole-bearing ultramafic rocks

Journal Pre-proof

Journal Pre-proof

Of the 33 dredges of the *Smoothseafloor* cruise (Sauter et al., 2013), 24 recovered amphibole-bearing, variably serpentinized ultramafic samples (Fig. 1; Table A1). Overall, amphibole-bearing peridotites represent 34% of the samples collected from these 24 dredges (Table A2). Peridotites with amphibole-bearing GSR zones were recovered in only 4 dredges from the western nearly amagmatic corridor (DR08, DR10, DR14, DR17; Fig. 1 and Table A2). The deformation of the primary minerals in these samples has been characterized in a previous study (Bickert et al., 2021), finding that GSR zones develop in peridotites that show the highest rates of a high stress (80 to 270 MPa), relatively high temperature (~800–1000 °C) deformation episode. The variable degrees of this heterogeneous deformation were described in four textural types, from A0 for the least deformed (kinked pyroxenes, weakly deformed olivine, no GSR), to A3 for the most deformed (kinked pyroxenes, strongly plastically deformed olivine, continuous GSR zones; Table A3).

In addition to samples with amphibole-bearing GSR zones (Fig. 2a and 3), we identified 3 other types of amphibole-bearing ultramafic samples: amphibole-bearing melt-impregnated ultramafic samples (Fig. 2b), amphibole mylonites (Fig. 2c), and amphibole-bearing serpentinized peridotites (Fig. 2d).

Amphibole-bearing, melt-impregnated samples occur in 21 dredges (Fig. 1; Table A2) and are interpreted as resulting from the hydration of peridotites impregnated by basaltic melts in the plagioclase stability field (Paquet et al., 2016). In hand specimen, amphibole-bearing domains are grey to dark, commonly foliated, and clustered along pyroxenes (Fig. 2b).

The amphibole mylonites are strongly foliated, commonly showing brown amphibole porphyroclasts with evidence of rolling structures (σ-shapes; Fig. 2c), and domains recording a higher strain with fewer porphyroclasts and a finer-grained matrix (Fig. 2c). Amphibole mylonites occur were sampled in only 3 dredges (DR27, DR33 and DR34; Fig. 2c, Table A2).

Journal Pre-proof

Dredges 33 and 34 sampled a moderately magmatic, corrugated detachment footwall (Fig. 1; Cannat et al., 2009).

The fourth type of amphibole-bearing peridotites is composed of strongly serpentinized peridotites, which is relatively common and found in 16 dredges (Fig. 1; Table A2). In hand specimen, amphibole-bearing serpentinized samples show a dark greenish color (Fig. 2d). Olivine is fully serpentinized and/or replaced by oxidized minerals, while pyroxenes are partially replaced by amphibole (Fig. 2d).

Overall, samples with amphibole-bearing GSR zones account for only 2% of the ultramafic samples recovered by dredging in the study area (Table A2). Amphibole-bearing melt-impregnated peridotites, amphibole mylonites and amphibole-bearing serpentinized peridotites respectively count for 20%, 2% and 10% (Table A2).

Journal Pre-proof

3. Sampling and analytical methods

We selected 28 amphibole-bearing ultramafic samples for detailed petrographic and geochemical analysis (Table A3) among the four types of amphibole-bearing samples listed in Table A2: (1) 8 samples with amphibole-bearing GSR zones, in which amphibole recrystallized together with the primary minerals of the peridotite (Fig. 3); (2) 7 amphibole-bearing melt-impregnated samples, in which amphibole recrystallized together with olivine and chlorite (Fig. 4); (3) 4 amphibole mylonites (Fig. 5a-c), and (4) 9 amphibole-bearing serpentinized peridotites in which amphibole replaced primary minerals in veins or in microshear zones (Fig. 5d-f).

Microstructures were studied in thin sections using both optical polarizing and scanning electron microscopy (SEM). Electron backscattered images obtained by SEM were used to characterize the fine-grained recrystallized assemblages, especially amphiboles in GSR zones that were often too small to be optically identified.

We also performed electron microprobe analysis to measure major elements concentrations of amphibole and primary minerals (olivine, orthopyroxene, clinopyroxene, spinel) using a Cameca SX-100 electron microprobe (CAMPARIS service, Paris). The acceleration voltage was fixed at 15 kV and beam current at 10 nA. The spot size was 1-2 µm. Counting time was 10 s. Representative major element compositions of amphibole are shown in Table 1. The whole dataset used for Fig. 6-9 is accessible in the supplementary material of this study (Tables A4-A6) and was partially published in Bickert et al. (2020) for pyroxenes and spinel composition, and in Bickert et al. (2021) for composition of amphiboles in GSR zones.

4. Results

4.1. Microstructures and amphibole composition in the amphibole-bearing ultramafic samples

Our first objective is to provide microstructural and chemical constraints on the nature of the fluids driving amphibole crystallization in the GSR zones (Fig. 3). For this we compare both the microstructures (Fig. 3-5) and the composition of these synkinematic amphiboles (Fig. 6a-b) with those of amphiboles present in the three other amphibole-bearing types (Fig. 6c-d, 7-8).

4.1.1. Peridotites with amphibole-bearing GSR zones

Journal Pre-proof

Journal Pre-proof

Peridotites with amphibole-bearing GSR zones are spinel-bearing harzburgites and lherzolites. Primary mineralogy is composed of large olivine and orthopyroxene grains (up to 2 cm in size; Bickert et al., 2021) with various amounts of clinopyroxene and spinel grains.

Anastomosing zones of GSR mainly develop at contact between olivine and orthopyroxene porphyroclasts (Fig. 3a, c). The neoblasts' grain size ranges from 1.5 to 84 µm (Bickert et al., 2020, 2021). The mineralogy of the recrystallized assemblage varies depending on the porphyroclasts at contact with: polymineralic (olivine, orthopyroxene, spinel, minor clinopyroxene and amphibole) along orthopyroxene porphyroclasts (Fig. 3a-d), or nearly monomineralic (olivine and minor spinel and amphibole) near olivine porphyroclasts (Fig. 3e).

In polymineralic GSR zones, minute amounts of colorless polygonal to prismatic amphibole crystals coexist with neoblasts of olivine, orthopyroxene and spinel (Fig. 3b, d). The polygonal shapes of these amphiboles indicate a textural equilibrium with the other recrystallized phases (Fig. 3b, 3d). In a few samples, we also observed discordant veins of undeformed prismatic amphibole crosscutting all microstructures, including the GSR zones, with sharp contacts (Fig. 3e-f).

Compositionally, amphibole in GSR zones are mostly edenites to Mg-rich hornblendes, with few tremolites (Si values: 6.32 - 7.76, $(Na+K)_A$ values: 0.1-0.7; Fig. 6a; Table 1). One sample contains synkinematic pargasitic amphiboles (SMS-DR17-4-31, Si values of 6.32 – 6.51, $(Na+K)_A$ values of 0.3-0.7; Figs. 6a, 7a). TiO_2 content is overall low (< 0.72 wt. %), mostly < 0.5 wt. % (Fig. 6b; Table A3). Mg# values range from 87.5 to 95.5 (Fig. 6b). Chlorine concentrations range from below the detection limit to 0.33 wt. % (Tables 1, A4). The intra-sample variability of amphibole composition spans the whole pargasite to tremolite trend (Figs 7a-b), with small variations related to the minerals micro-aggregation: amphibole in

Journal Pre-proof

olivine-rich zones have more depleted alkaline and iron concentrations (close to tremolitic composition) than in polymineralic zones (Figs. 7a-b). Amphibole from veins cutting the initial mineralogy globally follow the same trend, suggesting a similar origin as amphibole in GSR zones, despite a slight enrichment in alkali and iron (Figs. 7a-b, 7e; Table 1).

4.1.2. Amphibole-bearing, impregnated ultramafic samples

Amphibole-bearing, melt-impregnated ultramafic samples are spinel-bearing harzburgites and lherzolites with porphyroclastic textures (Table A3). Olivine is mostly preserved and weakly deformed, with undulose extinction and subgrain boundaries (Fig. 4a-b). By contrast, no orthopyroxene porphyroclasts nor melt impregnation veins are preserved in these samples; plagioclase is absent. Instead, oriented, fibrous to tabular, amphibole and bluish chlorite crystals form irregularly branched microshear zones that dissect the primary mineralogy, creating angular olivine-rich clasts (Fig. 4a-b). At contact with the amphibole and chlorite microshear zones, amphibole and olivine locally recrystallize together in polygonal grains, with a much coarser grain size than in the GSR zones (70-160 µm; Fig. 4b, d-e). Amphibole also locally crystallizes along corroded olivine grain boundaries (Fig. 4d-e). Serpentine is in every case a later alteration product, forming veins that crosscut both the olivine-rich clasts and the amphibole-chlorite domains (Fig. 4a, c).

Figure 4c shows a detail of a sample with amphibole-rich bands up to 8 mm-thick (Fig. 2c), composed of deformed, colorless oriented amphibole porphyroclasts and recrystallized amphibole grains, and defining a foliation (Fig. 4c). These amphibole-rich bands are interlayered with polymineralic domains composed of altered pyroxene porphyroclasts in a matrix of fine-grained amphibole and chlorite. Late microshear zones of deformed chlorite and serpentine enclose elongated relicts of olivine and of deformed spinel porphyroclasts, forming alteration haloes around spinels (Fig. 4c).

Compositionally, amphibole grains from amphibole-bearing melt-impregnated ultramafic samples also have pargasite to Mg-hornblende compositions, with a wider range of Si (6.35 – 7.96) and $(Na+K)_A$ values (0 – 0.93) than the amphiboles in GSR zones (Fig. 6c). Yet, they define a different trend than amphiboles in GSR zones, with higher $(Na+K)_A$ values at a given Si content (Fig. 6c). TiO_2 and Mg# contents are quite similar between the two types (< 0.57 wt. % and 86.7 – 96.6, respectively; Fig. 6d). Chlorine concentrations are overall lower than for amphibole in GSR zones (<0.17 wt. %; Tables 1, A4). As for amphibole in the GSR zones, amphibole composition varies slightly according to the nature of minerals phase at contact with, the few tremolites being located next to olivine grains (Figs. 7f-h; Table 1).

4.1.3. Amphibole mylonites

In amphibole mylonites, the initial mineralogy is totally overprinted by hydrous minerals, which makes difficult the identification of the initial protolith. Yet, the high amounts of chlorite and/or talc in the matrix (Fig. 5a, c) suggest that the protolith was a mixture of peridotite and gabbro (Albers et al., 2019; Bach et al., 2012; Boschi et al., 2006; Picazo et al; 2012). Amphibole mylonites show alternation of amphibole-rich domains with polymineralic domains (Fig. 5a-b). One sample shows a microshear zone in a large clinopyroxene grain, with recrystallization of both clinopyroxene and brown amphibole (Fig. A1). Amphibole-rich domains are mainly composed of prismatic brown amphibole porphyroclasts (Fig. 5a), while polymineralic domains are mostly composed of very small grains of amphibole, bluish to grey chlorite and talc (Fig 5a, c). Brown amphibole porphyroclasts, and former pyroxenes replaced by amphibole commonly form syntectonic rolling structures (δ- to σ-types), with pressure shadow rims composed of acicular amphibole ± chlorite ± talc (Fig. 5a, c). Spinel relicts are rare but present in several samples. Post-deformation veins of talc are common (Fig 5c).

As for the two first amphibole-bearing types, most amphiboles in these mylonites have edenitic to Mg-rich hornblende compositions (Fig. 8a-b). Yet, they differ by their high TiO_2 contents, which are mostly > 1 wt. % (0.27 - 3.64 wt.%; Fig. 8b; Table 1). Samples from the DR33 (from an exposed corrugated footwall; Cannat et al., 2006) are the most enriched in alkali and iron (Mg# < 83), while amphibole from the two other samples (DR27 and DR34) are more magnesian (Mg# of 85–94; Fig. 8b). Chlorine concentrations range from below the detection limit to 0.25 wt. % (Tables 1, A4). Amphibole composition in these mylonites also show a slight variability depending on the microstructures, with deformed amphibole porphyroclasts having higher TiO_2 and Al contents (> 1 wt.% and 1 a.p.f.u respectively), and lower Si < 7 a.p.f.u. (Fig. 8a-b and Table A3) than smaller amphiboles from polymineralic domains.

4.1.4. Amphibole-bearing serpentinized ultramafic samples

In amphibole-bearing serpentinized ultramafic samples, amphibole replaces pyroxenes (Fig. 5d-e), or occurs as fibrous crystals in late micro shear zones (Fig. 5e), or in the serpentinized groundmass (Fig. 5f; Table 1). Olivine is fully replaced, either by serpentine, or by oxide-bearing mineral assemblages (Fig. 5a). Chlorite when present postdates amphibole formation and is associated with serpentine in late microshear zones (Table A3). Serpentine products form veins that crosscut amphibole-rich domains (Fig. 5d-f).

Compositionally, amphibole in these extensively serpentinized samples is mostly tremolitic, with a few Mg-hornblendes (Fig. 8c; Table 1). Si values are mostly high (7.28-8 a.p.f.u.) with low $(Na+K)_A$ concentrations (< 0.41). All amphibole grains have low TiO_2 content (< 0.32 wt%) and Mg# shifting to higher values (94.9 - 97.8) (Fig. 8d). Chlorine concentrations do not exceed 0.13 wt. % (Tables 1; A4).

4.2. Amphibole composition and the primary mineralogy of amphibole-bearing samples

Our objective here is to identify any potential control on the protolith mineralogy on amphibole composition. For this purpose, we compare the composition of spinel and pyroxene relicts in the selected amphibole-bearing samples with existing data from the Eastern SWIR (Fig. 9; Tables A5-A6). Spinel and clinopyroxene porphyroclasts from the selected samples cover the whole compositional variations documented in peridotites from the same region by Seyler et al. (2003) and Paquet et al. (2016) (Fig. 9).

Spinel Mg# and Cr# are negatively correlated following the global trend of the abyssal peridotites (Dick and Fisher, 1984) (Fig. 9a). The four types of amphibole-bearing samples plot in different parts of the trend: amphibole mylonites have the most Cr-rich spinel (Cr# values of 42.5-43.6, Fig. 9a), also enriched in iron (Mg# <50; Fig. 9a) and in TiO_2 (> 0.15 wt%; Fig. 9b). Spinel from amphibole-bearing, melt-impregnated ultramafic samples show higher Mg# (53.6 – 61.3) at lower Cr# values (31.7-39.4; Fig. 9a). Spinel TiO_2 content is in the same range as in amphibole mylonites (Fig. 9b). Plagioclase-bearing peridotites from this region of the SWIR have similar spinel composition to these two amphibole-bearing types, consistent with a protolith resulting from chemical interactions between peridotite and a variably evolved melt (Fig. 9a-b; Paquet et al., 2016). By contrast, peridotites with amphibole-bearing GSR zones have spinel with lower Mg# and Cr# values (60.9 - 71.3 and 21.7-33.8, respectively; Fig. 9a), and with TiO_2 contents < 0.15 wt.% (Fig. 9b). The rare spinel relicts from amphibole-bearing serpentinized ultramafic samples have similar compositions, within the range of other residual peridotite samples from the eastern SWIR (amphibole-free GSR bearing samples from the *Smoothseafloor* dredges, and other samples studied by Seyler et al., 2003; Fig. 9a-b). Overall, spinel and amphibole Mg# show a similar decreasing trend with increasing the degree of melt-impregnation (Fig. 9b, Fig. 10b, d).

Compositions of clinopyroxene porphyroclasts in samples with amphibole-bearing GSR zones covers the entire range of clinopyroxene composition recorded in other residual peridotites from the eastern SWIR, including those with amphibole-free GSR zones (Figs. 9c-d). Due to the extent of alteration, clinopyroxene composition was measured in only one amphibole-bearing melt-impregnated ultramafic sample and one amphibole mylonite. Clinopyroxene from the amphibole-bearing melt-impregnated ultramafic sample plots at the lower Cr_2O_3 (average of 0.70 wt.%), higher Al_2O_3 (7.43 wt.% on average) end of the trend defined by residual peridotites from the Eastern SWIR, and at similar Mg# values (90.2 on average; Figs. 9c-d). By contrast, clinopyroxene from the amphibole mylonite is more depleted in Al_2O_3 and Cr_2O_3 contents (3.08 wt.% and 0.29 wt.%, respectively; Fig. 9c), with lower Mg# (82.9; Fig. 9d). Clinopyroxene in amphibole-bearing serpentinized ultramafic samples were too altered to be measured. Overall, clinopyroxene TiO_2 contents decrease with increasing Mg# and Cr#, as also observed by Seyler et al. (2003; Fig. 9c-d; Table A6).

5. Discussion

The objective of this study is to better constrain the extent and the distribution of mantle hydration along axial detachments at the Eastern SWIR, below the domain affected by pervasive hydrothermal circulation and by serpentinization (Fig. 11). Because this region of the SWIR has a very low melt supply, plate divergence is mostly accommodated by slip

Journal Pre-proof

along these detachment faults (Cannat et al., 2006; Sauter et al., 2013), which therefore represent the actual plate boundary (Fig. 11a).

The occurrence of small amounts of amphibole in GSR zones is evidence for the presence of small amounts of hydrous fluids in the root zone of these plate boundary faults at and near the BDT (Bickert et al., 2020; 2021). Microseismicity data (Chen et al., 2023) helps constrain this BDT region to depth >15 km. Compared to oceanic transform faults (OTFs), the other category of plate boundary faults at mid-oceanic ridges (Fig. 11b), axial detachment faults are both generally shorter lived (< 4 Myrs; Tani et al., 2011), and associated with continuous exhumation of deeply-derived material. These characteristics probably translate into substantial differences in the degree of deformation and hydration between the two categories of plate boundary faults.

Journal Pre-proof

5.1. A seawater-derived origin for fluids that percolate down to the root zone of eastern SWIRaxial detachment faults

In samples from the Eastern SWIR, amphibole is present in various mineralogical assemblages: (1) synkinematic with olivine ± orthopyroxene ± clinopyroxene + spinel in GSR zones (Fig. 3b-d); (2) with olivine and/or chlorite in impregnated ultramafic samples (Fig. 4a-b); (3) with chlorite ± talc in amphibole mylonites (Fig. 5a-c); (4) predating serpentine ± chlorite in the most serpentinized ultramafic samples (Fig. 5d-e). These observed mineralogical assemblages could indicate a relative chronology through exhumation, with increasing hydrous fluids content upward: very localized hydration in the GSR zones, at high temperatures (>800°C) at the root zone of detachments, close to the BDT; to more pervasive hydration conditions under greenschist facies conditions in the amphibole-bearing serpentinized peridotites. Serpentinization appears to postdate most amphibole-bearing microstructures in this whole suite, and preferentially affects olivine, leaving pyroxenes relicts except in the most extensively serpentinized samples, which suggest moderate temperatures of serpentinization (T <400°C; Bach et al., 2004; Klein et al., 2009), consistent with the oxygen isotope results of Rouméjon et al. (2015).

The amphiboles in the studied suite of rocks can result from (1) magmatic infiltrations or dikes in the peridotite (Cannat & Seyler, 1995; Cipriani et al., 2009; Schroeder & John, 2004); (2) sea-water, suggesting deep percolation of hydrothermal fluids in the mantle lithosphere, down to the root of the fault at the BDT (Cannat & Seyler, 1995; Kohli & Warren, 2020; Prigent et al., 2020; Vieira Duarte et al., 2020); or (3) crystallizing from small amounts of water in the residual lherzolitic mantle (Alard et al., 2022; Le Roux et al., 2021; Schmädicke et al., 2018).

It is unlikely that the amphibole in GSR zones crystallized from hydrous fluids trapped in mantle primary minerals. Water dissolved in residual mantle paragenesis would be close to or lower than the average mantle source, i.e. circa 200 ppm in olivine (Urann et al., 2017), which is a too low amount to the formation of monomineralic amphibole veins crosscutting the microstructures (Fig. 3e-f) with similar composition as those in GSR zones (Fig. 7a-e).

Then, if amphiboles have a purely magmatic origin, they would be expected to have a pargasitic composition with high Fe, Ti and Na content, as described for amphiboles in samples from the MAR (Fig. 10a-b; Albers et al., 2019; Picazo et al., 2012). This is the case for some amphibole in the amphibole mylonites, in which Ti-rich brown amphibole porphyroclasts (Fig. 5c, 8b) have compositions close to those in amphibole-bearing samples from the MAR at 15°N (Fig. 10a-b) and from SWIR gabbros (Dick et al., 2002; Ozawa et al., 1991; Paquet et al., 2016). Yet, in the same samples, the subsequent replacement of primary minerals, including the Ti-rich amphiboles, coupled with the evolution of the mineralogical assemblage (tremolitic to edenitic amphibole + chlorite + talc) also indicate a hydrous fluid-dominated alteration regime, under greenschist conditions (Jöns et al., 2010; Klein et al., 2015), which is in favor of a hydrothermal fluid circulation.

Amphibole from GSR zones have edenitic to Mg-hornblende compositions, with low TiO_2 content (<1wt. %; Fig. 6b). These compositions are closer to those of amphibole interpreted as derived from seawater percolation in peridotites from OTFs (Fig. 10c-d). In addition, the similarity of amphibole composition in GSR zones and in the other amphibole-bearing types, that are of more clear hydrothermal origin, point to a common hydrothermal origin (Fig. 10). The initial mineralogical assemblage of Olivine + Orthopyroxene ± Clinopyroxene + Cr-rich spinel, typical of residual peridotites (Fig. 9), is also consistent with simple hydration of peridotites, at temperatures > 650°C, which would lead to a transition from granulite to amphibolite facies, in which pyroxenes are consumed to form amphibole (Cipriani et al., 2009; Spear, 1981; Vieira Duarte et al., 2020). Amphibole crystals in GSR zones and to a lesser extent in melt-impregnated ultramafic samples are indeed in textural equilibrium with primary minerals (olivine, orthopyroxene, spinel; Fig. 3b, d; 4b). However, the low abundance of amphibole in GSR zones, the highly localized distribution of hydrous minerals along zones of high strength contrasts such as orthopyroxene boundaries and GSR zones (Fig. 3a-c; 4c-d), coupled with the incomplete replacement of primary minerals, suggest that hydration was very limited.

Limited hydration in amphibole-bearing GSR zones and in the melt-impregnated ultramafic samples is consistent with the intrasample variability of amphibole composition driven by the minerals in contact (Fig. 7).(Fig. 7), suggests that fluid composition was buffered by the protolith. This variability, and the strict localization of hydrous minerals along high strength zones, point to a rock-dominated hydration at low water-rock ratios. We

Journal Pre-proof

thus propose that local fluid composition, and the resulting amphibole composition were buffered by the protolith: lherzolites to harzburgites for amphibole in the GSR zones; and mixture of residual peridotite and gabbroic impregnations and dikelets for amphibole in melt-impregnated samples. The latter have similar microstructures, alkaline contents and spinel iron enrichment to hydrothermally altered melt-impregnated peridotites from the MAR (Fig. 10a, c; Albers et al., 2019; Jöns et al., 2010; Picazo et al., 2012). The correlation between spinel Mg# and amphibole Mg# for the four amphibole-bearing types, with varying degrees of melt-impregnation (Figs. 9b, 10b), is consistent with fluid composition being buffered by the protolith, as variably melt-impregnated domains are then replaced by amphibole (Figs. 4-5). Therefore, amphibole composition, deriving from primary minerals, would reflect the processes that have affected the protolith itself, such as the interaction of more or less evolved melts with the host peridotite, at high temperature (Paquet et al., 2016).

5.2. Detachment-related deformation and bidirectional fluid flow

Microstructural and compositional observations in amphibole-bearing SWIR samples allow to reconstruct deep fluid flow along axial detachment faults in a magma-poor plate divergence context (Fig. 11a). At depth, brittle fracture and shear zones forming the detachment grade into a system of anastomosing, crystal plastic to semi-brittle shear zones (Fig. 11a, c; Bickert et al., 2021). This moving anastomosed network allows the exhumation of rocks deformed in high strain zones at relative high P-T conditions to shallower depths and pressures. On the one hand, these microfractures act as fluid pathways for small amounts of seawater-derived fluids that percolate down to the BDT domain. In addition to brittle microstructures, mineral scale heterogeneity, such as between brittle orthopyroxene

Journal Pre-proof

and dominantly plastic olivine, can create small-scale stress concentrations that will help localize strain, favoring fluid circulation and further focusing deformation (Bickert et al., 2021; Dygert et al., 2019; Ismail et al., 2021; Lopez-Sanchez et al., 2021).

On the other hand, magmatic fluids episodically move up along the deformation system (Fig. 11c), resulting in the melt-impregnated and gabbro injected ultramafic samples described by Paquet et al. (2016). In amphibole-bearing melt-impregnated ultramafic samples, the olivine-rich clasts (Fig. 4a-c) may have resulted from local melt injections, as the peridotite entered into the brittle part of the axial lithosphere (Fig. 11c; Albers et al., 2019; Picazo et al., 2012). The syn-recrystallization of olivine and amphibole neoblasts (Fig. 4a-b, d-e), nonetheless suggests that hydration of these gabbroic dikelets started during the late stages of the high stress semi-brittle deformation affecting primary minerals, at temperatures <750°C (Fumagalli et al., 2005). It is worth noting that no massive gabbroic sequences were recovered at the Eastern SWIR, but rather small dikelets or parts of dikes in contact with peridotites (Paquet et al., 2016). This is in accordance with the very low magma budget of this region of the SWIR and differs from other slow and ultraslow locations where large gabbroic bodies, with extensive ductile strain have been drilled in detachments footwalls (Cannat, 1991; Hansen et al., 2013).

As the rock material is exhumed into shallower depths, hydration becomes more pervasive, eventually switching from a rock-dominated to a fluid-dominated alteration regime (Fig. 11d). Samples altered under greenschist facies conditions, such as amphibole-bearing ultramafic samples and mylonites, show higher proportions of low temperature hydrous minerals that are not only focused along zones of high strength contrasts, but also occur in the groundmass (Fig. 5d-f). As exhumation proceeds, significant shear stresses affect the detachment but also its footwall (Lavier et al., 1999; Sandiford et al., 2021). Rouméjon et al. (2014) proposed that initial microfracturing, providing pathways for hydrous fluids and leading to the serpentinization mesh texture, form in response to tectonic stresses combined with peridotite cooling from 800°C to 400°C. The generation of an interconnected porosity through more pervasive cracking, in part due to serpentinization-induced volume change, would characterize the hydrothermal domain. In this domain, the alteration of magmatic minerals and of gabbro-infiltrated peridotite into chlorite- and talc-bearing assemblages, which are weaker than serpentine, locally facilitates strain localization (Boschi et al., 2006; Escartín et al., 2003; Picazo et al., 2012; Schroeder and John, 2004).

5.3. Implications for deep fluid percolation along oceanic plate boundaries

Mg-rich hornblende amphiboles similar to those described here have been observed in ultramafic samples from other magma-starved ridges, active or fossil (Boschi et al., 2006; Cannat et al., 2009; Escartín et al., 2003; Patterson et al., 2021; Picazo et al., 2012; Schroeder and John, 2004; Vieira Duarte et al., 2020), but also along active transform faults such as Shaka and Vema (Cipriani et al., 2009; Kohli et al., 2019; Prigent et al., 2020; Fig. 10c-d). In both contexts, they have been interpreted as resulting from interaction of mantle-derived rocks with limited quantities of seawater-derived fluids that percolated down to the BDT zone (i.e. the root zone of the faults), promoting fluid-assisted deformation (Prigent et al., 2020; Vieira Duarte et al., 2020, Cipriani et al., 2009). This fluid-assisted deformation combines brittle and ductile deformation mechanisms, with similar mineralogical assemblages and temperature conditions as presented here for Eastern SWIR samples (Fig. 11b; Kakihata et al., 2022; Kohli & Warren, 2020; Prigent et al., 2020).

A deep BDT is supported by recent microseismic studies that recorded hypocenters down to 15-20 km below seafloor at the Eastern SWIR (Chen et al., 2023; Grevemeyer et al.,

Journal Pre-proof

2019; Schlindwein and Schmid, 2016), at Gakkel ridge (Meier et al., 2021; Schlindwein et al., 2015) and along OTFs (de Melo et al., 2020; Grevemeyer et al., 2021).

The similarities between the nearly amagmatic SWIR axial detachments and OTFs are therefore striking. Both are large trans-lithospheric faults acting as plate boundaries along slow or ultraslow mid-oceanic ridges. However, detachment faults systematically accommodate exhumation, while OTFs only do it under conditions of incipient extension or compression: for example transtension near ridge/transform intersections (Prigent et al., 2020; Kohli et al., 2019), or transpression forming push-up ridges such as St Paul or Romanche OTFs (Bonatti et al., 1994; Maia et al., 2016). Both the degrees of finite deformation and the intensity of fluid-assisted deformation are more extreme in OTF ultramafic samples compared with samples from the Eastern SWIR. Most OTF samples are high temperature mylonites with generalized GSR and high proportions of hydrous minerals (Cannat et al., 1990; Cipriani et al., 2009; Jaroslow et al., 1996; Kakihata et al., 2022; Kohli & Warren, 2020; Prigent et al., 2020). By contrast, the deformation recorded in peridotites in the footwall of eastern SWIR detachments is strongly heterogeneous; GSR is local, at grain scale, and observed in only 31% of the dredged ultramafic samples (Table A2). The small proportion of synkinematic amphiboles in GSR zones also indicates a very limited role for fluid-assisted deformation.

These differences in deformation intensity and hydration reflect the contrasting lifetime of both structures: axial detachment faults at the Eastern SWIR have maximum offsets of 20 km and fault activity durations are < 3 Myr (Cannat et al., 2019). By contrast, OTFs are long-lived strike-slip faults with offsets reaching several hundreds of kilometers (Grevemeyer et al., 2021; Ligi et al., 2002). The maturity of OTFs allows long-lived strain accumulation in the mantle material, and a long-lasting exposure to seawater-derived fluids that percolate down to BDT level.

At the Eastern SWIR, strain accumulation is limited by the short lifetime of detachment faults (Cannat et al., 2019), and by the fact that mantle rocks are continuously exhumed out of the BDT into higher structural levels: the vertical exhumation along detachment faults implies a steady renewal of the lithospheric mantle involved in deformation and hydration. Fractures and microshear zones composing the detachment in the BDT zone allow fluid circulation (Fig. 11c-d);The fractured BDT material is then exhumed to shallower structural domains and new fractures and microfractures need to be formed in the newly, freshly exhuming BDT mantle. We propose that this constant regeneration of the mantle material along the detachment would limit pervasive fluid penetration and strain accumulation into the deep axial lithosphere.

6. Conclusions

At the Eastern SWIR, detachment faults exhume variably serpentinized ultramafic rocks on the seafloor. A third of these samples investigated as part of this work show evidence of fluid circulation beyond the serpentine stability field, by the occurrence of high-temperature Mg-hornblende to tremolitic deformed amphibole crystals. The composition of these amphiboles favors a hydrothermal origin. Seawater-derived fluids circulate along fractures and microfractures composing the axial detachment, down to the root zone of the fault, at the BDT zone. Fluid circulation is controlled by both brittle microfractures and small-scale rheological contrasts that focus fluids and along which amphibole forms preferentially. Amphibole composition is also controlled by the composition of the initial protolith. The extent and the distribution of mantle hydration along detachments from the Eastern SWIR is

Journal Pre-proof

similar to those observed along oceanic transform faults, despite much smaller intensity. We propose that the vertical exhumation of new material along the detachment fault coupled with the shorter lifetime of these detachments compared to OTFs, prevent a more pervasive deformation and hydration.

Data Avaibility

Microprobe data on which the results of this work are based are available on the Supplementary material of this study.

Acknowledgements

The authors thank Nick Dygert, an anonymous reviewer and the guest editor Frieder Klein for their helpful comments and suggestions. Partial funding of this work was supported by PRIN 2017 (PRIN2017KY5ZX8) and by ANR project «Ridge-Factory-Slow » (ANR- 18-CE01-0002). Thanks to the IPGP Marine Rock Repository for sample curation. The authors are grateful to M. Quintin for providing the thin sections, to M. Fialin and N. Rividi for their technical assistance at the CAMPARIS service in Paris. The IPGP SEM facility is supported by the IPGP multidisciplinary program PARI, and by Region île-de-France SESAME Grant no. 12015908.

Journal Pre-proof

Appendix A - Supplementary material

In this section we provide tables of data and additional figures that give further support for the results we presented in the paper. Table A1 displays the depths and positions of the dredges of *Smoothseafloor* cruise (https://doi.org/10.17600/10200050) and of the in-situ sample from *Rovsmooth* cruise (https://doi.org/10.17600/16002000). Table A2 classifies the different types of amphibole-bearing ultramafic samples and their relative estimated abundances. Table A3 provides the IGSN codes and the microstructural characteristics of the 28 samples analyzed in this study. Tables A4 to A6 respectively provide microprobe data measured on amphibole, clinopyroxene and spinel from the selected amphibole-bearing ultramafic samples.

Figure A1 shows prehnite grains in amphibole mylonites, as a hint for a magmatic protolith.

Declaration of interests

The authors declare that they have no known competing financial interests or personal relationships that could have appeared to influence the work reported in this paper.

References

Alard, O., Halimulati, A., Demouchy, S., 2022. Look between the grains. Nat. Geosci. 15, 856–857. https://doi.org/10.1038/s41561-022-01065-3

Albers, E., Schroeder, T., Bach, W., 2019. Melt Impregnation of Mantle Peridotite Facilitates High-Temperature Hydration and Mechanical Weakening: Implications for Oceanic Detachment Faults. Geochemistry, Geophys. Geosystems 20, 84–108. https://doi.org/10.1029/2018GC007783

Bach, W., Garrido, C.J., Paulick, H., Harvey, J., Rosner, M., 2004. Seawater-peridotite interactions: First insights from ODP Leg 209, MAR 15°N. Geochemistry, Geophys. Geosystems 5. https://doi.org/10.1029/2004GC000744

Bach, W., Jons, N., Klein, F., 2012. Metasomatism Within the Ocean Crust, in: Transformation of Rock. https://doi.org/10.1007/978-3-642-28394-9

Bickert, M., Cannat, M., Tommasi, A., Jammes, S., Lavier, L., 2021. Strain Localization in the Root of Detachment Faults at a Melt-Starved Mid-Ocean Ridge : A Microstructural Study of Abyssal Peridotites From the Southwest Indian Ridge. Geochemistry, Geophys.

Journal Pre-proof

Geosystems 22, 1–29. https://doi.org/10.1029/2020GC009434

Bonatti, E., Ligi, M., Gasperini, L., Peyve, A., Raznitsin, Y., Chen, Y.J., 1994. Transform migration and vertical tectonics at the Romanche Fracture Zone, equatorial Atlantic. J. Geophys. Res. 99. https://doi.org/10.1029/94jb01178

Boschi, C., Früh-Green, G.L., Delacour, A., Karson, J.A., Kelley, D.S., 2006. Mass transfer and fluid flow during detachment faulting and development of an oceanic core complex, Atlantis Massif (MAR 30°N). Geochemistry, Geophys. Geosystems 7. https://doi.org/10.1029/2005GC001074

Brunelli, D., Sanfilippo, A., Bonatti, E., Skolotnev, S., Escartin, J., Ligi, M., Ballabio, G., Cipriani, A., 2020. Origin of oceanic ferrodiorites by injection of nelsonitic melts in gabbros at the Vema Lithospheric Section, Mid Atlantic Ridge. Lithos 368–369, 105589. https://doi.org/10.1016/j.lithos.2020.105589

Cann, J.R., Blackman, D.K., Smith, D.K., McAllister, E., Janssen, B., Mello, S., Avgerinos, E., Pascoe, A.R., Escartin, J., 1997. Corrugated slip surfaces formed at ridge-transform intersections on the Mid-Atlantic Ridge. Nature 385, 329–332. https://doi.org/10.1038/385329a0

Cannat, M., 1993. Emplacement of Mantle Rocks in the Seafloor. J. Geophys. Res. 98, 4163–4172.

Cannat, M., Juteau, T., Berger, E., 1990. 5. PETROSTRUCTURAL ANALYSIS OF THE LEG 109 SERPENTINIZED PERIDOTITES. Proc. Ocean Drill. Program, Sci. Results, Vol. 106/109 106, 47–56.

Cannat, M., Sauter, D., Escartín, J., Lavier, L., Picazo, S., 2009. Oceanic corrugated surfaces and the strength of the axial lithosphere at slow spreading ridges. Earth Planet. Sci. Lett. https://doi.org/10.1016/j.epsl.2009.09.020

Journal Pre-proof

Cannat, M., Sauter, D., Lavier, L., Bickert, M., Momoh, E., Leroy, S., 2019. On spreading modes and magma supply at slow and ultraslow mid-ocean ridges. Earth Planet. Sci. Lett. 519, 223–233. https://doi.org/10.1016/j.epsl.2019.05.012

Cannat, M., Sauter, D., Mendel, V., Ruellan, E., Okino, K., Escartin, J., Combier, V., Baala, M., 2006. Modes of seafloor generation at a melt-poor ultraslow-spreading ridge. Geology 34, 605–608. https://doi.org/10.1130/G22486.1

Cannat, M., Sauter, D., Rouméjon, S., 2012. Formation of an ultramafic seafloor at the Southwest Indian Ridge 62°-65°E : internal structure of detachment faults and sparse volcanism documented by sidescan sonar and dredges. AGU Fall Meeting Abstracts.

Cannat, M., Seyler, M., 1995. Transform tectonics, metamorphic plagioclase and amphibolitization in ultramafic rocks of the Vema transform fault (Atlantic Ocean). Earth Planet. Sci. Lett. 133, 283–298. https://doi.org/10.1016/0012-821X(95)00078-Q

Ceuleneer, G., Cannat, M., 1997. 2. High-Temperature Ductile Deformation of Site 920 Peridotites. Proc. Ocean Drill. Program, Sci. Results 153, 23–34. https://doi.org/10.2973/odp.proc.sr.153.002.1997

Chen, J., Crawford, W., Cannat, M., 2023. Microseismicity and lithosphere thickness at a nearly amagmatic mid-ocean ridge. PREP.

Cipriani, A., Bonatti, E., Seyler, M., Brueckner, H.K., Brunelli, D., Dallai, L., Hemming, S.R., Ligi, M., Ottolini, L., Turrin, B.D., 2009. A 19 to 17 Ma amagmatic extension event at the Mid-Atlantic Ridge: Ultramafic mylonites from the Vema Lithospheric Section. Geochemistry, Geophys. Geosystems 10. https://doi.org/10.1029/2009GC002534

de Martin, B.J., Hirth, G., Evans, B., 2004. Experimental Constraints on Thermal Cracking of Peridotite at Oceanic Spreading Centers, in: Mid-Ocean Ridges: Hydrothermal Interactions Between the Lithosphere and Oceans.

Journal Pre-proof

de Melo, G.W.S., Parnell-Turner, R., Dziak, R.P., Smith, D.K., Maia, M., do Nascimento, A.F., Royer, J.-Y., 2020. Uppermost Mantle Velocity beneath the Mid-Atlantic Ridge and Transform Faults in the Equatorial Atlantic Ocean. Bull. Seismol. Soc. Am. https://doi.org/10.1785/0120200248

deMartin, B.J., Sohn, R.A., Pablo Canales, J., Humphris, S.E., 2007. Kinematics and geometry of active detachment faulting beneath the Trans-Atlantic Geotraverse (TAG) hydrothermal field on the Mid-Atlantic Ridge. Geology 35, 711. https://doi.org/10.1130/G23718A.1

Dick, H.J.B., Fisher, R.L., 1984. Mineralogic Studies of the Residues of Mantle Melting: Abyssal and Alpine-Type Peridotites, in: Kimberlites II: The Mantle and Crust-Mantle Relationships. pp. 295–308. https://doi.org/10.1016/B978-0-444-42274-3.50031-7

Dick, H.J.B., Ozawa, K., Meyer, P.S., Niu, Y., Robinson, P.T., Constantin, M., Hebert, R., Maeda, J., Natland, J., Hirth, G., Mackie, S.M., 2002. Primary silicate mineral chemistry of a 1.5-km section of very slow spreading lower ocean crust: ODP Hole 735B, Southwest Indian Ridge. Proc. Ocean Drill. Program, 176 Sci. Results. https://doi.org/10.2973/odp.proc.sr.176.001.2002

Dygert, N., Bernard, R.E., Behr, W.M., 2019. Great Basin Mantle Xenoliths Record Active Lithospheric Downwelling Beneath Central Nevada. Geochemistry, Geophys. Geosystems 20, 751–772. https://doi.org/10.1029/2018GC007834

Escartín, J., Andreani, M., Hirth, G., Evans, B., 2008. Relationships between the microstructural evolution and the rheology of talc at elevated pressures and temperatures. Earth Planet. Sci. Lett. 268, 463–475. https://doi.org/10.1016/j.epsl.2008.02.004

Escartin, J., Hirth, G., Evans, B., 1997. Effects of serpentinization on the litshopheric strength and the style of normal faulting at slow-spreading ridges. Earth Planet. Sci. Lett. 151, 181–189.

Escartín, J., Mével, C., MacLeod, C.J., McCaig, A.M., 2003. Constraints on deformation conditions and the origin of oceanic detachments: The Mid-Atlantic Ridge core complex at 15°45′N. Geochemistry, Geophys. Geosystems 4, 1–37. https://doi.org/10.1029/2002GC000472

Escartín, J., Mével, C., Petersen, S., Bonnemains, D., Cannat, M., Andreani, M., Augustin, N., Bezos, A., Chavagnac, V., Choi, Y., Godard, M., Haaga, K., Hamelin, C., Ildefonse, B., Jamieson, J., John, B., Leleu, T., MacLeod, C.J., Massot-Campos, M., Nomikou, P., Olive, J.A., Paquet, M., Rommevaux, C., Rothenbeck, M., Steinfuhrer, A., Tominaga, M., Triebe, L., Campos, R., Gracias, N., Garcia, R., 2017. Tectonic structure, evolution, and the nature of oceanic core complexes and their detachment fault zones (13°20′N and 13°30′N, Mid Atlantic Ridge). Geochemistry, Geophys. Geosystems 18, 1451–1482. https://doi.org/10.1002/2016GC006775

Fruh-green, G.L., Connolly, J.A.D., Plas, A., Kelley, D.S., Grobety, B., 2004. Serpentinization of Oceanic Peridotites : Implications for Geochemical Cycles and Biological Activity The Subseafloor Biosphere at Mid-Ocean Ridges. Geophys. Monogr. Ser. 144, 119–136.

Fumagalli, P., Zanchetta, S., Poli, S., 2009. Alkali in phlogopite and amphibole and their effects on phase relations in metasomatized peridotites: A high-pressure study. Contrib. to Mineral. Petrol. 158, 723–737. https://doi.org/10.1007/s00410-009-0407-4

Grevemeyer, I., Hayman, N.W., Lange, D., Peirce, C., Papenberg, C., Van Avendonk, H.J.A., Schmid, F., de La Peña, L.G., Dannowski, A., 2019. Constraining the maximum depth of brittle deformation at slow- and ultraslow-spreading ridges using microseismicity. Geology 47, 1069–1073. https://doi.org/10.1130/g46577.1

Grevemeyer, I., Rüpke, L.H., Morgan, J.P., Iyer, K., Devey, C.W., 2021. Extensional tectonics and two-stage crustal accretion at oceanic transform faults. Nature 591, 402–407. https://doi.org/10.1038/s41586-021-03278-9

Harigane, Y., Abe, N., Michibayashi, K., Kimura, J.-I., Chang, Q., 2016. Melt-rock interactions and fabric development of peridotites from North Pond in the Kane area, Mid-Atlantic Ridge: Implications of microstructural and petrological analyses of peridotite samples from IODP Hole U1382A. Geochemistry Geophys. Geosystems 17, 2298–2322. https://doi.org/10.1002/2016GC006429.

Ismail, W. Ben, Tommasi, A., Lopez-Sanchez, M.A., Rutter, E.H., Barou, F., Demouchy, S., 2021. Deformation of upper mantle rocks with contrasting initial fabrics in axial extension. Tectonophysics 815. https://doi.org/10.1016/j.tecto.2021.228997

Jaroslow, G.E., Hirth, G., Dick, H.J.B., 1996. Abyssal peridotite mylonites: implications for grain-size sensitive flow and strain localization in the oceanic lithosphere. Tectonophysics 256, 17–37. https://doi.org/10.1016/0040-1951(95)00163-8

Jöns, N., Bach, W., Klein, F., 2010. Magmatic influence on reaction paths and element transport during serpentinization. Chem. Geol. 274, 196–211. https://doi.org/10.1016/j.chemgeo.2010.04.009

Kakihata, Y., Michibayashi, K., Dick, H.J.B., 2022. Heterogeneity in texture and crystal fabric of intensely hydrated ultramylonitic peridotites along a transform fault, Southwest Indian Ridge. Tectonophysics 823, 229206. https://doi.org/10.1016/j.tecto.2021.229206

Karato, S.-I., Paterson, M.S., Fitzgerald, J.D., 1986. Rheology of Synthetic Olivine Aggregates: Influence of Grain Size and Water. J. Geophys. Res. 91, 8151–8176. https://doi.org/10.1029/JB091iB08p08151

Journal Pre-proof

Journal Pre-proof

Klein, F., Bach, W., Jöns, N., McCollom, T., Moskowitz, B., Berquó, T., 2009. Iron partitioning and hydrogen generation during serpentinization of abyssal peridotites from 15°N on the Mid-Atlantic Ridge. Geochim. Cosmochim. Acta 73, 6868–6893. https://doi.org/10.1016/j.gca.2009.08.021

Klein, F., Grozeva, N.G., Seewald, J.S., McCollom, T.M., Humphris, S.E., Moskowitz, B., Berquó, T.S., Kahl, W.A., 2015. Fluids in the Crust. Experimental constraints on fluid-rock reactions during incipient serpentinization of harzburgite. Am. Mineral. 100, 991–1002. https://doi.org/10.2138/am-2015-5112

Kohli, A., Wolfson-Schwehr, M., Prigent, C., Warren, J.M., 2021. Oceanic transform fault seismicity and slip mode influenced by seawater infiltration. Nat. Geosci. 14, 606–611. https://doi.org/10.1038/s41561-021-00778-1

Kohli, A.H., Warren, J.M., 2020. Evidence for a Deep Hydrologic Cycle on Oceanic Transform Faults. J. Geophys. Res. Solid Earth 125, 1–23. https://doi.org/10.1029/2019JB017751

Le Roux, V., Urann, B.M., Brunelli, D., Bonatti, E., Cipriani, A., Demouchy, S., Monteleone, B.D., 2021. Postmelting hydrogen enrichment in the oceanic lithosphere. Sci. Adv. 7, 1–11. https://doi.org/10.1126/sciadv.abf6071

Ligi, M., Bonatti, E., Gasperini, L., Poliakov, A.N.B., 2002. Oceanic broad multifault transform plate boundaries. Geology 30, 11–14. https://doi.org/10.1130/0091-7613(2002)030<0011:OBMTPB>2.0.CO;2

Lopez-Sanchez, M.A., Tommasi, A., Ismail, W. Ben, Barou, F., 2021. Dynamic recrystallization by subgrain rotation in olivine revealed by electron backscatter diffraction. Tectonophysics 815, 228916. https://doi.org/10.1016/j.tecto.2021.228916

MacLeod, C.J., Escartin, J., Banerji, D., Banks, G.J., Gleeson, M., Irving, D.H.B., Lilly, R.M., McCaig, A.M., Niu, Y., Allerton, S., Smith, D.K., 2002. Direct geological evidence for oceanic detachment faulting: The Mid-Atlantic Ridge, 15 45N. Geology 30, 879–882. https://doi.org/10.1130/0091-7613(2002)030<0879:DGEFOD>2.0.CO;2

Maia, M., Sichel, S., Briais, A., Brunelli, D., Ligi, M., Ferreira, N., Campos, T., Mougel, B., Brehme, I., Hémond, C., Motoki, A., Moura, D., Scalabrin, C., Pessanha, I., Alves, E., Ayres, A., Oliveira, P., 2016. Extreme mantle uplift and exhumation along a transpressive transform fault. Nat. Geosci. 9, 619–623. https://doi.org/10.1038/ngeo2759

Meier, M., Schlindwein, V., Scholz, J., Geils, J., Schmidt-Aursch, M.C., Krüger, F., Czuba, W., Janik, T., 2021. Segment-Scale Seismicity of the Ultraslow Spreading Knipovich Ridge. Geochemistry, Geophys. Geosystems 22. https://doi.org/10.1029/2020GC009375

Ozawa, K., Meyer, P.S., Bloomer, S.H., 1991. Mineralogy and Textures of Iron-Titanium Oxide Gabbros and Associated Olivine Gabbros from Hole 735B, in: Proceedings of the Ocean Drilling Program, 118 Scientific Results. Ocean Drilling Program. https://doi.org/10.2973/odp.proc.sr.118.125.1991

Paquet, M., Cannat, M., Brunelli, D., Hamelin, C., Humler, E., 2016. Effect of melt/mantle interactions on MORB chemistry at the easternmost Southwest Indian Ridge (61-67°E). Geochemistry Geophys. Geosystems 17, 1312–1338. https://doi.org/10.1002/2015GC006205.Received

Parnell-Turner, R., Sohn, R.A., Peirce, C., Reston, T.J., Macleod, C.J., Searle, R.C., Simão, N., 2020. Seismicity trends and detachment fault structure at 13°N, Mid-Atlantic Ridge. Geology. https://doi.org/10.1130/G48420.1

Parnell-Turner, R., Sohn, R.A., Peirce, C., Reston, T.J., MacLeod, C.J., Searle, R.C., Simão, N.M., 2017. Oceanic detachment faults generate compression in extension. Geology 45, 923–926. https://doi.org/10.1130/G39232.1

Journal Pre-proof

Patterson, S.N., Lynn, K.J., Prigent, C., Warren, J.M., 2021. High temperature hydrothermal alteration and amphibole formation in Gakkel Ridge abyssal peridotites. Lithos 392–393, 106107. https://doi.org/10.1016/j.lithos.2021.106107

Picazo, S., Cannat, M., Delacour, A., Escartín, J., Rouméjon, S., Silantyev, S., 2012. Deformation associated with the denudation of mantle-derived rocks at the Mid-Atlantic Ridge 13°-15°N: The role of magmatic injections and hydrothermal alteration. Geochemistry, Geophys. Geosystems 13. https://doi.org/10.1029/2012GC004121

Prigent, C., Warren, J.M., Kohli, A.H., Teyssier, C., 2020. Fracture-mediated deep seawater flow and mantle hydration on oceanic transform faults. Earth Planet. Sci. Lett. 532, 115988. https://doi.org/10.1016/j.epsl.2019.115988

Reston, T., 2018. Flipping detachments: The kinematics of ultraslow spreading ridges. Earth Planet. Sci. Lett. 503, 144–157. https://doi.org/10.1016/j.epsl.2018.09.032

Reston, T.J., McDermott, K.G., 2011. Successive detachment faults and mantle unroofing at magma-poor rifted margins. Geology 39, 1071–1074. https://doi.org/10.1130/G32428.1

Rouméjon, S., Cannat, M., 2014. Serpentinization of mantle-derived peridotites at mid-ocean ridges: Mesh texture development in the context of tectonic exhumation. Geochemistry, Geophys. Geosystems 15, 2354–2379. https://doi.org/10.1002/2013GC005148

Rouméjon, S., Cannat, M., Agrinier, P., Godard, M., Andreani, M., 2015. Serpentinization and fluid pathways in tectonically exhumed peridotites from the southwest Indian ridge (62-65°E). J. Petrol. 56, 703–734. https://doi.org/10.1093/petrology/egv014

Sauter, D., Cannat, M., Rouméjon, S., Andreani, M., Birot, D., Bronner, A., Brunelli, D., Carlut, J., Delacour, A., Guyader, V., MacLeod, C.J., Manatschal, G., Mendel, V., Ménez, B.,

Journal Pre-proof

Pasini, V., Ruellan, E., Searle, R., 2013. Continuous exhumation of mantle-derived rocks at the Southwest Indian Ridge for 11 million years. Nat. Geosci. 6, 314–320. https://doi.org/10.1038/ngeo1771

Schlindwein, V., Demuth, A., Korger, E., Läderach, C., Schmid, F., 2015. Seismicity of the Arctic mid-ocean Ridge system. Polar Sci. 9, 146–157. https://doi.org/10.1016/j.polar.2014.10.001

Schlindwein, V., Schmid, F., 2016. Mid-ocean-ridge seismicity reveals extreme types of ocean lithosphere. Nature 535, 276–279. https://doi.org/10.1038/nature18277

Schmädicke, E., Gose, J., Stalder, R., 2018. Water in Abyssal Peridotite: Why Are Melt-Depleted Rocks so Water Rich? Geochemistry, Geophys. Geosystems 19, 1824–1843. https://doi.org/10.1029/2017GC007390

Schroeder, T., John, B.E., 2004. Strain localization on an oceanic detachment fault system, Atlantis Massif, 30°N, Mid-Atlantic Ridge. Geochemistry, Geophys. Geosystems 5. https://doi.org/10.1029/2004GC000728

Seyler, M., Cannat, M., Mével, C., 2003. Evidence for major-element heterogeneity in the mantle source of abyssal peridotites from the Southwest Indian Ridge (52° to 68°E). Geochemistry, Geophys. Geosystems 4. https://doi.org/10.1029/2002GC000305

Seyler, M., Lorand, J.P., Dick, H.J.B., Drouin, M., 2007. Pervasive melt percolation reactions in ultra-depleted refractory harzburgites at the Mid-Atlantic Ridge, 15° 20'N: ODP Hole 1274A. Contrib. to Mineral. Petrol. 153, 303–319. https://doi.org/10.1007/s00410-006-0148-6

Smith, D.K., Cann, J.R., Escartín, J., 2006. Widespread active detachment faulting and core complex formation near 13°N on the Mid-Atlantic Ridge. Nature 442, 440–443. https://doi.org/10.1038/nature04950

Spear, F.S., 1981. An experimental study of hornblende stability and compositional variability in amphibolite. Am. J. Sci. 281, 697–734.

Tani, K., Dunkley, D.J., Ohara, Y., 2011. Termination of backarc spreading: Zircon dating of a giant oceanic core complex. Geology 39, 47–50. https://doi.org/10.1130/G31322.1

Tucholke, B.E., Behn, M.D., Buck, W.R., Lin, J., 2008. Role of melt supply in oceanic detachment faulting and formation of megamullions. Geology 36, 455–458. https://doi.org/10.1130/G24639A.1

Urann, B.M., Le Roux, V., Hammond, K., Marschall, H.R., Lee, C.T.A., Monteleone, B.D., 2017. Fluorine and chlorine in mantle minerals and the halogen budget of the Earth's mantle. Contrib. to Mineral. Petrol. 172. https://doi.org/10.1007/s00410-017-1368-7

Vieira Duarte, J.F., Kaczmarek, M.A., Vonlanthen, P., Putlitz, B., Müntener, O., 2020. Hydration of a Mantle Shear Zone Beyond Serpentine Stability: A Possible Link to Microseismicity Along Ultraslow Spreading Ridges? J. Geophys. Res. Solid Earth 125, 1–24. https://doi.org/10.1029/2020JB019509

Whitney, D.L., Evans, B.W., 2010. Abbreviations for names of rock-forming minerals. Am. Mineral. 95, 185–187. https://doi.org/10.2138/am.2010.3371

Yu, Z., Li, J., Niu, X., Rawlinson, N., Ruan, A., Wang, W., Hu, H., Wei, X., Zhang, J., Liang, Y., 2018. Lithospheric Structure and Tectonic Processes Constrained by Microearthquake Activity at the Central Ultraslow-Spreading Southwest Indian Ridge (49.2° to 50.8°E). J. Geophys. Res. Solid Earth 123, 6247–6262. https://doi.org/10.1029/2017JB015367

Journal Pre-proof

TABLES

Table 1: Representative spot analyses of amphibole compositions for the four types of amphibole-bearing samples from the Eastern SWIR: neoblasts in Fig. 3b, 7d-e (marked points) in GSR zones; neoblasts in Fig. 4b and in shear zones in Fig. 7f (marked points) in melt-impregnated ultramafic samples; porphyroclasts and neoblasts in Fig. 5b-c for amphibole mylonites; and fibrous amphiboles in Fig. 5e and undeformed amphiboles in Fig. 5f for serpentinized ultramafic samples. The whole amphibole data set is in Table A4.

thin section	amphibole-bearing type	mineral	position	SiO2	TiO2	Al2O3	FeO	MnO	MgO	CaO	Na2O	K2O	Cr2O3	NiO	Cl	F	TOTAL	Mg#	AlT	(Na+K)A	Si
SMS_DR10_4_8A	amphibole-bearing GSR zone	amphibole13	neoblast	53.38	0.20	4.03	2.26	0.11	21.76	13.99	0.78	0.00	0.58	0.06	0.05	0.00	97.20	94.48	0.57	0.21	7.43
SMS_DR10_4_8A	amphibole-bearing GSR zone	amphibole14	neoblast	51.88	0.26	5.76	2.57	0.02	22.47	11.40	1.21	0.01	0.74	0.12	0.07	0.00	96.53	93.97	0.75	0.33	7.25
SMS_DR10_4_8A	amphibole-bearing GSR zone	amphibole16	neoblast	52.48	0.18	3.90	2.69	0.05	23.73	11.41	0.81	0.01	0.50	0.07	0.06	0.09	95.89	94.03	0.62	0.22	7.38
SMS_DR10_4_8	amphibole-bearing GSR zone	amphibole	vein	51.43	0.21	7.94	3.85	0.02	20.38	12.51	1.67	0.03	0.60	0.08	0.00	0.09	98.69	90.43	0.90	0.43	7.10

A		V2																			
SM		a																			
S_		m																			
DR		ph		4					1	1							9	9			
10		ib		9	0	9	3	0	9	2	2	0	0	0	0	0	8	0	1	0	6
_4	amphibol	ol		.	.	.	.	.	.	.	.	.	.	.	.	.	.	.	.	.	.
_8	e-bearing	e	vei	7	1	6	5	0	5	4	1	0	7	0	0	0	0	8	0	5	9
A	GSR zone	V3	n	6	4	5	1	6	6	5	3	1	2	0	0	0	0	4	7	1	3
SM		a																			
S_		m																			
DR		ph		5					2	1							9	9			
10		ib		2	0	5	3	0	3	1	1	0	0	0	0	0	8	2	0	0	7
_4	amphibol	ol		.	.	.	.	.	.	.	.	.	.	.	.	.	.	.	.	.	.
_8	e-bearing	e	vei	1	1	9	5	0	5	3	2	0	3	0	0	0	4	2	8	3	1
A	GSR zone	V3	n	8	6	6	5	4	6	7	5	1	7	0	0	0	5	1	2	4	8
SM		a																			
S_		m																			
DR		ph		5					2	1							9	9			
10		ib		3	0	5	2	0	1	2	1	0	0	0	0	0	7	4	0	0	7
_4	amphibol	ol		.	.	.	.	.	.	.	.	.	.	.	.	.	.	.	.	.	.
_8	e-bearing	e	vei	2	1	9	3	0	6	6	2	0	4	0	0	0	5	2	6	3	3
A	GSR zone	V4	n	0	1	0	3	4	0	0	7	2	8	0	0	0	4	9	5	0	5
SM																					
S_		a																			
DR		m		5					2	1							9	9			
17		ph		3	0	6	2	0	2	2	1	0	0	0	0	0	8	3	0	0	7
_4	amphibol	ib	ne	.	.	.	.	.	.	.	.	.	.	.	.	.	.	.	.	.	.
_0	e-bearing	ol	obl	2	1	2	9	0	0	3	2	0	4	1	0	0	7	0	7	3	2
6	GSR zone	e4	ast	3	1	3	3	0	9	6	3	2	5	1	3	0	9	7	2	3	8
SM																					
S_		a																			
DR		m		5					2	1							9	9			
17		ph		3	0	5	2	0	2	2	1	0	0	0	0	0	8	3	0	0	7
_4	amphibol	ib	ne	.	.	.	.	.	.	.	.	.	.	.	.	.	.	.	.	.	.
_0	e-bearing	ol	obl	4	0	6	8	0	3	5	1	0	3	1	0	0	4	4	6	3	3
6	GSR zone	e5	ast	6	6	2	0	0	8	2	1	1	4	4	3	0	8	4	7	0	3
SM																					
S_		a																			
DR		m		5					2	1							9	9			
17		ph		2	0	7	3	0	1	2	1	0	0	0	0	0	8	2	0	0	7
_4	amphibol	ib	ne	.	.	.	.	.	.	.	.	.	.	.	.	.	.	.	.	.	.
_0	e-bearing	ol	obl	1	0	1	0	0	5	5	4	0	2	0	0	0	3	5	8	3	1
6	GSR zone	e7	ast	1	3	5	8	5	6	9	4	2	8	4	3	0	7	9	2	9	8
SM	amphibol	a	ne	4	0	1	3	0	1	1	3	0	1	0	0	0	9	9	1	0	6
S_	e-bearing	m	obl	6	.	1	.	.	8	1	.	.	.	.	.	.	7	0	.	.	.
DR	melt-	ph	ast	.	2	.	7	0	.	.	0	0	4	0	1	0	.	.	5	7	5

29_4_6	impregnated ultramafic	ibole 3		00	6	70	6	6	99	99	1	8	8	2	3	3	52	00	0	6	0
SMS_DR29_4_6	amphibole-bearing melt-impregnated ultramafic	amphibole 4	neoblast	46.50	0.22	11.71	3.64	0.03	19.24	12.08	2.94	0.03	1.63	0.16	0.13	0.00	98.33	90.41	1.48	0.75	6.52
SMS_DR29_5_31	amphibole-bearing melt-impregnated ultramafic	amphibole 9	post	57.28	0.12	2.18	1.97	0.06	22.96	13.16	0.79	0.02	0.19	0.09	0.04	0.00	98.87	95.40	0.24	0.14	7.76
SMS_DR29_5_31	amphibole-bearing melt-impregnated ultramafic	amphibole 9	post	58.62	0.06	0.65	1.89	0.06	23.46	12.73	0.91	0.02	0.00	0.10	0.00	0.00	98.49	95.68	0.06	0.12	7.94
SMS_DR29_5_31	amphibole-bearing melt-impregnated ultramafic	amphibole 10	porphyroclast	52.13	0.30	6.27	2.39	0.00	20.97	12.94	2.16	0.07	0.99	0.16	0.02	0.01	98.41	93.99	0.79	0.51	7.21
SMS_DR29_5_31	amphibole-bearing melt-impregnated ultramafic	amphibole 11	porphyroclast	51.30	0.39	6.87	2.81	0.07	20.63	12.72	2.36	0.01	0.99	0.03	0.04	0.00	98.23	92.90	0.88	0.53	7.12
SMS_DR27_3_20	amphibole mylonite	amphibole 7	porphyroclast	50.06	2.07	7.63	3.83	0.05	20.38	11.92	2.34	0.02	0.32	0.17	0.07	0.08	98.94	90.46	1.08	0.47	6.92

SMS_DR27_3_20	amphibole mylonite	amphibole8	neoblast	49.82	1.21	7.74	3.28	0.05	20.48	12.17	2.20	0.02	1.38	0.13	0.08	0.07	98.61	91.76	1.09	0.48	6.91
SMS_DR27_3_20	amphibole mylonite	amphibole9	neoblast	49.10	2.01	8.37	3.58	0.07	19.91	12.27	2.34	0.03	1.13	0.13	0.09	0.00	99.03	90.85	1.19	0.52	6.81
SMS_DR33_2_7	amphibole mylonite	amphibole1	porphyroclast	46.77	3.06	7.78	11.56	0.26	16.16	9.63	2.83	0.27	0.05	0.10	0.02	0.16	98.65	71.36	1.28	0.59	6.72
SMS_DR33_2_7	amphibole mylonite	amphibole1	porphyroclast	46.59	3.12	7.83	11.32	0.22	15.96	9.87	2.83	0.28	0.00	0.05	0.01	0.00	98.06	71.53	1.25	0.66	6.75
SMS_DR33_2_7	amphibole mylonite	amphibole2	neoblast	49.45	1.04	8.31	3.89	0.04	20.21	11.67	2.58	0.12	0.32	0.15	0.05	0.05	97.88	90.26	1.09	0.58	6.91
SMS_DR29_4_7	amphibole-bearing serpentinized peridotite	amphibole3	post	52.71	0.12	5.18	2.47	0.05	22.15	12.12	1.80	0.05	0.95	0.13	0.05	0.00	97.78	94.12	0.70	0.44	7.30
SMS_DR29_4	amphibole-bearing serpentinized peridotit	amphibol	post	55.45	0.11	3.26	2.17	0.00	22.71	12.94	1.14	0.03	0.56	0.09	0.02	0.06	98.55	94.91	0.43	0.24	7.57

Journal Pre-proof

_7	e	e3																			
SMS_DR29_4_7	amphibole-bearing serpentinized peridotite	amphibole4	porphyroclast	56.24	0.01	2.76	2.15	0.04	23.07	13.27	0.96	0.03	0.06	0.13	0.01	0.05	98.78	95.02	0.35	0.23	7.65
SMS_DR29_4_7	amphibole-bearing serpentinized peridotite	amphibole5	deformed acicular	55.82	0.13	3.09	2.60	0.05	23.14	12.64	1.13	0.03	0.06	0.00	0.01	0.08	98.76	94.08	0.41	0.24	7.59
SMS_DR29_4_7	amphibole-bearing serpentinized peridotite	amphibole7	deformed acicular	56.88	0.09	2.11	2.25	0.07	23.40	12.60	0.83	0.02	0.05	0.05	0.10	0.14	98.44	94.87	0.28	0.14	7.72
SMS_DR29_4_7	amphibole-bearing serpentinized peridotite	amphibole8	deformed acicular	57.44	0.13	1.99	2.02	0.02	23.10	13.01	0.65	0.02	0.02	0.12	0.00	0.09	98.60	95.32	0.22	0.08	7.78

FIGURES

FIGURE 1

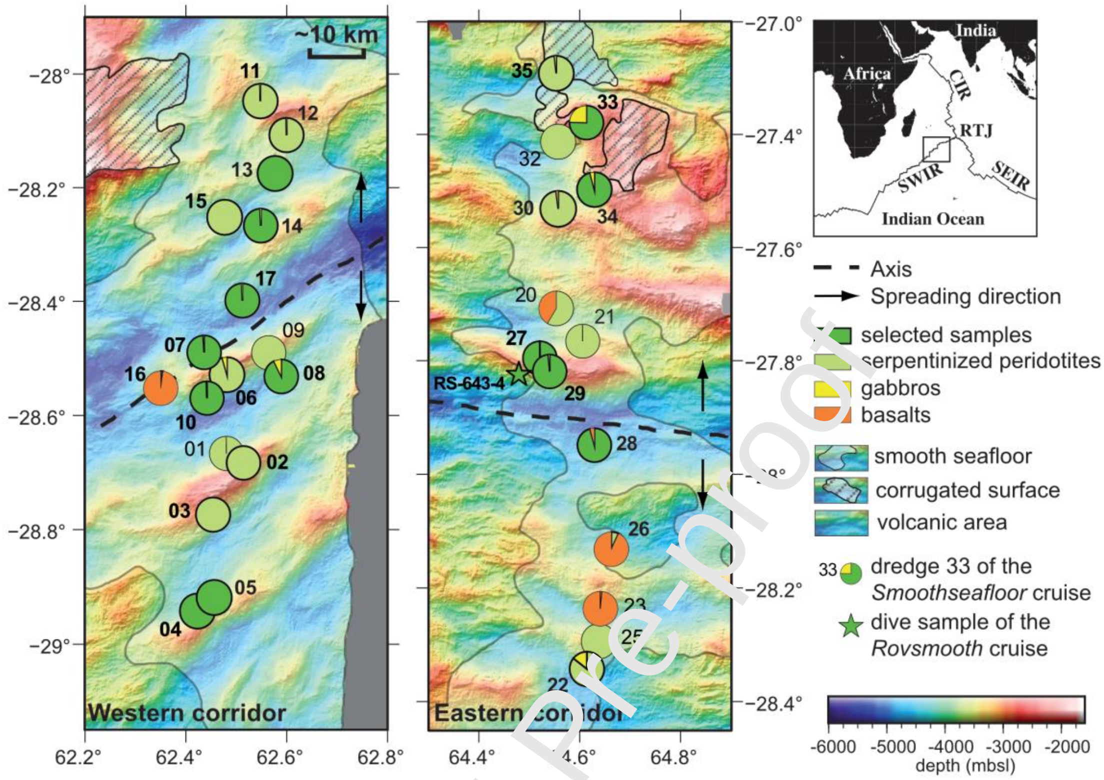

FIGURE 1: (a) Bathymetric map of the two nearly-amagmatic spreading corridors of the eastern Southwest Indian Ridge (62-65°E). Smooth and corrugated surfaces are highlighted in white and dashed areas respectively. Samples were dredged on- and off-axis (black dashed line) during the *Smoothseafloor* cruise (doi: 10.17600/10200050, Table A1). Map is modified from Rouméjon et al., 2015 (after Sauter et al., 2013). Pie charts show proportions of dredged samples recovered by rock type. Dredges that recovered amphibole-bearing peridotites are shown in thicker contours, and those in which amphibole-bearing samples were analyzed for this study are shown in dark green. The green star indicates the position of sample RS-643-4, which was sampled *in-situ* during a ROV dive on the wall of the active detachment (*Rovsmooth* cruise, doi: 10.17600/16002000; Table A1).

Journal Pre-proof

Journal Pre-proof

FIGURE 2

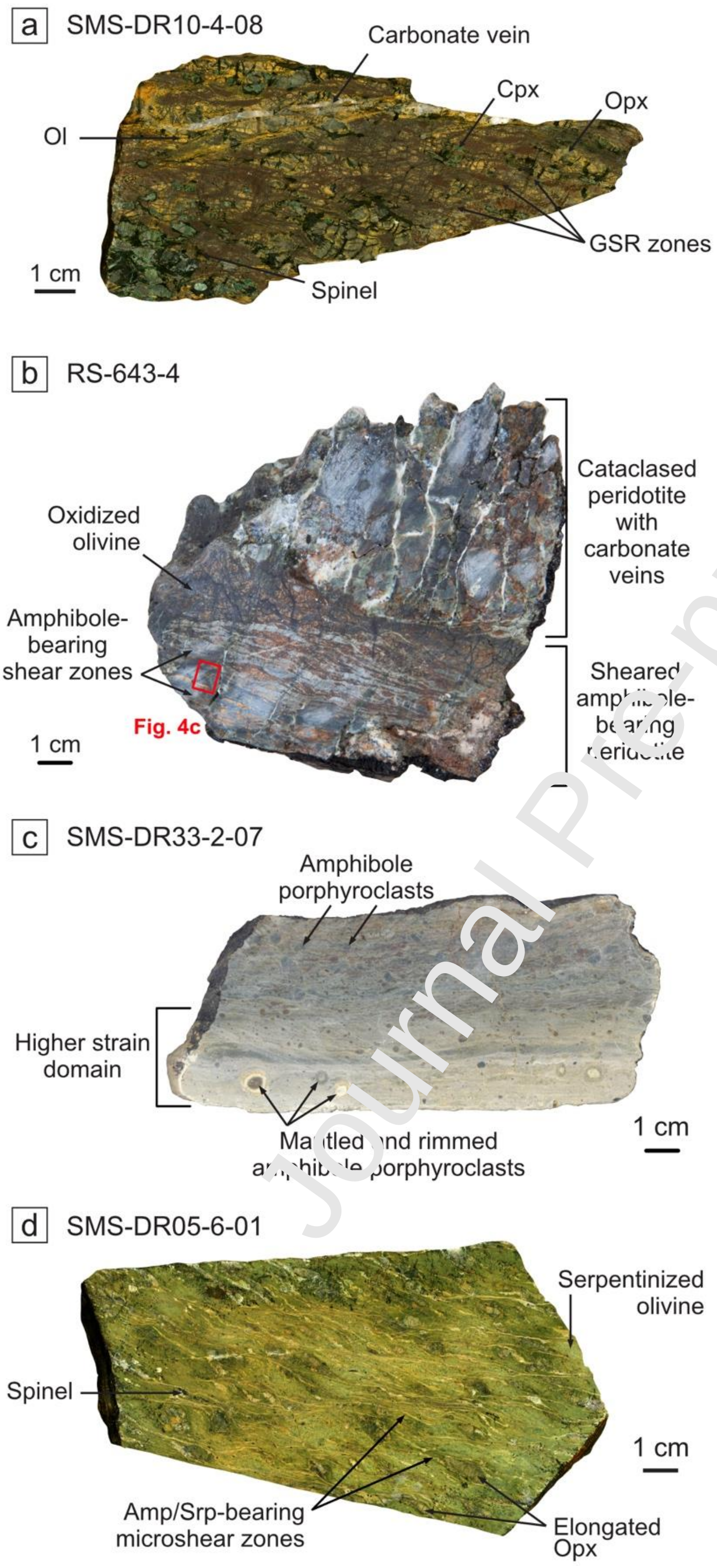

Journal Pre-proof

Figure 2: Photographs of selected amphibole-bearing ultramafic rocks from the Eastern SWIR. (a) Deformed partially serpentinized lherzolite (sample SMS-DR10-4-08). Texture is

strongly foliated with elongated porphyroclasts of orthopyroxene (Opx) and clinopyroxene (Cpx), and anastomosed grain size reduction (GSR) zones that locally contain amphibole (see Fig. 3; Bickert et al., 2021). Olivine (Ol) is partially replaced by oxidized minerals. Primary mineralogy is cut by late veins of carbonates. (b) Cataclased melt-impregnated peridotite, partially replaced by oxidized minerals, with amphibole-bearing shear bands clustered along orthopyroxene grains (sample RS-643-4). The red square outlines the location of Figure 4c. (c) Amphibole mylonite (sample SMS-DR33-2-07). Brown amphibole porphyroclasts in the most deformed part of the sample form rolling structures (δ-/σ-types) enclosed in a very fine-grained matrix of amphibole, chlorite and talc. (d) Foliated amphibole-bearing serpentinized peridotite (sample SMS-DR05-6-01). Shear zones of amphibole (Amp) and serpentine (Srp) underline the foliation. Olivine is fully replaced by serpentine (Srp).

Journal Pre-proof

FIGURE 3

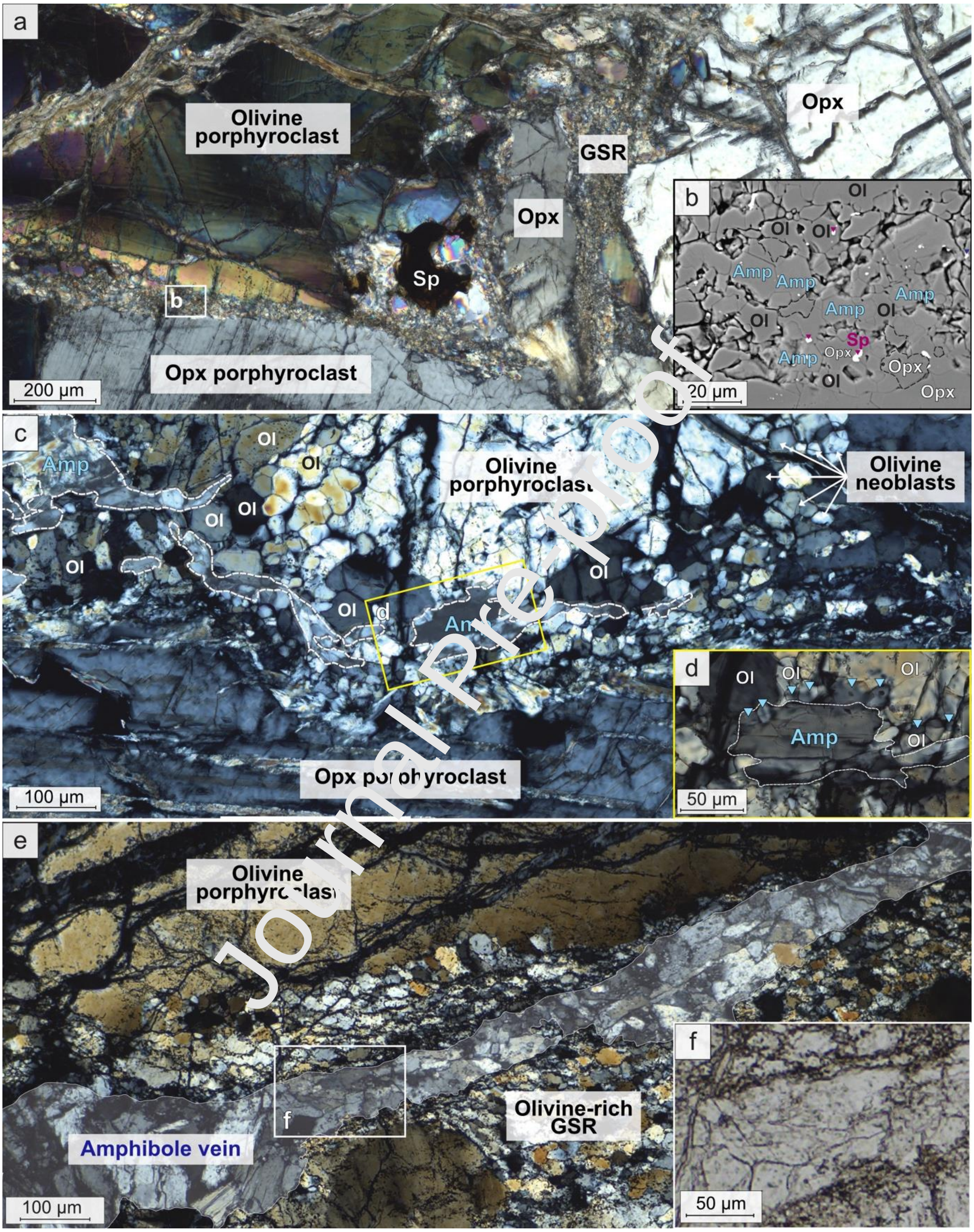

Figure 3: Amphiboles in Grain Size Reduction (GSR) zones. Microphotographs under cross-polarized light (a, c-e) and SEM images (b). (a) Microphotography of a GSR zone at contact between olivine and orthopyroxene porphyroclasts (sample SMS-DR17-4-6). (b) SEM detail

Journal Pre-proof

of the recrystallized assemblage composed of olivine (Ol) + spinel (Sp) + orthopyroxene (Opx) + polygonal amphiboles (Amp) (modified from Bickert et al., 2021). (c) Coarser prismatic amphiboles in an olivine-rich GSR zone (sample SMS- DR08-2-26). (d) Detail of the same GSR zone showing small polygonal amphibole and olivine crystals crystallizing together at contact with a coarser prismatic amphibole. (e, f) Undeformed vein of tabular and prismatic amphiboles crosscutting an olivine-rich GSR domain (sample SMS-DR10-4-08).

Journal Pre-proof

FIGURE 4

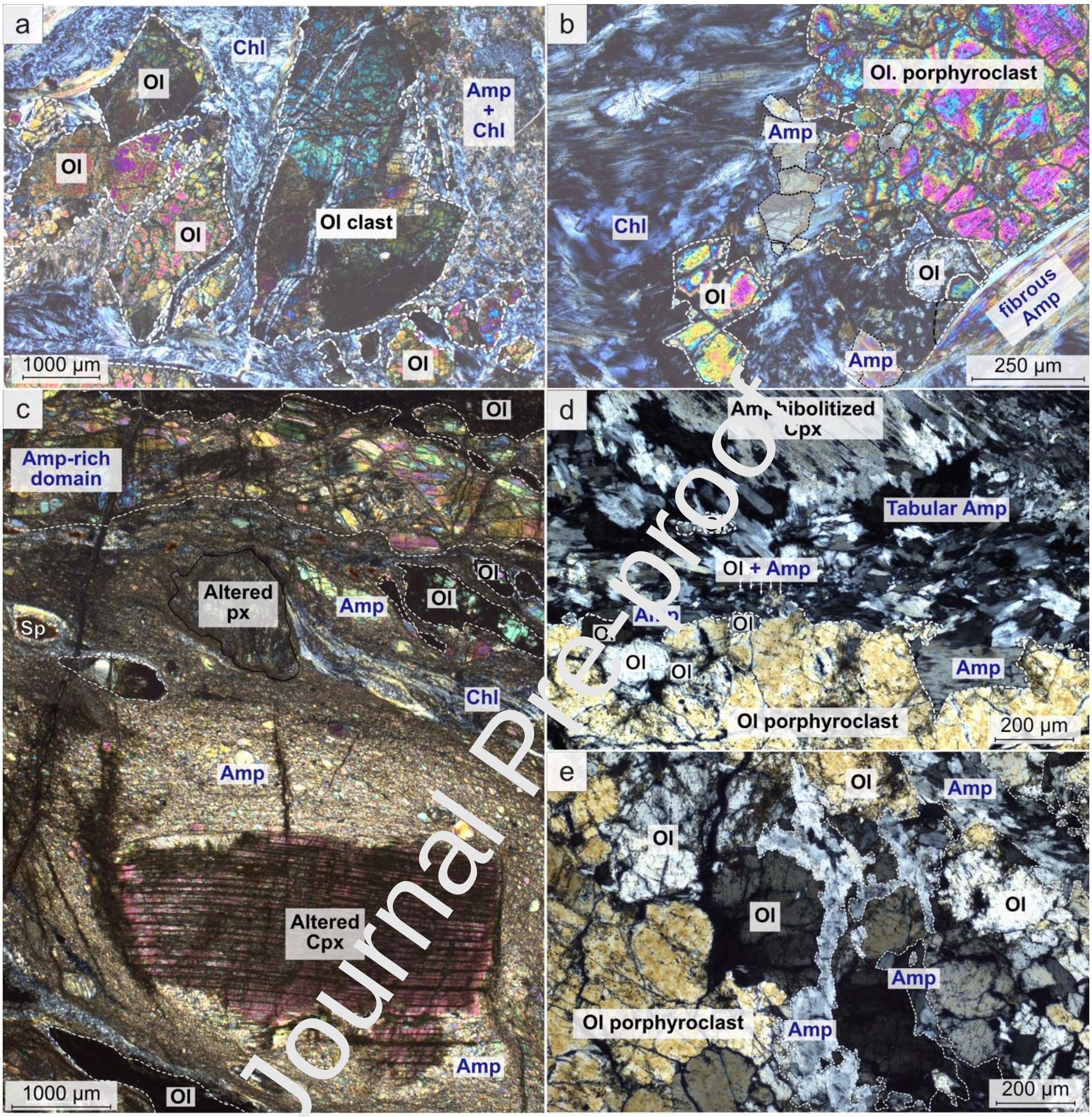

FIGURE 4: Amphibole-bearing melt-impregnated peridotites. Microphotographs under cross-polarized light. (a) Microshear zones enclosing clasts of olivine (Ol) fragments in a matrix of fibrous to primastic amphibole (Amp) and chlorite (Chl) (sample SMS-DR29-4-06). (b) Detail of the contact between olivine (Ol) and the matrix. Locally, olivine recrystallizes in coarse grains with prismatic amphibole (Amp). Fibrous amphibole crosscut olivine neoblasts, postdating the deformation (lower right side of the picture). (c) Example of a sample (sample RS-643-04) with thicker amphibole-rich domains composed of elongated and deformed

Journal Pre-proof

Journal Pre-proof

amphibole porphyroclasts. Amphibole-bearing shear zones are mostly focused along pyroxene porphyroclasts. (Clino-)pyroxene (Cpx) porphyroclasts are partially to fully replaced by syn-deformation amphibole. Relicts of olivine (Ol) and spinel (Sp) have elongated shapes and are enclosed in a matrix of prismatic to fibrous amphibole (Amp) and chlorite (Chl). The elongated size of pyroxenes and spinel porphyroclasts suggest a HT primary shear zone that has been subsequently altered. (d) Late amphibole shear zones at contact with olivine and clinopyroxene porphyroclasts (sample SMS-DR29-7-01). Clinopyroxene (Cpx) is fully replaced by tabular amphiboles (Amp) similar to the ones surrounding it. Olivine (Ol) remains fresh with slightly corroded / blurred boundaries at contact with amphibole shear zones, due to local recrystallization of olivine and amphibole. (e) Interstitial, prismatic undeformed amphiboles along olivine grain boundaries in the same sample (SMS-DR29-7-01).

Journal Pre-proof

FIGURE 5

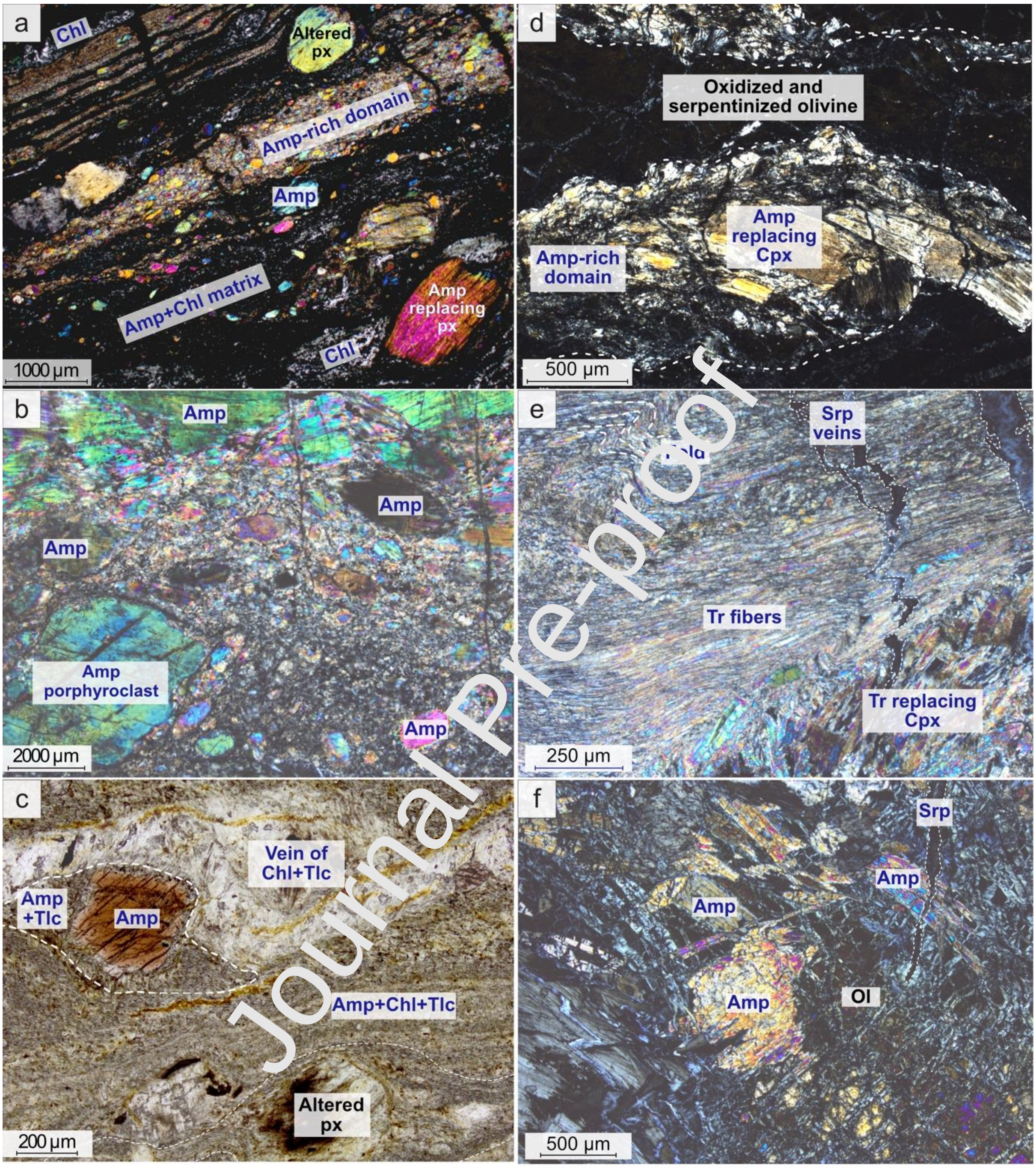

Journal Pre-proof

FIGURE 5: Amphibole mylonites (a-c) and amphibole-bearing serpentinized peridotites (d-f). Microphotographs under cross-polarized (a-b, d-f) and natural light (c). (a) Alternation of amphibole-rich domains with polymineralic domains. Pyroxenes (px) are entirely replaced by amphibole (amp; sample SMS-DR13-4-41). (b) Amphibole-rich domains are composed of deformed porphyroclasts of amphibole in a matrix of amphibole neoblasts (sample SMS-

DR27-3-20). (c) Polymineralic domains are composed of porphyroclasts of brown amphiboles and altered pyroxenes forming complex rolling structures (δ- to σ-types) in a matrix of amphibole (Amp) ± chlorite (Chl) ± talc (Tlc). Locally, veins of chlorite (Chl) and talc (Tlc) follow the foliation (sample SMS-DR33-2-07). (d) In amphibole-bearing serpentinized peridotites, primary minerals such as olivine (Ol) and pyroxenes (px) are almost completely altered or replaced by amphibole (Amp; sample SMS-DR13-4-41). Amphibole and the replaced pyroxene porphyroclasts can locally be fragmented in a domino type /shear band type. (e) Detail of a late shear zone of fibrous tremolite (Tr), in contact with weakly deformed peridotite in which clinopyroxene (Cpx) is replaced by tabular to prismatic amphiboles (Amp; sample SMS-DR29-4-07). Serpentine (Srp) veins cut the amphibole shear zones, postdating amphibole deformation. (f) Detail of undeformed tabular to prismatic amphibole in olivine groundmass cut by serpentine (Srp) fractures (sample SMS-DR29-4-07).

Journal Pre-proof

FIGURE 6

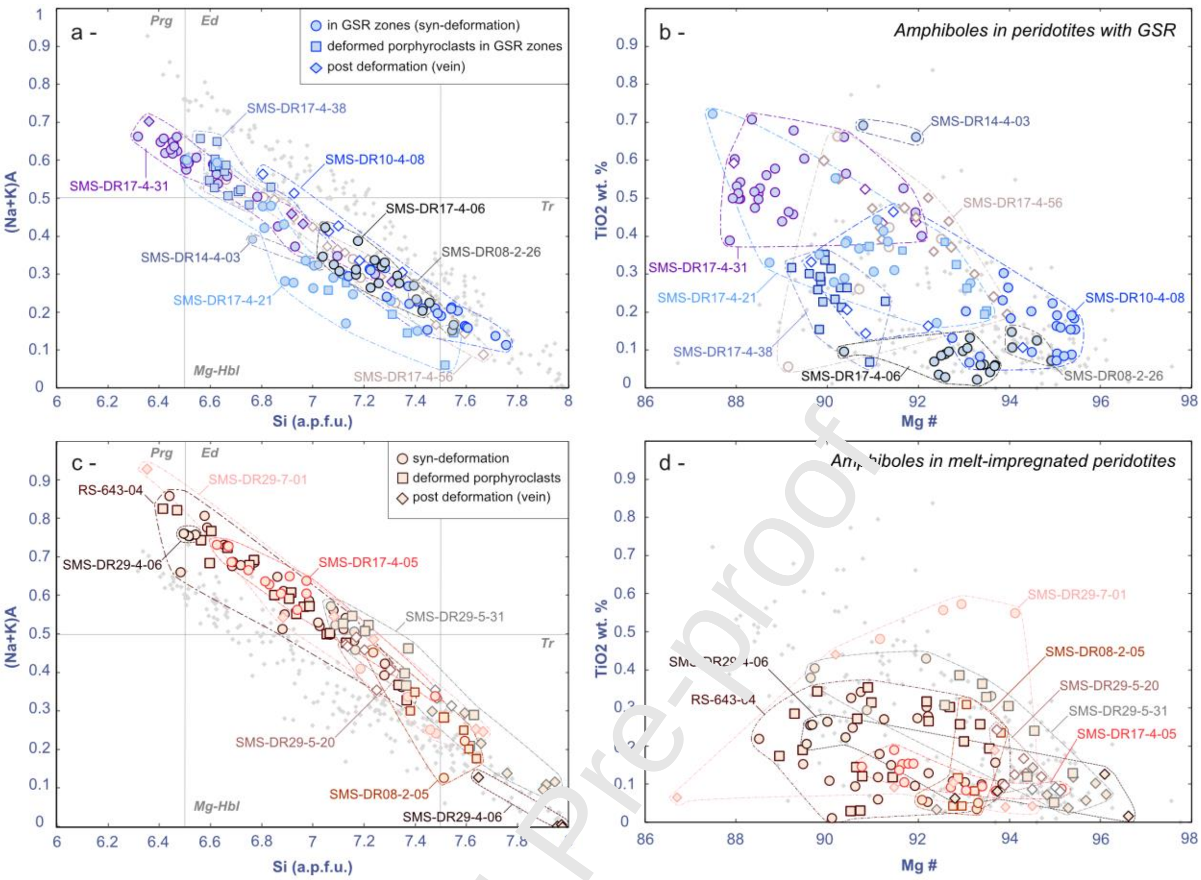

FIGURE 6: Amphibole compositions in (a, b) peridotites with amphibole-bearing GSR zones and (c, d) amphibole-bearing melt-impregnated peridotites. (a, c) Alkali versus Si content in atom per formula unit (a.p.f.u.). (b, d) TiO_2 (wt.%) versus Mg#. The grey data points represent the whole amphibole dataset presented in this study (Table A4). Abbreviations taken from Whitney and Evans (2010): pargasite (Prg), edenite (Ed), magnesiohornblende (Mg-Hbl), tremolite (Tr).

Journal Pre-proof

FIGURE 7

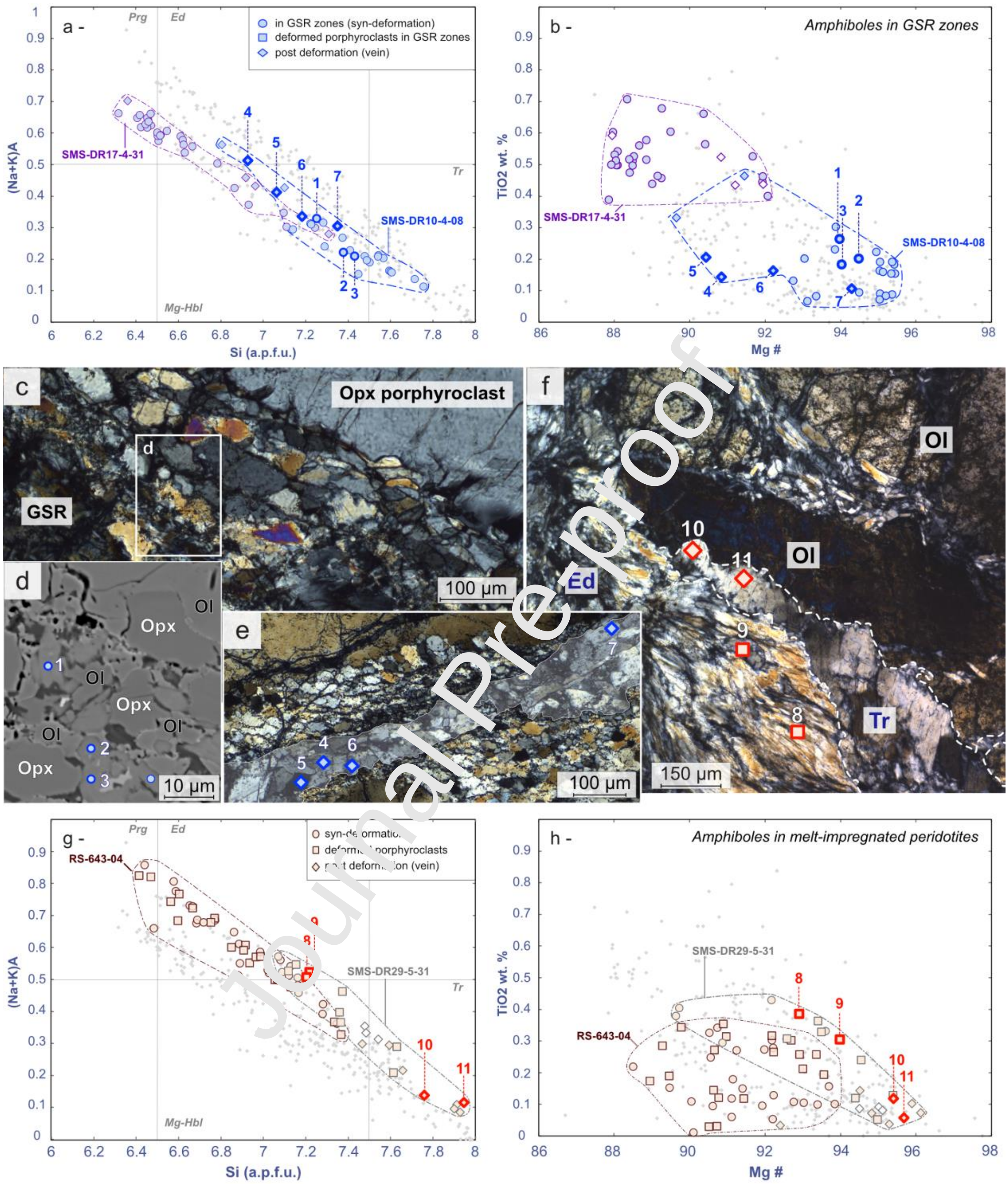

Journal Pre-proof

Figure 7: Intrasample variations in amphibole composition in (a-b) two samples with amphibole-bearing GSR zones (samples SMS-DR10-4-08 and SMS-DR17-4-31) and (g-h) two amphibole-bearing melt-impregnated peridotites (samples SMS-DR29-5-31 and RS-643-04, the latter shown in Fig. 2b, 4c). Corresponding microphotographs and SEM images in (c-f):

Journal Pre-proof

numbers correspond to measurements highlighted in the graphs (a-b, g-h) and reported in Table 1. (a, g) Alkali versus Si content in atom per formula unit (a.p.f.u.). (b, h) TiO_2 (wt.%) versus Mg#. The grey data points represent the whole amphibole dataset presented in this study (Table A4). (c) Microphotograph under polarized light of a polymineralic amphibole-bearing GSR zone along an orthopyroxene (Opx) porphyroclast (sample SMS-DR10-4-08). (d) Detail of the recrystallized assemblage composed of olivine (Ol), Orthopyroxene (Opx) and polygonal amphibole (blue points). (e) Amphibole vein crosscutting an olivine-rich GSR zone (see Figure 3e; same sample). (f) Amphibole microshear zone in an amphibole-bearing impregnated ultramafic sample, showing deformed crystals, rimmed by undeformed amphibole at contact with olivine (sample SMS-DR23-5-31).

Journal Pre-proof

Journal Pre-proof

FIGURE 8

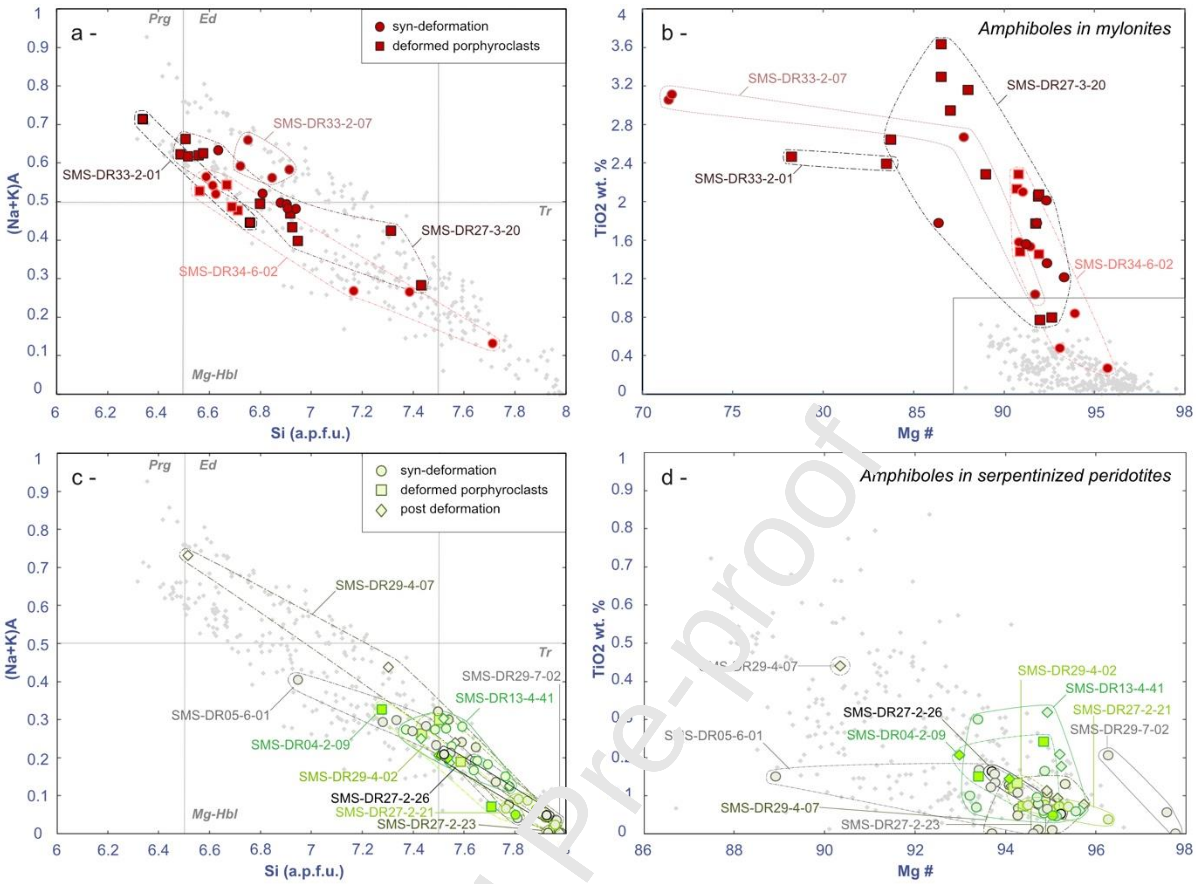

Figure 8: Amphibole compositions in (a, b) amphibole mylonites and (c, d) amphibole-bearing serpentinized peridotites. (a, c) Alkali versus Si content in atom per formula unit (a.p.f.u.). (b, d) TiO_2 (wt.%) versus Mg#. The grey data points represent the whole amphibole data set presented in this study (Table A4). Abbreviations taken from Whitney & Evans (2010): pargasite (Prg), edenite (Ed), magnesiohornblende (Mg-Hbl), tremolite (Tr).

Journal Pre-proof

FIGURE 9

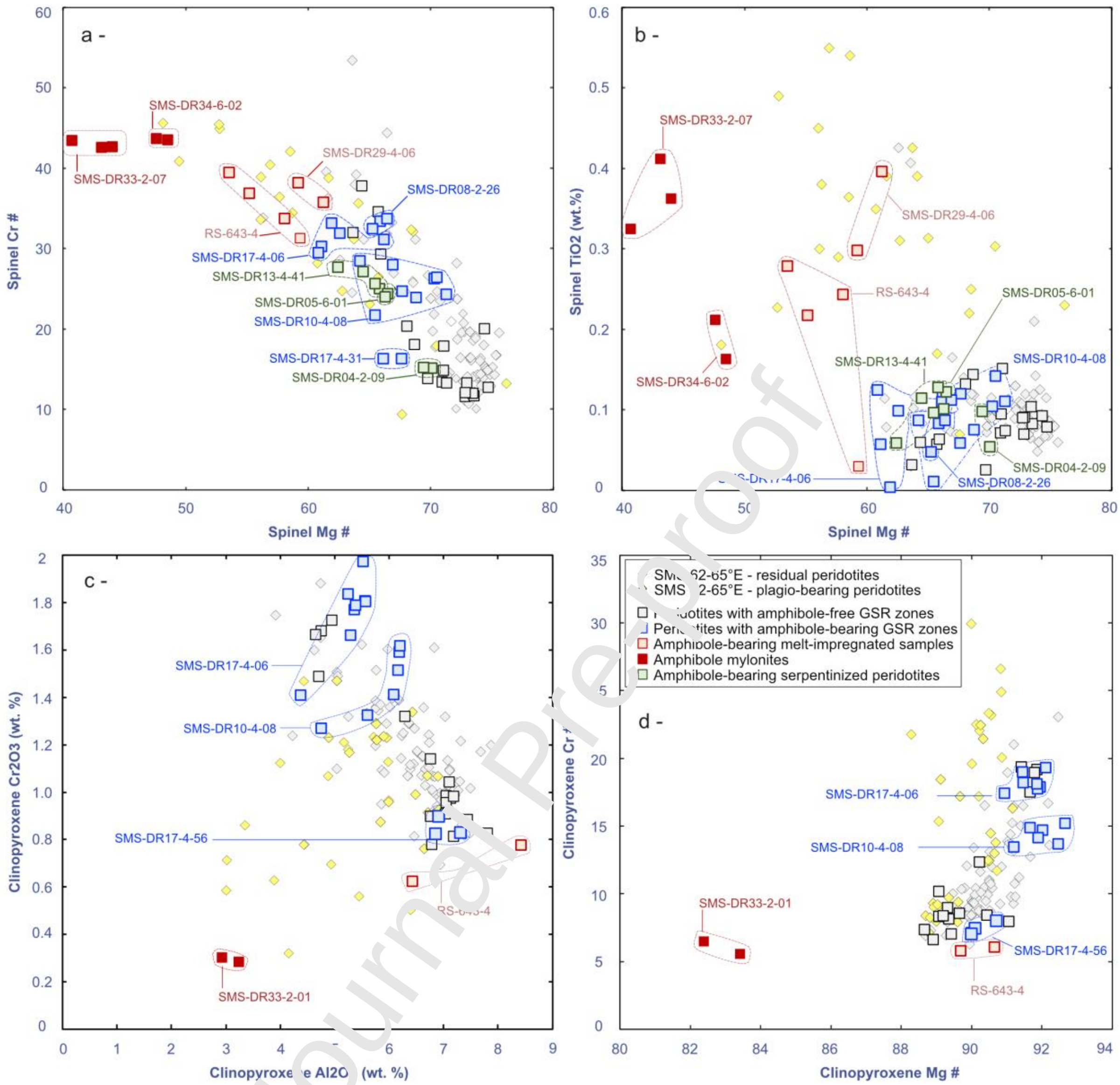

FIGURE 9: Spinel and clinopyroxene core compositions in amphibole-bearing samples (data in Tables A5-A6, respectively). (a) Spinel Cr# versus Mg# values. (b) Spinel TiO_2 (wt.%) versus Mg#. (c) Clinopyroxene Cr_2O_3 content (wt.%) vs Al_2O_3 (wt.%). (d) Clinopyroxene Mg# versus Cr# values. Residual and plagioclase-bearing peridotites from the Eastern SWIR (data from Seyler et al., 2003; Paquet et al., 2016 and unpublished data from D.Brunelli) are shown for comparison.

Journal Pre-proof

FIGURE 10

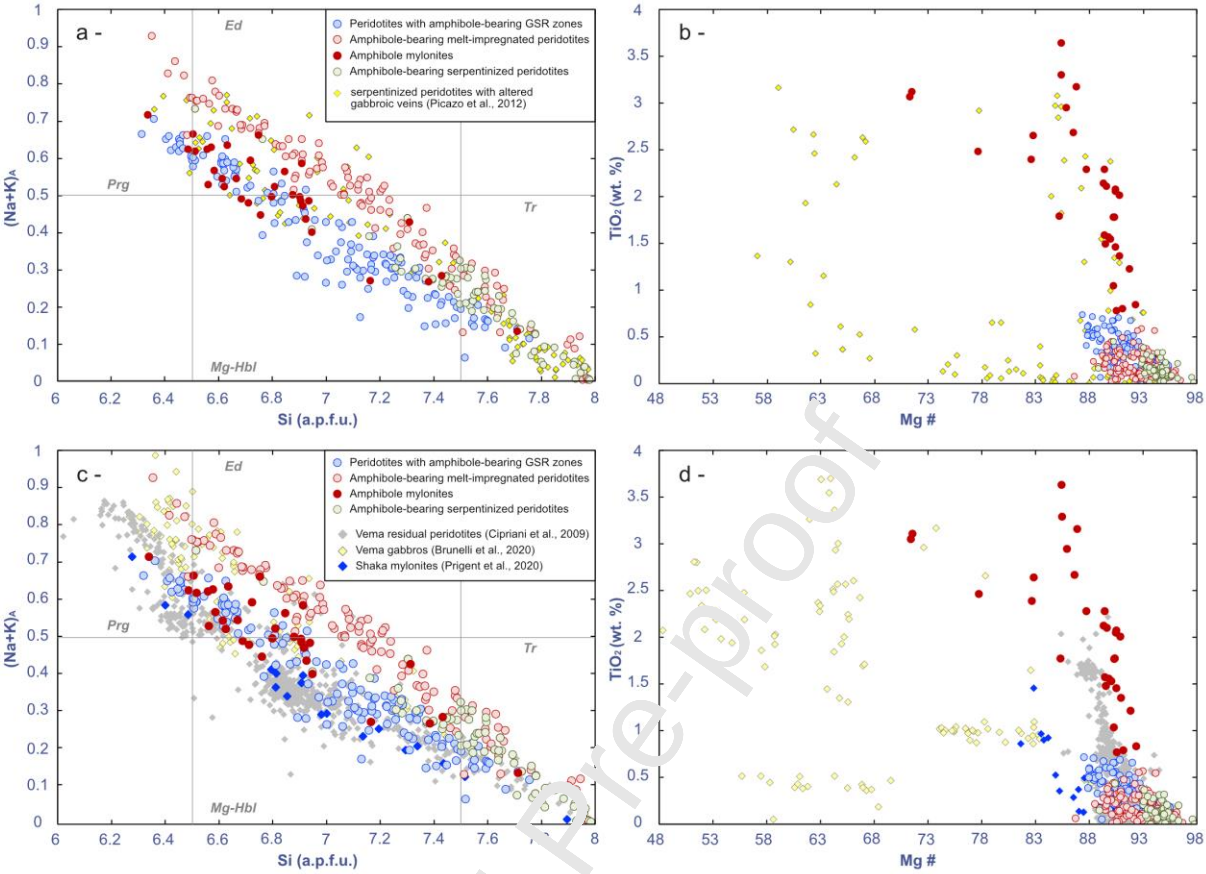

FIGURE 10: Compositional variability of amphiboles in SWIR amphibole-bearing samples (Table A4) compared to (a,b) amphibole-bearing serpentinized peridotites with altered gabbroic veins from the MAR at 15°N (Picazo et al., 2012) and (c, d) amphibole-bearing peridotites and gabbros from the Shaka (Prigent et al., 2020) and Vema Transform Zones (Cipriani et al., 2009; Brunelli et al., 2020). Color code is the same as in Figures 6-9. (a) alkali versus Si content in atom per formula unit (a.p.f.u.) and (b) TiO_2 (wt.%) versus Mg#. Abbreviations taken from Whitney & Evans (2010): pargasite (Prg), edenite (Ed), magnesiohornblende (Mg-Hbl), tremolite (Tr).

Journal Pre-proof

FIGURE 11

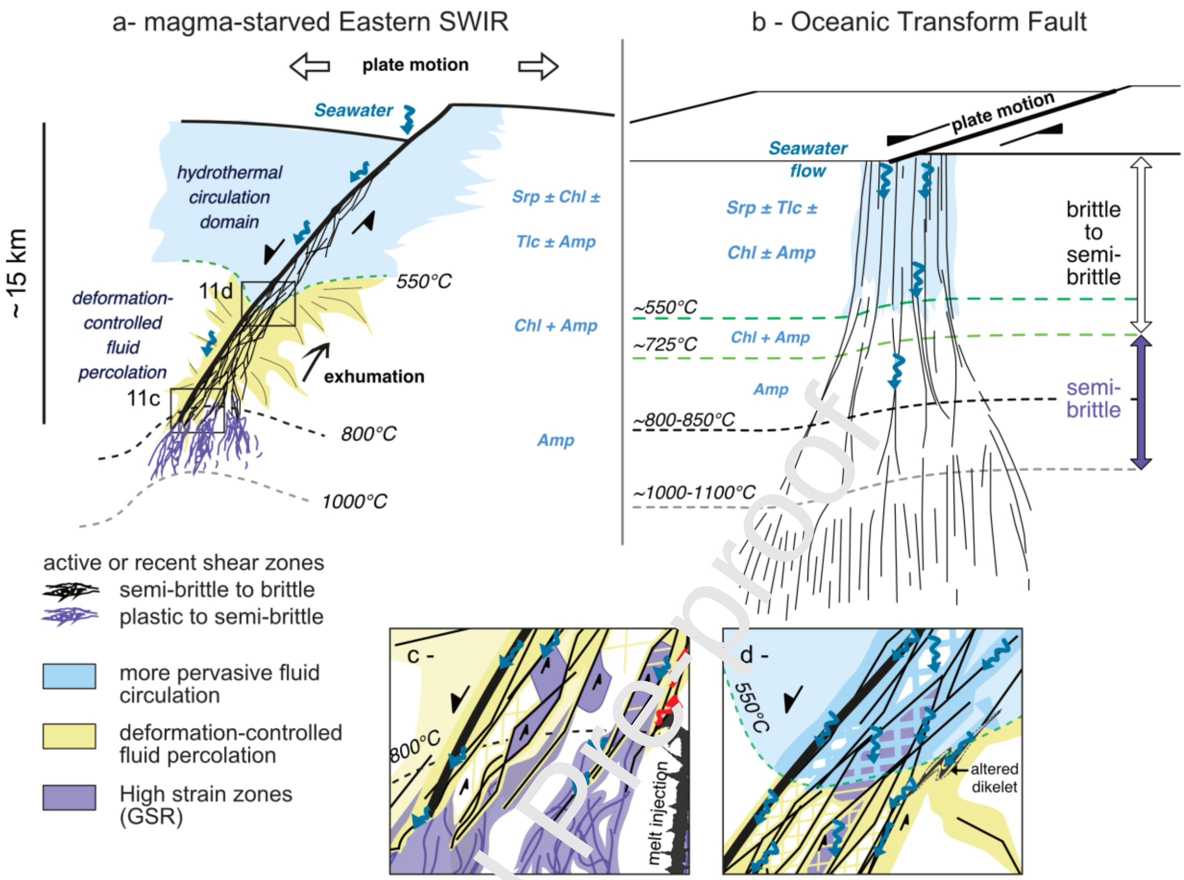

FIGURE 11: Interpretative sketches comparing hydration and deformation processes in the root zone of (a) the eastern SWIR detachment faults (modified after Bickert et al., 2021) and (b) oceanic transform faults (modified after Prigent et al., 2020). (c-d) are details of (a) showing fluid circulation (c) at the root zone of detachment faults and (d) at the transition to greenschist conditions. In (c), fractures and microfractures forming the detachment (black lines) root into a system of anastomosing plastic to semi brittle shear zones (dark purple), forming high strain zones (light purple). Locally, microfractures forming the detachment enclose blocks of deformed material, which will be progressively exhumed with fault activity. Seawater-derived fluids percolate through the network of microfractures forming the detachment and through mineral scale heterogeneities (blue arrows), while magma-derived

Journal Pre-proof

fluids move up along the deformation system (red arrows). In (d), as mantle blocks are exhumed along the network of faults forming the detachment, under greenschist conditions, hydration becomes more pervasive. Magmatic minerals from gabbroic dikelets form minerals weaker than serpentine, favoring strain localization and fluid focusing.

<u>SUPPLEMENTARY TABLES</u>

Table A1: Depths and positions of the dredges containing amphibole-bearing ultramafic rocks and of the one amphibole-bearing sample collected in-situ (sample RS-643-04). Dredges were done on- and off-axis during *Smoothseafloor* cruise (2010; doi: 10.17600/10200050). Positions are based on on-bottom/off-bottom positions and recalculated from ship positions. Sample RS-643-04 was recovered in-situ during *Rovsmooth* cruise (2016; doi:10.17600/16002000). Abbreviations: longitude (long.), and latitude (lat.).

Sampling method	Name	Long. E, Start	Lat. N, Start	Depth (m), Start	Long. E, End	Lat. N, End	Depth (m), End	Weight (kg)	Total number of samples	Number of peridotite samples
Dredge	DR02	62°30.26'E	28°40.89'S	-2979	[illegible]	28°41.29'S	-2476	512	19	19
Dredge	DR03	62°27.41'E	28°46.79'S	-3727	[illegible]	28°46.39'S	-3177	80	24	24
Dredge	DR04	62°25.63'E	28°56.57'S	-3673	[illegible]	28°57.19'S	-3224	14.60	12	12
Dredge	DR05	62°27.52'E	28°55.57'S	-2677	[illegible]	29°01.49'S	-3320	655	104	104
Dredge	DR06	62°29.13'E	28°31.87'S	[illegible]	[illegible]	28°31.52'S	-3238	166	57	22
Dredge	DR07	62°26.30'E	28°29.75'S	[illegible]	62°26.45'E	28°30.03'S	-3817	390	46	42
Dredge	DR08	62°35.13'E	28°31.29'S	[illegible]	62°35.25'E	28°30.55'S	-4370	722	48	30
Dredge	DR10	62°27.74'E	28°33.22 S	-4319	62°28.11'E	28°33.55'S	-3602	27	31	28
Dredge	DR11	62°33.09'E	28°03.09'S	[illegible]	62°33.30'E	28°03.40'S	-3145	60.1	39	38
Dredge	DR12	62°36.18'E	28°06.48'S	[illegible]	62°36.22'E	28°06.10'S	-3468	44	36	35
Dredge	DR13	62°34.74'E	[illegible]	[illegible]	62°34.24'E	28°10.16'S	-3608	122	43	42
Dredge	DR14	62°33.02'E	28°16.15'S	[illegible]	62°33.17'E	28°16.42'S	-3375	105	30	28
Dredge	DR15	62°28.55'E	[illegible]	-4298	62°28.46'E	28°15.34'S	-4059	234.2	33	28
Dredge	DR16	62°21.11'E	[illegible]	-4360	62°21.43'E	28°32.63'S	-3838	286	25	11
Dredge	DR17	[illegible]	[illegible]	-4963	62°31.19'E	28°23.86'S	-4392	235	101	82
Dredge	DR22	64°36.59'E	[illegible]	-4443	64°36.39'E	28°19.27'S	-3916	28	30	21
Dredge	DR23	64°38.00'E	[illegible]	-4252	64°38.00'E	28°13.55'S	-3785	61.5	14	0
Dredge	DR24	64°32.51'E	[illegible]	-4028	64°32.66'E	28°11.18'S	-3390	80	8	0
Dredge	DR25	64°37.80'E	28°18.08'S	-3762	64°37.10'E	28°17.41'S	-	0.7	1	1
Dredge	DR26	64°39.32'E	28°07.95'S	-4101	64°38.79'E	28°08.98'S	-3712	386	32	12
Dredge	DR27	64°31.19'E	27°.47.98'S	-3203	64°31.83'E	27°48.61'S	-2570	810	61	60
Dredge	DR28	64°37.22'E	27°56.80'S	-4760	64°38.02'E	27°57.41'S	-4542	90	19	14
Dredge	DR29	64°32.01'E	27°49.31'S	-2956	64°33.29'E	27°49.08'S	-2604	930	95	79
Dredge	DR30	64°33.41'E	27°32.54'S	-2950	64°33.39'E	27°33.12'S	-2734	90	14	13
Dredge	DR33	64°36.03'E	27°22.83'S	-2856	64°35.53'E	27°22.49'S	-2504	170	43	34
Dredge	DR34	64°36.98'E	27°30.29'S	-2928	64°37.73'E	27°29.54'S	-2583	400	77	69
Dredge	DR35	64°32.60'E	27°17.82'S	-4350	64°32.61'E	27°17.24'S	-3862	41.3	25	20
In-situ	RS-643-04	64°31.70'E	27°48.44'S	-2690	-	-	-		1	1

Journal Pre-proof

Table A2: Proportions of amphibole-bearing samples in a set of 386 ultramafic samples collected at the Eastern SWIR (62-65°E) during *Smoothseafloor* and *Rovsmooth* cruises (see text and caption of Table A1).

Dredge	Number of ultramafic samples	Samples with GSR zones	Amphibole in GSR zones	Chlorite-bearing samples	Chlorite-bearing samples with amphibole	Amphibole mylonites	Amphibole-bearing serpentinized peridotites
SMS-DR1	6	-	-	-	-	-	-
SMS-DR2	6	3	-	-	-	-	1
SMS-DR3	5	-	-	1	1	-	2
SMS-DR4	4	4	-	3	3	-	1
SMS-DR5	14	4	-	3	2	-	2
SMS-DR6	11	3	-	1	1	-	-
SMS-DR7	11	1	-	6	3	-	-
SMS-DR8	10	5	1	2	1	-	1
SMS-DR9	1	-	-	-	-	-	-
SMS-DR10	16	16	1	3	-	-	6
SMS-DR11	13	2	-	4	2	-	1
SMS-DR12	17	1	-	2	3	-	1
SMS-DR13	15	5	-	5	5	-	6
SMS-DR14	7	3	1	1	1	-	3
SMS-DR15	14	1	-	1	1	-	-
SMS-DR16	4	-	-	1	1	-	1
SMS-DR17	44	12	6	11	11	-	1
SMS-DR20	3	-	-	-	-	-	-
SMS-DR21	7	-	-	-	-	-	-
SMS-DR22	17	3	-	1	-	-	3
SMS-DR26	4	-	-	1	1	-	-
SMS-DR27	34	8	-	13	5	1	3
SMS-DR28	10	1	-	4	4	-	-
SMS-DR29	48	26	-	29	22	-	4
SMS-DR30	9	2	-	4	3	-	-
SMS-DR32	3	-	-	-	-	-	-
SMS-DR33	15	7	-	4	3	2	-
SMS-DR34	28	4	-	4	3	5	3
SMS-DR35	9	8	-	1	1	-	-
RS-643-4	1	1	-	1	1	-	-
TOTAL	386	120	9	106	78	8	39
Proportion	-	31%	2%	27%	20%	2%	10%

Journal Pre-proof

Table A3: Name, terminations of IGSN code (http://www.igsn.org), amphibole-bearing and textural types and characteristics of samples selected in this study. Samples with GSR zones differ from amphibole mylonites by the proportion of GSR: GSR zones are very localized and well below the 50-90% proportions of matrix that define a mylonite.

			Primary mineralogy				Deformation			Interaction with primary minerals		amp-rich domain			chl-bearing shear zones		Amp post-deformation	
sample	IGSN code*	Amphibole-bearing type	Olivine relicts	fresh px (>10%)	plagio	Magmatic amp	Texture	Deformation types (A0-A3)	GSR	Polygonal amp in GSR	Recryst. amp + ol	oriented tabular amp	deformed prismatic amp porphyroclasts	oriented fibrous amp	amp + chl	fibrous chl ± srp	unoriented amp	mineralization after px
SMS_DR08_02_26	3484	amphibole-bearing GSR zones	yes	yes			Porphyroclastic	A2	x	x								
SMS_DR10_04_08	3530	amphibole-bearing GSR zones	yes	yes			Porphyroclastic	A3	x	x						x	vein	
SMS_DR14_04_03	3683	amphibole-bearing GSR zones	yes	yes			Porphyroclastic	A2	x	x						x		amp+px
SMS_DR17_04_06	3792	amphibole-bearing GSR zones	yes	yes			Porphyroclastic	A2	x	x								amp
SMS_DR17_04_21	3807	amphibole-bearing GSR zones	yes	yes			Porphyroclastic	A3	x	x	x	x	x			x		amp
SMS_DR17_04_31	3817	amphibole-bearing GSR zones	yes	yes			Porphyroclastic	A3	x	x								
SMS_DR17_04_38	3824	amphibole-bearing GSR zones	-	yes			Protomylonite	A4	x	x			x			x		amp-chl
SMS_DR17_04_56	3842	amphibole-bearing GSR zones	yes	yes			Porphyroclastic	A2	x	prismatic ?		x					x	amp
RS_643_4	1104	impregnated amphibole-bearing peridotite	yes	no			Protomylonite	A3	x			x			x	?		amp-chl
SMS_DR08_02_05	3463	impregnated amphibole-bearing peridotite	yes	no			Porphyroclastic	A2-A3	x		?		x		x			amp-chl
SMS_DR17_04_05	3791	impregnated amphibole-bearing peridotite	yes	no			Porphyroclastic	A2	x		x	x						amp-(chl?)
SMS_DR29_04_06	4148	impregnated amphibole-bearing peridotite	yes	yes			Porphyroclastic	A1	-		x			x	x	x		chl ?
SMS_DR29_05_20	4176	impregnated amphibole-bearing peridotite	yes	yes			Porphyroclastic	A2	x		?	x			x	x		amp-chl
SMS_DR29_05_31	4187	impregnated amphibole-bearing peridotite	yes	no			Porphyroclastic	A1	-		x		x		x			amp-chl
SMS_DR29_07_01	4215	impregnated amphibole-bearing peridotite	yes	-	?		Porphyroclastic	A1	-		x	x			x			amp-chl
SMS_DR27_03_20	4084	amphibole mylonite	-	-		yes	Mylonite	A4	amp			x	x		x			amp
SMS_DR33_02_01	4271	amphibole mylonite	-	-	prehnite	yes	Mylonite	A4	amp	x								
SMS_DR33_02_07	4277	amphibole mylonite	-	no	?	yes	Mylonite	A4	amp				x		amp-tlc			
SMS_DR34_06_02	4383	amphibole mylonite	-	-		yes	Mylonite	A4	amp			x	x		x			
SMS_DR04_02_09	3235	serpentinized amphibole-bearing peridotite	no	yes			Porphyroclastic	A2-A3	x				x			x		amp
SMS_DR05_06_01	3321	serpentinized amphibole-bearing peridotite	no	yes			Porphyroclastic	A2-A3	x			x				x		amp
SMS_DR13_04_41	3675	serpentinized amphibole-bearing peridotite	no	no			Porphyroclastic	A3	x				x		?	x		amp
SMS_DR27_02_21	4058	serpentinized amphibole-bearing peridotite	no	no			Porphyroclastic	A0-A1				x	x	x		x		amp-chl
SMS_DR27_02_23	4060	serpentinized amphibole-bearing peridotite	no	no			Porphyroclastic	A0-A1				x				x		amp
SMS_DR27_02_26	4063	serpentinized amphibole-bearing peridotite	no	no			Porphyroclastic	A0-A1					x			x		amp
SMS_DR29_04_02	4144	serpentinized amphibole-bearing peridotite	no	no			Porphyroclastic	A1						x	x			amp
SMS_DR29_04_07	4149	serpentinized amphibole-bearing peridotite	yes	yes			Porphyroclastic	A1					x	x			x	amp-chl
SMS_DR29_07_02	4216	serpentinized amphibole-bearing peridotite	yes	-			Porphyroclastic	A1				x		x		x		amp-chl

*all IGSN codes start by: CNRS000000

Table A4: Amphibole composition for the four types of amphibole-bearing ultramafic samples and used for Fig. 6-8 and 10.

thin section	amphibole-bearing type	mineral	position	SiO2	TiO2	Al2O3	FeO	MnO	MgO	CaO	Na2O	K2O	Cr2O3	NiO	Cl	F	TOTAL	Mg#	Al T	(Na+K)A	Si
SMS_DR17_4_38	amphibole-bearing GSR zone	amphibole9	porphyroclast	46.68	0.35	12.03	3.72	0.09	18.67	11.61	2.67	0.04	0.46	0.11	0.07	0.00	96.50	89.94	1.37	0.65	6.63
SMS_DR17_4_38	amphibole-bearing GSR zone	amphibole10	porphyroclast	48.68	0.23	10.27	3.28	0.13	19.27	12.15	2.22	0.05	0.64	0.14	0.09	0.00	97.16	91.28	1.16	0.53	6.84
SMS_DR17_4_56	amphibole-bearing GSR zone	amphibole1	porphyroclast	52.09	0.45	6.06	3.23	0.02	20.68	12.74	1.19	0.02	0.61	0.09	0.07	0.00	97.25	91.95	0.73	0.29	7.27
SMS_DR17_4_56	amphibole-bearing GSR zone	amphibole2	porphyroclast	50.14	0.47	8.05	3.49	0.05	19.76	13.03	1.67	0.05	0.87	0.18	0.13	0.00	97.89	90.98	1.00	0.42	7.00
SMS_DR17_4_56	amphibole-bearing GSR zone	amphibole3	porphyroclast	51.38	0.36	7.42	2.97	0.03	20.11	13.08	1.53	0.01	0.87	0.10	0.12	0.00	97.99	92.34	0.87	0.36	7.13
SMS_DR17_4_56	amphibole-bearing GSR zone	amphibole4	neoblast	47.17	0.06	10.53	4.32	0.08	19.87	11.92	2.04	0.04	0.98	0.14	0.13	0.00	97.28	89.14	1.33	0.57	6.67
SMS_DR17_4_56	amphibole-bearing GSR zone	amphibole4	neoblast	48.85	0.26	10.07	3.59	0.06	19.62	13.17	1.87	0.02	0.31	0.02	0.21	0.00	98.05	90.70	1.19	0.50	6.81
SMS_DR17_4_56	amphibole-bearing GSR zone	amphibole5	neoblast	52.60	0.37	6.86	3.57	0.03	21.15	13.19	1.28	0.00	0.76	0.04	0.12	0.00	99.98	91.35	0.84	0.34	7.16
SMS_DR17_4_56	amphibole-bearing GSR zone	amphibole6	neoblast	47.36	0.66	10.98	3.67	0.00	19.00	12.71	2.04	0.03	0.84	0.13	0.13	0.00	97.56	90.22	1.34	0.55	6.66
SMS_DR17_4_56	amphibole-bearing GSR zone	amphibole7	neoblast	52.84	0.50	6.57	3.17	0.03	21.08	13.52	1.35	0.02	0.79	0.05	0.15	0.00	100.06	92.21	0.82	0.33	7.18
SMS_DR17_4_56	amphibole-bearing GSR zone	amphibole8	neoblast	51.58	0.44	6.02	2.95	0.00	20.92	12.94	1.24	0.02	0.79	0.12	0.07	0.00	97.09	92.67	0.78	0.34	7.22
SMS_DR17_4_56	amphibole-bearing GSR zone	amphibole9	post	50.36	0.39	8.30	3.37	0.01	19.59	12.92	1.46	0.07	0.47	0.10	0.06	0.00	97.11	91.19	0.94	0.37	7.06
SMS_DR17_4_56	amphibole-bearing GSR zone	amphibole10	post	54.23	0.30	4.58	2.78	0.01	21.45	12.82	0.76	0.05	0.48	0.15	0.08	0.00	97.68	93.22	0.52	0.17	7.48
SMS_DR17_4_56	amphibole-bearing GSR zone	amphibole11	neoblast	52.99	0.39	5.85	2.98	0.09	20.61	13.04	1.07	0.00	0.74	0.09	0.11	0.00	97.96	92.50	0.68	0.22	7.32
SMS_DR17_4_56	amphibole-bearing GSR zone	amphibole12	neoblast	52.10	0.42	6.93	3.43	0.03	20.35	12.99	1.25	0.05	0.73	0.11	0.13	0.00	98.51	91.36	0.81	0.29	7.19
SMS_DR17_4_56	amphibole-bearing GSR zone	amphibole13	vein	50.01	0.55	8.96	3.82	0.05	19.81	12.65	1.77	0.04	0.87	0.16	0.09	0.00	98.78	90.24	1.08	0.45	6.92
SMS_DR17_4_56	amphibole-bearing GSR zone	amphibole14	vein	49.12	0.60	9.15	3.92	0.00	19.59	12.79	1.86	0.02	1.13	0.07	0.09	0.00	98.35	89.92	1.15	0.50	6.85
SMS_DR17_4_56	amphibole-bearing GSR zone	amphibole15	vein	51.18	0.42	7.35	3.50	0.08	20.24	12.88	1.45	0.07	0.93	0.07	0.13	0.00	98.31	91.16	0.91	0.37	7.09
SMS_DR17_4_56	amphibole-bearing GSR zone	amphibole16	vein	53.40	0.37	4.91	3.01	0.00	21.50	13.17	1.15	0.03	0.85	0.14	0.10	0.00	98.63	92.72	0.66	0.29	7.34
SMS_DR17_4_56	amphibole-bearing GSR zone	amphibole17	vein	55.89	0.19	3.30	2.52	0.06	21.91	12.79	0.56	0.03	0.35	0.17	0.05	0.00	97.84	93.95	0.33	0.09	7.67
SMS_DR17_4_56	amphibole-bearing GSR zone	amphibole18	vein	55.92	0.24	3.88	2.69	0.03	22.20	13.04	0.70	0.02	0.11	0.07	0.05	0.00	98.93	93.65	0.41	0.14	7.59
SMS_DR17_4_56	amphibole-bearing GSR zone	amphibole19	vein	52.05	0.47	5.92	3.31	0.03	20.50	12.94	1.22	0.06	0.90	0.16	0.09	0.00	97.65	91.69	0.75	0.30	7.25
RS_643_4	amphibole-bearing melt-impregnated peridotite	amphibole 1	porphyroclast	48.04	0.03	10.98	3.77	0.04	20.19	12.62	2.64	0.07	0.41	0.11	0.07	0.00	98.98	90.51	1.33	0.72	6.67
RS_643_4	amphibole-bearing melt-impregnated peridotite	amphibole 2	neoblast	52.63	0.16	5.35	2.70	0.06	22.52	11.97	1.47	0.01	0.77	0.07	0.09	0.00	97.79	93.69	0.72	0.39	7.28
RS_643_4	amphibole-bearing melt-impregnated peridotite	amphibole 3	neoblast	46.13	0.01	13.33	3.86	0.12	19.69	11.63	3.20	0.15	0.21	0.03	0.10	0.00	98.46	90.10	1.56	0.86	6.44
RS_643_4	amphibole-bearing melt-impregnated peridotite	amphibole 4	porphyroclast	47.57	0.03	11.56	3.57	0.00	19.60	12.49	2.97	0.05	1.02	0.13	0.08	0.00	99.07	90.73	1.39	0.77	6.61
RS_643_4	amphibole-bearing melt-impregnated peridotite	amphibole 5	neoblast	45.54	0.22	8.87	5.36	0.00	23.15	8.90	2.31	0.12	2.81	0.14	0.05	0.00	97.46	88.51	1.49	0.66	6.49
RS_643_4	amphibole-bearing melt-impregnated peridotite	amphibole 6	neoblast	47.46	0.09	11.70	3.69	0.05	19.99	12.25	3.12	0.06	0.54	0.10	0.13	0.00	99.18	90.61	1.42	0.81	6.58
RS_643_4	amphibole-bearing melt-impregnated peridotite	amphibole 7	neoblast	47.31	0.06	11.43	3.61	0.07	20.76	11.56	2.84	0.06	0.56	0.14	0.11	0.00	98.50	91.12	1.41	0.78	6.59
RS_643_4	amphibole-bearing melt-impregnated peridotite	amphibole 8	neoblast	47.72	0.25	10.64	3.65	0.01	19.64	12.12	2.71	0.00	1.03	0.04	0.12	0.00	97.94	90.56	1.31	0.68	6.69
RS_643_4	amphibole-bearing melt-impregnated peridotite	amphibole 9	neoblast	53.50	0.10	5.59	2.78	0.00	22.06	12.57	1.83	0.04	1.00	0.07	0.08	0.00	99.63	93.40	0.72	0.42	7.28
RS_643_4	amphibole-bearing melt-impregnated peridotite	amphibole 10	neoblast	51.59	0.10	8.32	3.27	0.11	20.87	12.73	2.23	0.02	0.67	0.01	0.09	0.00	99.99	91.92	0.97	0.52	7.03
RS_643_4	amphibole-bearing melt-impregnated peridotite	amphibole 11	neoblast	51.30	0.11	7.93	2.79	0.11	20.87	12.48	2.16	0.01	0.66	0.14	0.09	0.00	98.64	93.03	0.93	0.50	7.07
RS_643_4	amphibole-bearing melt-impregnated peridotite	amphibole 12	neoblast	50.33	0.15	7.88	3.42	0.05	20.39	12.94	1.98	0.03	0.66	0.04	0.06	0.00	97.92	91.40	0.98	0.53	7.02
RS_643_4	amphibole-bearing melt-impregnated peridotite	amphibole 13	neoblast	51.64	0.18	6.60	3.57	0.00	20.61	12.87	1.99	0.06	0.67	0.12	0.09	0.00	98.39	91.15	0.84	0.48	7.16
RS_643_4	amphibole-bearing melt-impregnated peridotite	amphibole 14	porphyroclast	49.90	0.12	8.03	3.74	0.03	20.66	12.56	2.12	0.03	0.55	0.09	0.13	0.00	97.96	90.77	1.03	0.57	6.97
RS_643_4	amphibole-bearing melt-impregnated peridotite	amphibole 15	porphyroclast	49.91	0.14	7.84	3.75	0.02	20.37	12.57	2.20	0.04	0.74	0.07	0.10	0.00	97.75	90.63	1.01	0.57	6.99
RS_643_4	amphibole-bearing melt-impregnated peridotite	amphibole 16	neoblast	47.27	0.15	10.12	4.16	0.00	19.83	13.11	2.65	0.05	0.62	0.05	0.11	0.00	98.12	89.47	1.35	0.73	6.65

Table A5: Spinel composition for the four types of amphibole-bearing ultramafic samples and used for Fig. 9a-b.

Sample	amphibole-bearing type	Mineral	Position	SiO2	TiO2	Al2O3	Cr2O3	FeO	MnO	MgO	NiO	Total		Mg#	Cr#	Mg#(Fe2)
SMS_DR08_2_26	amphibole-bearing GSR zone	spinel 2	core	0.00	0.08	39.06	29.29	14.66	0.00	15.88	0.24	99.21		67.63	33.46	65.88
SMS_DR08_2_26	amphibole-bearing GSR zone	spinel 2b	core	0.04	0.05	39.54	28.37	14.72	0.00	15.51	0.20	98.42		66.41	32.49	65.27
SMS_DR08_2_26	amphibole-bearing GSR zone	spinel 2b	core	0.04	0.09	39.12	29.76	14.12	0.00	15.67	0.03	98.82		66.62	33.78	66.43
SMS_DR10_4_8A	amphibole-bearing GSR zone	spinel 1	core	0.10	0.01	48.04	19.88	14.79	0.00	15.73	0.21	98.75		64.98	21.72	65.47
SMS_DR10_4_8A	amphibole-bearing GSR zone	spinel 3	core	0.04	0.08	46.50	21.78	13.61	0.00	16.84	0.25	99.09		69.40	23.90	68.81
SMS_DR10_4_8A	amphibole-bearing GSR zone	spinel 3	core	0.08	0.12	45.93	22.52	14.00	0.00	16.46	0.24	99.35		67.84	24.75	67.70
SMS_DR10_4_8A	amphibole-bearing GSR zone	spinel 2	core	0.03	0.11	46.77	22.40	12.27	0.00	17.11	0.22	98.92		70.38	24.31	71.31
SMS_DR10_4_8A	amphibole-bearing GSR zone	spinel 2	core	0.20	0.09	42.66	25.30	14.91	0.00	15.02	0.29	98.47		63.51	28.46	64.22
SMS_DR10_4_8A	amphibole-bearing GSR zone	spinel 3	core	0.01	0.10	44.64	23.78	12.90	0.00	17.12	0.12	98.66		70.96	26.33	70.29
SMS_DR10_4_8A	amphibole-bearing GSR zone	spinel 4	core	0.03	0.11	43.84	25.45	14.03	0.00	15.90	0.08	99.43		66.14	28.02	66.90
SMS_DR10_4_8A	amphibole-bearing GSR zone	spinel 2b	core	0.03	0.14	44.66	23.90	12.91	0.00	17.33	0.09	99.06		71.39	26.42	70.53
SMS_DR17_4_6	amphibole-bearing GSR zone	spinel 1	core	0.06	0.10	39.26	27.44	16.50	0.00	15.50	0.28	99.14		66.04	31.91	62.61
SMS_DR17_4_6	amphibole-bearing GSR zone	spinel 2	core	0.03	0.06	40.27	26.06	16.56	0.00	14.60	0.18	97.75		63.00	30.27	61.13
SMS_DR17_4_6	amphibole-bearing GSR zone	spinel 1b	core	0.04	0.12	41.16	27.73	14.63	0.00	16.08	0.11	99.87		67.20	31.12	66.20
SMS_DR17_4_6	amphibole-bearing GSR zone	spinel 3	core	0.06	0.13	41.29	25.77	17.26	0.00	15.06	0.09	99.64		63.31	29.51	60.87
SMS_DR17_4_6	amphibole-bearing GSR zone	spinel 4	core	0.02	0.00	38.34	28.45	16.48	0.00	15.03	0.19	98.51		64.84	33.23	61.91
SMS_DR17_4_31	amphibole-bearing GSR zone	spinel	core	0.05	0.11	52.06	15.13	16.05	0.00	17.58	0.30	101.27		69.57	16.31	66.13
SMS_DR17_4_31	amphibole-bearing GSR zone	spinel 62	core	0.00	0.06	51.32	14.94	14.82	0.00	17.40	0.29	98.84		70.50	16.34	67.67
SMS_DR17_4_31	amphibole-bearing GSR zone	spinel 62	rim	0.00	0.03	51.74	14.61	15.41	0.00	17.19	0.40	99.38		69.56	15.92	66.53
RS_643_4	amphibole-bearing melt-impregnated peridotite	spinel	core	0.05	0.28	32.59	31.63	20.78	0.00	13.45	0.15	98.93		59.18	39.43	53.57
RS_643_4	amphibole-bearing melt-impregnated peridotite	spinel	core	0.00	0.24	37.14	28.15	18.89	0.00	[illegible]	0.12	99.22		62.98	33.70	58.08
RS_643_4	amphibole-bearing melt-impregnated peridotite	spinel	core	0.00	0.22	34.57	30.11	19.84	0.00	[illegible]	0.14	98.60		60.14	36.87	55.21
RS_643_4	amphibole-bearing melt-impregnated peridotite	spinel	core	0.02	0.03	39.20	26.59	18.34	0.00	[illegible]	0.17	99.39		64.12	31.27	59.38
SMS_DR29_4_6	amphibole-bearing melt-impregnated peridotite	spinel1	core1	0.02	0.40	35.96	29.91	16.93	0.00	15.01	[illegible]	98.40		64.85	35.81	61.26
SMS_DR29_4_6	amphibole-bearing melt-impregnated peridotite	spinel1 - RIM	rim1	0.00	0.30	34.54	31.88	17.44	0.00	[illegible]	[illegible]	98.53		62.09	38.23	59.23
SMS_DR33_2_7	amphibole mylonite	spinel1	core?	0.01	0.41	29.12	32.21	25.88	0.00	11.03	0.18	98.83		49.89	42.59	43.17
SMS_DR33_2_7	amphibole mylonite	spinel1	core?	0.02	0.32	28.48	32.63	26.75	0.00	[illegible]	0.17	98.69		47.17	43.45	40.76
SMS_DR33_2_7	amphibole mylonite	spinel1	core?	0.05	0.36	28.89	31.99	25.32	[illegible]	[illegible]	0.35	98.15		51.09	42.61	44.06
SMS_DR34_6_2	amphibole mylonite	spinel1	core?	0.07	0.16	29.81	34.27	21.84	[illegible]	[illegible]	0.14	97.87		52.65	43.54	48.57
SMS_DR34_6_2	amphibole mylonite	spinel1 - RIM	rim	0.00	0.21	30.03	34.67	22.64	[illegible]	[illegible]	0.15	99.26		52.05	43.64	47.67
SMS_DR04_2_9	amphibole-bearing serpentinized peridotite	spinel	core1	0.00	0.05	53.03	14.13	13.57	0.00	17.84	0.30	98.91		71.69	15.16	70.10
SMS_DR04_2_9	amphibole-bearing serpentinized peridotite	spinel	core1	0.05	0.10	53.41	14.32	13.99	[illegible]	17.83	0.30	100.01		70.84	15.24	69.44
SMS_DR05_6_1	amphibole-bearing serpentinized peridotite	spinel1	core1	0.00	0.12	45.84	22.11	[illegible]	[illegible]	16.43	0.30	99.54		67.91	24.44	66.53
SMS_DR05_6_1	amphibole-bearing serpentinized peridotite	spinel 1	core1	0.06	0.10	46.23	21.83	[illegible]	0.00	16.44	0.31	99.86		67.61	24.06	66.31

Journal Pre-proof

Table A6: Clinopyroxene composition for the four types of amphibole-bearing ultramafic samples and used for Fig. 9c-d.

thin section	amphibole-bearing type	mineral	position	[illegible]	TiO	[illegible]	-	FeO	MnO	MgO	CaO	Na2O	K2O	-	Cr2O3	NiO	Cl	F	Total	-	Al T	Al Oct	XMg	XCr	Ca	Na	Ti	-	Mg#	Cr#
SMS_DR10_4_8A	amphibole-bearing GSR zone	cpx 2b	core	[illegible]	[illegible]	[illegible]		2.38	0.23	15.22	21.23	1.05	0.02		1.41	0.07	0.00		100.43		0.106	0.152	0.912	0.13	0.82	0.07	0.00		91.20	13.47
SMS_DR10_4_8A	amphibole-bearing GSR zone	cpx 2c	core	50.64	[illegible]	[illegible]		2.23	0.08	14.70	22.00	1.02	0.00		1.52	0.03	0.00		98.65		0.134	0.134	0.919	0.14	0.87	0.07	0.01		91.89	14.17
SMS_DR10_4_8A	amphibole-bearing GSR zone	cpx 2c	core	[illegible]	[illegible]	[illegible]		2.29	0.00	14.82	22.22	0.98	0.00		1.59	0.01	0.00		98.91		0.139	0.129	0.920	0.15	0.88	0.07	0.01		92.01	14.72
SMS_DR10_4_8A	amphibole-bearing GSR zone	cpx 2c	core	[illegible]	[illegible]	6.20		2.39	0.10	15.36	21.22	0.96	0.02		1.62	0.06	0.02		99.87		0.124	0.141	0.917	0.15	0.82	0.07	0.01		91.66	14.90
SMS_DR10_4_8A	amphibole-bearing GSR zone	cpx	core	53.34	[illegible]	4.74		2.09	0.16	15.89	21.96	0.87	0.00		1.27	0.10	0.00		100.66		0.083	0.118	0.927	0.15	0.85	0.06	0.01		92.65	15.22
SMS_DR17_4_56	amphibole-bearing GSR zone	cpx 1	[illegible]	[illegible]	0.51	6.85		3.06	0.08	16.07	21.28	0.89	0.00		0.83	0.07	0.00		101.40		0.148	0.141	0.901	0.07	0.82	0.06	0.01		90.10	7.48
SMS_DR17_4_56	amphibole-bearing GSR zone	cpx 1	[illegible]	[illegible]	0.46	7.31		3.16	0.05	16.20	20.45	0.88	0.00		0.83	0.08	0.02		100.39		0.161	0.150	0.900	0.07	0.79	0.06	0.01		89.99	7.08
SMS_DR17_4_56	amphibole-bearing GSR zone	cpx 1b	[illegible]	50.26	0.43	6.90		2.75	0.04	15.28	21.93	0.68	0.04		0.90	0.05	0.00		99.26		0.159	0.139	0.907	0.08	0.86	0.05	0.01		90.70	8.02
SMS_DR17_4_56	amphibole-bearing GSR zone	opx 1	core	55.69	0.09	4.51		6.70	0.08	32.36	0.78	0.01	0.00		0.43	0.17	0.01		100.84		0.090	0.092	0.895	0.06	0.03	0.00	0.00		89.47	6.04
SMS_DR17_4_6	amphibole-bearing GSR zone	cpx 1	[illegible]	52.93	0.11	5.24		2.80	0.02	16.96	19.12	1.32	0.00		1.84	0.04	0.00		100.38		0.097	0.125	0.915	0.19	0.74	0.09	0.00		91.45	19.03
SMS_DR17_4_6	amphibole-bearing GSR zone	cpx 3	[illegible]	52.82	0.10	5.29		3.34	0.04	19.03	16.39	1.08	0.00		1.66	0.07	0.00		99.82		0.102	0.122	0.909	0.17	0.63	0.08	0.00		90.93	17.43
SMS_DR17_4_6	amphibole-bearing GSR zone	cpx 3	core	52.16	0.08	5.55		2.48	0.00	15.81	20.47	1.42	0.03		1.81	0.07	0.00		99.88		0.108	0.129	0.919	0.18	0.80	0.10	0.00		91.92	17.92
SMS_DR17_4_6	amphibole-bearing GSR zone	[illegible]	[illegible]	53.78	0.13	4.37		2.68	0.02	17.13	19.62	1.17	0.00		1.41	0.06	0.00		100.36		0.069	0.116	0.919	0.18	0.75	0.08	0.00		91.88	17.78
SMS_DR17_4_6	amphibole-bearing GSR zone	cpx 4	core	52.17	0.15	5.52		2.20	0.03	14.61	21.69	1.41	0.00		1.97	0.00	0.00		99.75		0.102	0.135	0.921	0.19	0.85	0.10	0.00		92.11	19.36
SMS_DR17_4_6	amphibole-bearing GSR zone	cpx 4	[illegible]	52.23	0.12	5.56		2.42	0.03	15.65	20.61	1.35	0.00		1.81	0.04	0.00		99.82		0.105	0.132	0.919	0.18	0.80	0.09	0.00		91.94	17.89
SMS_DR17_4_6	amphibole-bearing GSR zone	[illegible]	[illegible]	52.04	0.11	5.36		2.54	0.01	16.19	20.32	1.22	0.00		1.77	0.04	0.00		99.62		0.109	0.121	0.919	0.18	0.79	0.09	0.00		91.86	18.14
SMS_DR17_4_6	amphibole-bearing GSR zone	[illegible]	[illegible]	52.87	0.11	5.38		2.88	0.02	17.41	18.25	1.19	0.03		1.79	0.04	0.00		99.95		0.097	0.132	0.915	0.18	0.70	0.08	0.00		91.46	18.24
RS_643_4	amphibole-bearing melt-impregnated peridotite	[illegible]	core	50.14	0.21	8.42		3.06	0.08	15.26	22.61	0.79	0.01		0.78	0.03	0.06		101.43		0.198	0.159	0.897	0.06	0.87	0.05	0.01		89.68	5.82
RS_643_4	amphibole-bearing melt-impregnated peridotite	[illegible]	core	51.64	0.16	6.43		2.94	0.02	16.12	22.41	0.74	0.02		0.62	0.08	0.08		101.26		0.146	0.126	0.907	0.06	0.86	0.05	0.00		90.65	6.11
SMS_DR33_2_1	amphibole mylonite	[illegible]	core	52.63	0.55	3.23		5.64	0.18	16.42	20.97	0.60	0.01		0.28	0.02	0.00	0.04	100.57		0.08	0.06	0.83	0.06	0.82	0.04	0.02		83.41	5.58
SMS_DR33_2_1	amphibole mylonite	cpx3	core	53.18	0.49	2.93		6.21	0.22	16.86	19.78	0.57	0.02		0.30	0.07	0.00	0.00	100.63		0.07	0.06	0.82	0.07	0.77	0.04	0.01		82.37	6.51
SMS_DR04_2_9	amphibole-bearing serpentinized peridotite	opx1	core	54.66	0.10	5.85		6.55	0.07	32.08	0.74	0.03	0.01		0.64	0.07	0.00	0.08	100.88		0.13	0.11	0.90	0.07	0.03	0.00	0.00		89.62	6.86
SMS_DR04_2_9	amphibole-bearing serpentinized peridotite	opx1	core	54.25	0.09	5.78		7.07	0.15	31.42	0.77	0.03	0.03		0.83	0.04	0.00	0.06	100.52		0.13	0.11	0.89	0.09	0.03	0.00	0.00		88.57	8.81
SMS_DR05_6_1	amphibole-bearing serpentinized peridotite	opx1	core	55.04	0.05	4.57		6.02	0.07	32.57	0.81	0.06	0.01		0.76	0.15	0.03	0.00	100.14		0.10	0.08	0.91	0.10	0.03	0.00	0.00		90.51	10.09
SMS_DR05_6_1	amphibole-bearing serpentinized peridotite	opx1	core	55.86	0.09	4.33		5.76	0.04	32.79	0.66	0.03	0.01		0.88	0.06	0.02	0.06	100.59		0.09	0.09	0.91	0.12	0.02	0.00	0.00		90.96	11.97
SMS_DR29_4_2	amphibole-bearing serpentinized peridotite	cpx1	core	55.72	0.01	0.10		2.13	0.04	17.77	25.61	0.02	0.00		0.00	0.02	0.00	0.00	101.43		0.00	0.00	0.94	0.00	0.98	0.00	0.00		93.59	0.00
SMS_DR29_4_2	amphibole-bearing serpentinized peridotite	cpx2	core	55.36	0.05	0.04		2.88	0.16	17.20	25.05	0.00	0.01		0.01	0.06	0.02	0.00	100.85		0.00	0.00	0.91	0.15	0.97	0.00	0.00		90.96	15.12

SUPPLEMENTARY FIGURES

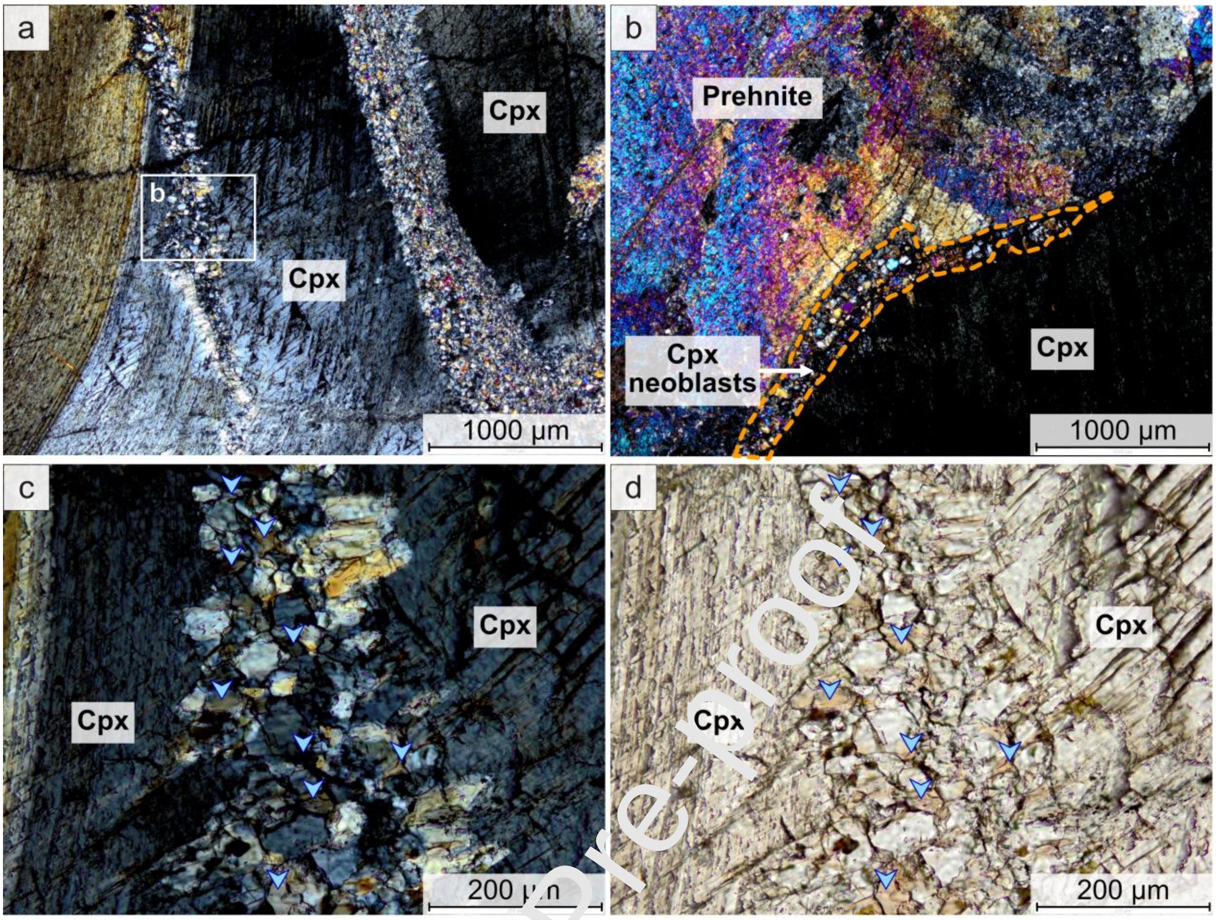

Figure A1: Microphotographs under cross-polarized light (a-c) and natural light (d) of amphibole in an amphibole-bearing mylonite (SMS-DR33-2-01). (a) Coarse, ductilely deformed and partially recrystallized porphyroclasts of clinopyroxene (Cpx). (b) Large prehnite grains coexisting with clinopyroxene. Recrystallization occurs along the two-phase grain boundaries. (c-d) Detail of (a) showing neoblasts of clinopyroxene recrystallizing together with brown amphibole (pointed by blue arrows) .

Highlights

- Synkinematic amphiboles crystallized at the root of Eastern SWIR axial detachments.
- Seawater-derived fluids percolate along the detachment down to the BDT.
- Variations in amphibole composition are controlled by the protolith.
- Deep fluid percolation is controlled by detachment fault activity.

Journal Pre-proof

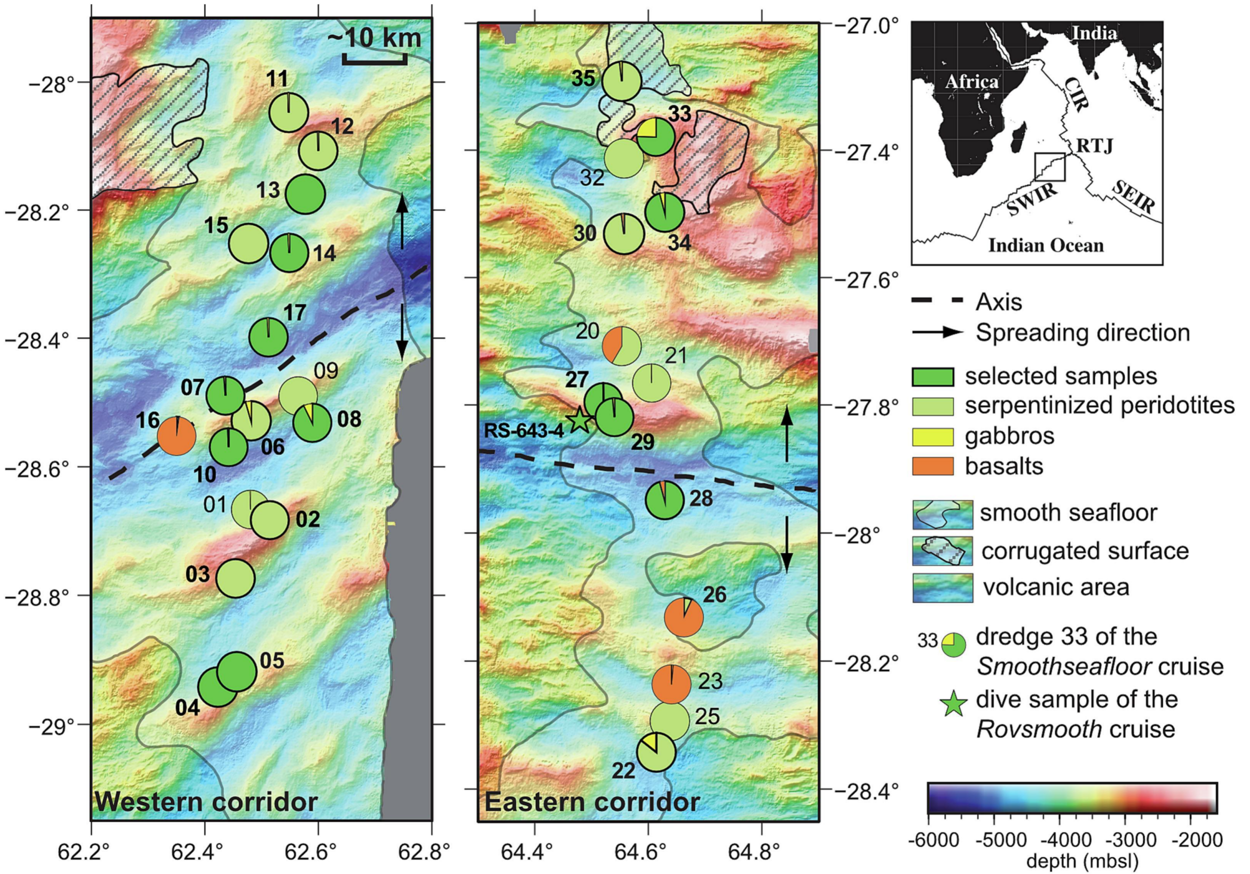

~10 km
Western corridor
Eastern corridor
RS-643-4
Africa
India
CIR
RTJ
SWIR
SEIR
Indian Ocean
Axis
Spreading direction
selected samples
serpentinized peridotites
gabbros
basalts
smooth seafloor
corrugated surface
volcanic area
dredge 33 of the *Smoothseafloor* cruise
dive sample of the *Rovsmooth* cruise
depth (mbsl)
-6000
-5000
-4000
-3000
-2000
62.2°
62.4°
62.6°
62.8°
64.4°
64.6°
64.8°
−28°
−28.2°
−28.4°
−28.6°
−28.8°
−29°
−27.0°
−27.4°
−27.6°
−27.8°
−28°
−28.2°
−28.4°

Figure 1

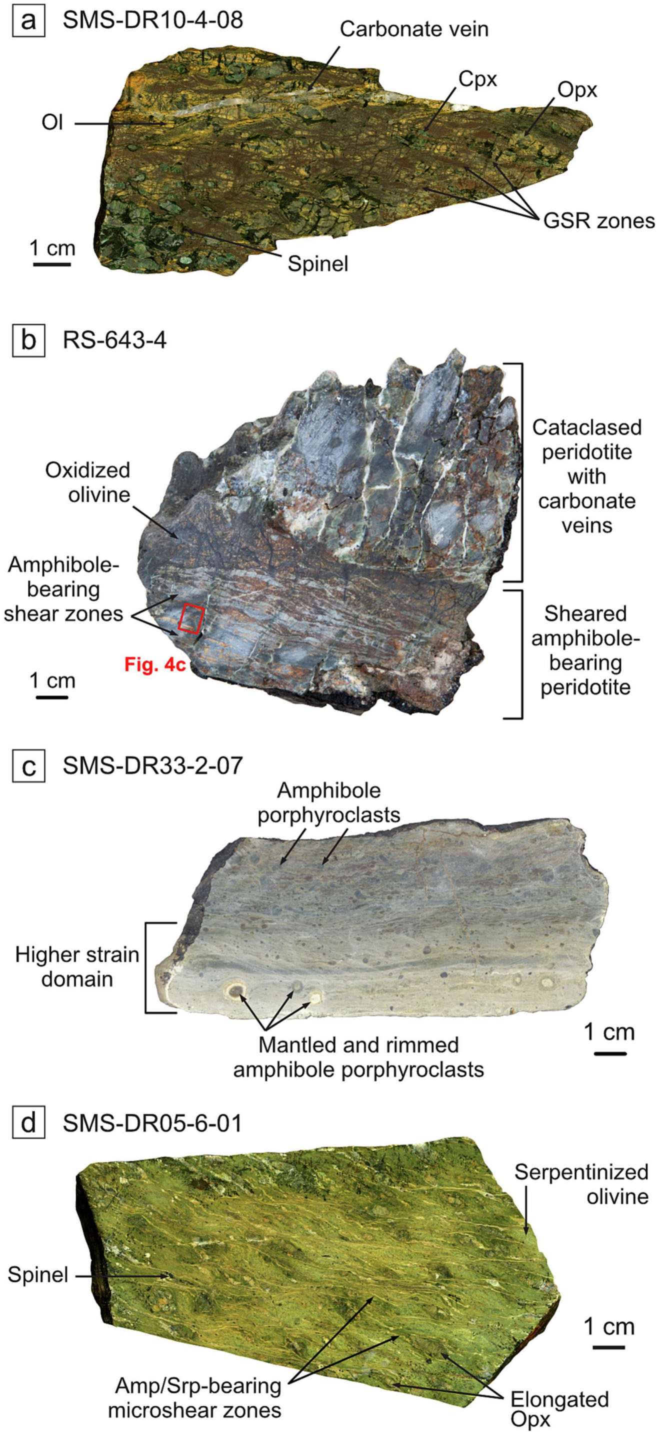
a
SMS-DR10-4-08
Carbonate vein
Cpx
Opx
Ol
GSR zones
1 cm
Spinel
b
RS-643-4
Cataclased peridotite with carbonate veins
Oxidized olivine
Amphibole-bearing shear zones
Sheared amphibole-bearing peridotite
Fig. 4c
1 cm
c
SMS-DR33-2-07
Amphibole porphyroclasts
Higher strain domain
Mantled and rimmed amphibole porphyroclasts
1 cm
d
SMS-DR05-6-01
Serpentinized olivine
Spinel
1 cm
Amp/Srp-bearing microshear zones
Elongated Opx

Figure 2

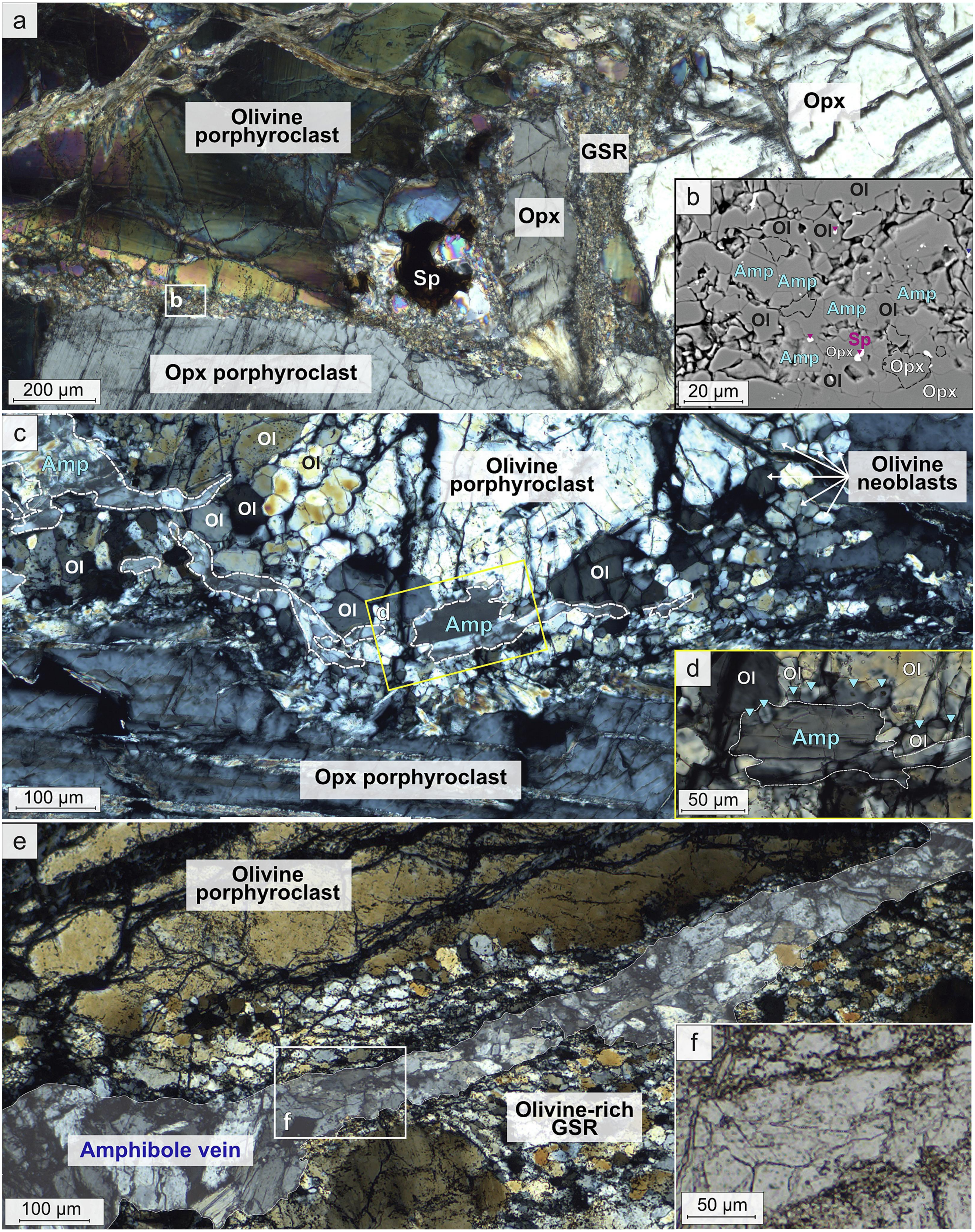
a
Olivine porphyroclast
Opx
GSR
Opx
Sp
b
Opx porphyroclast
200 μm
b
Ol
Ol
Ol
Amp
Amp
Amp
Amp
Ol
Ol
Sp
Amp
Opx
Opx
Ol
Opx
20 μm
c
Amp
Ol
Ol
Olivine porphyroclast
Olivine neoblasts
Ol
Ol
Ol
Ol
Ol
d
Amp
Opx porphyroclast
100 μm
d
Ol
Ol
Ol
Amp
Ol
50 μm
e
Olivine porphyroclast
f
Olivine-rich GSR
Amphibole vein
100 μm
f
50 μm

Figure 3

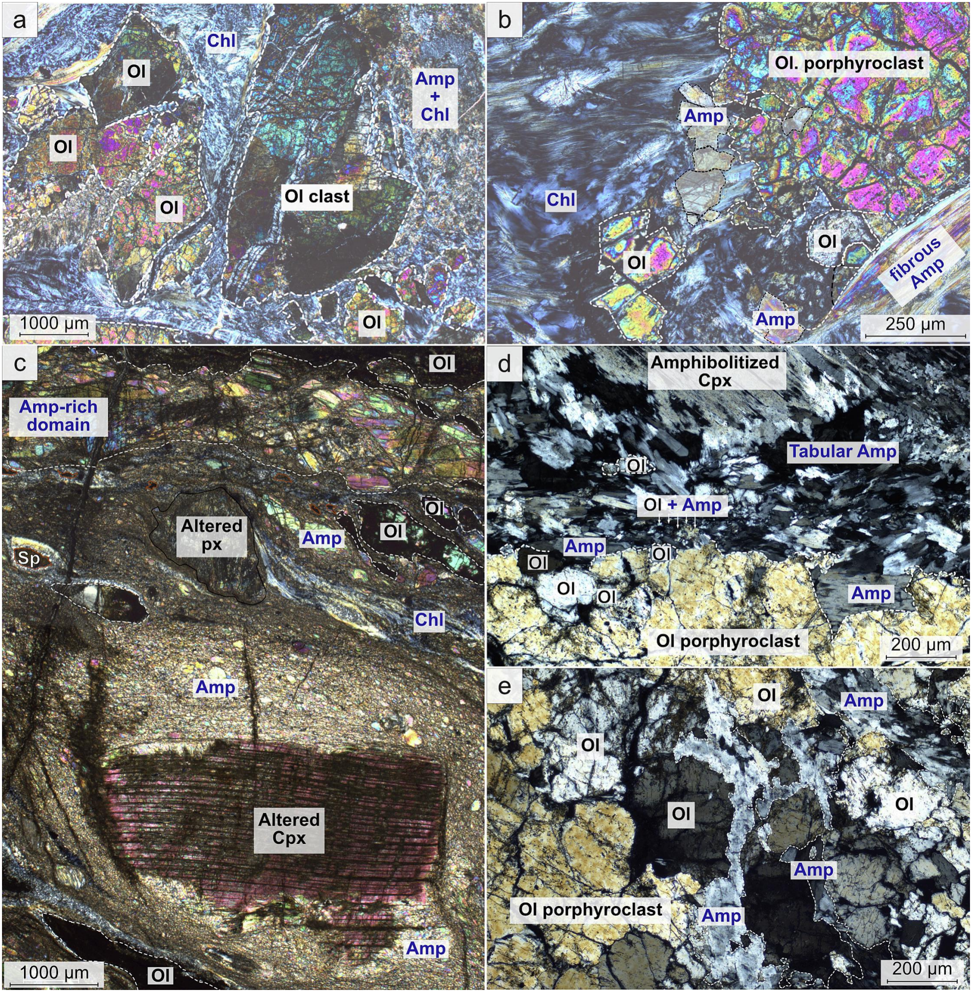

a
Chl
Ol
Amp
+
Chl
Ol
Ol
Ol clast
Ol
1000 μm
b
Ol. porphyroclast
Amp
Chl
Ol
Ol
fibrous
Amp
Amp
250 μm
c
Ol
Amp-rich
domain
Altered
px
Amp
Ol
Ol
Sp
Chl
Amp
Altered
Cpx
Amp
1000 μm
Ol
d
Amphibolitized
Cpx
Tabular Amp
Ol
Ol + Amp
Amp
Ol
Ol
Ol
Ol
Amp
Ol porphyroclast
200 μm
e
Ol
Amp
Ol
Ol
Ol
Amp
Ol porphyroclast
Amp
200 μm

Figure 4

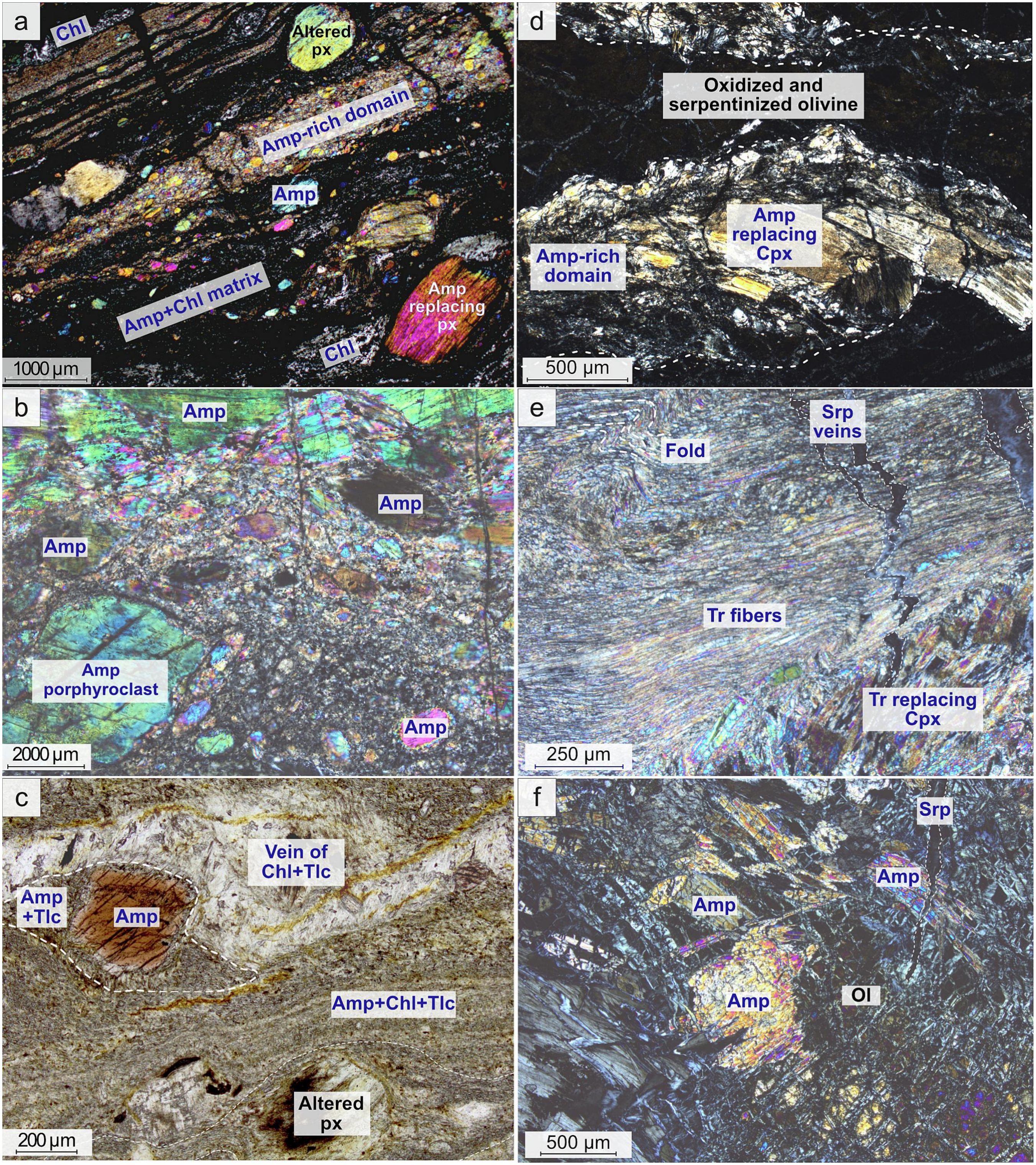
a
Chl
Altered px
Amp-rich domain
Amp
Amp+Chl matrix
Amp replacing px
Chl
1000 µm
d
Oxidized and serpentinized olivine
Amp replacing Cpx
Amp-rich domain
500 µm
b
Amp
Amp
Amp
Amp porphyroclast
Amp
2000 µm
e
Srp veins
Fold
Tr fibers
Tr replacing Cpx
250 µm
c
Vein of Chl+Tlc
Amp +Tlc
Amp
Amp+Chl+Tlc
Altered px
200 µm
f
Srp
Amp
Amp
Amp
Ol
500 µm

Figure 5

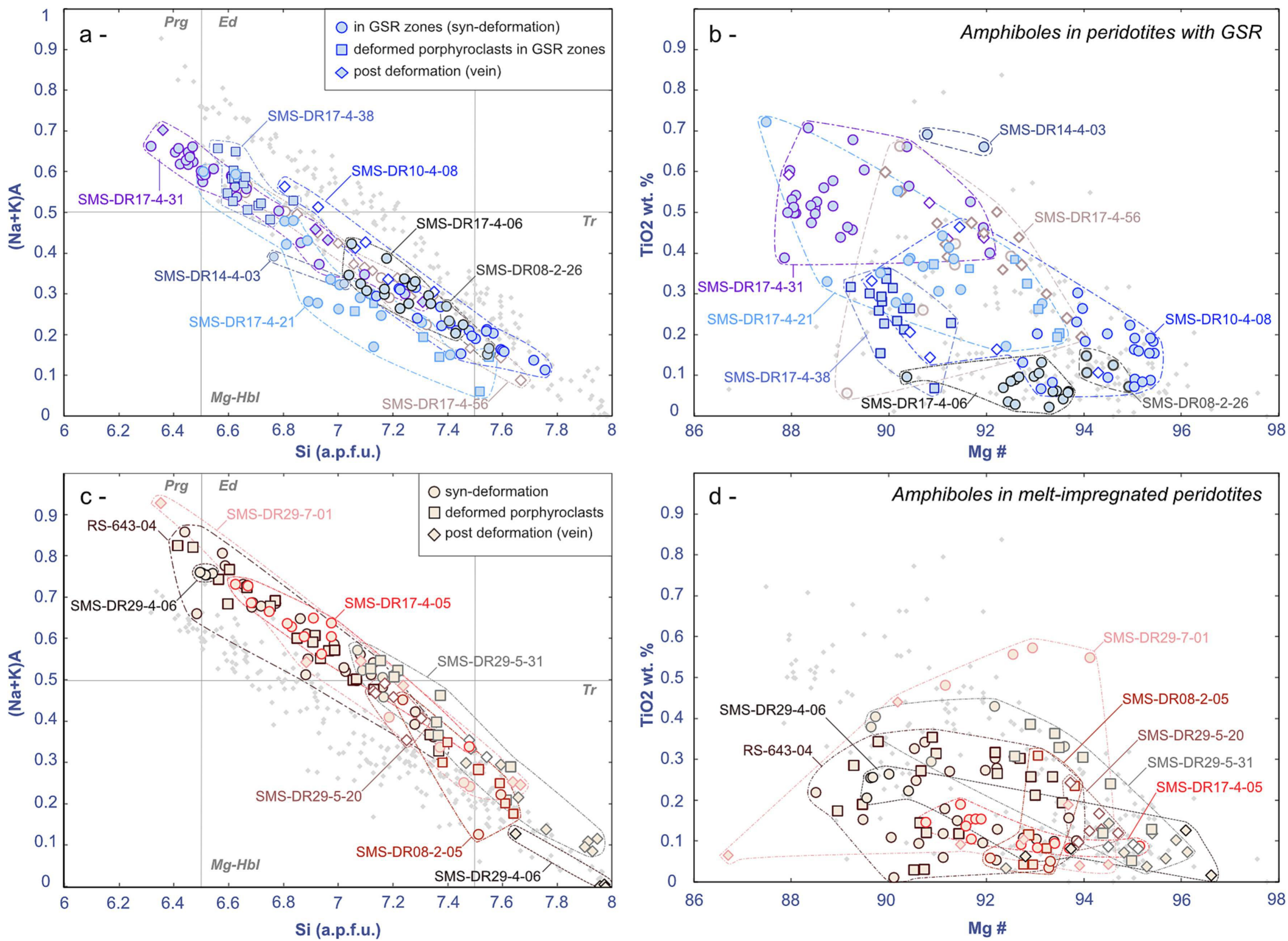

a -
Prg
Ed
Tr
Mg-Hbl
in GSR zones (syn-deformation)
deformed porphyroclasts in GSR zones
post deformation (vein)
SMS-DR17-4-38
SMS-DR10-4-08
SMS-DR17-4-31
SMS-DR17-4-06
SMS-DR14-4-03
SMS-DR08-2-26
SMS-DR17-4-21
SMS-DR17-4-56
(Na+K)A
Si (a.p.f.u.)
b -
Amphiboles in peridotites with GSR
SMS-DR14-4-03
SMS-DR17-4-56
SMS-DR17-4-31
SMS-DR17-4-21
SMS-DR10-4-08
SMS-DR17-4-38
SMS-DR17-4-06
SMS-DR08-2-26
TiO2 wt. %
Mg #
c -
Prg
Ed
Tr
Mg-Hbl
syn-deformation
deformed porphyroclasts
post deformation (vein)
RS-643-04
SMS-DR29-7-01
SMS-DR29-4-06
SMS-DR17-4-05
SMS-DR29-5-31
SMS-DR29-5-20
SMS-DR08-2-05
SMS-DR29-4-06
(Na+K)A
Si (a.p.f.u.)
d -
Amphiboles in melt-impregnated peridotites
SMS-DR29-7-01
SMS-DR29-4-06
SMS-DR08-2-05
RS-643-04
SMS-DR29-5-20
SMS-DR29-5-31
SMS-DR17-4-05
TiO2 wt. %
Mg #

Figure 6

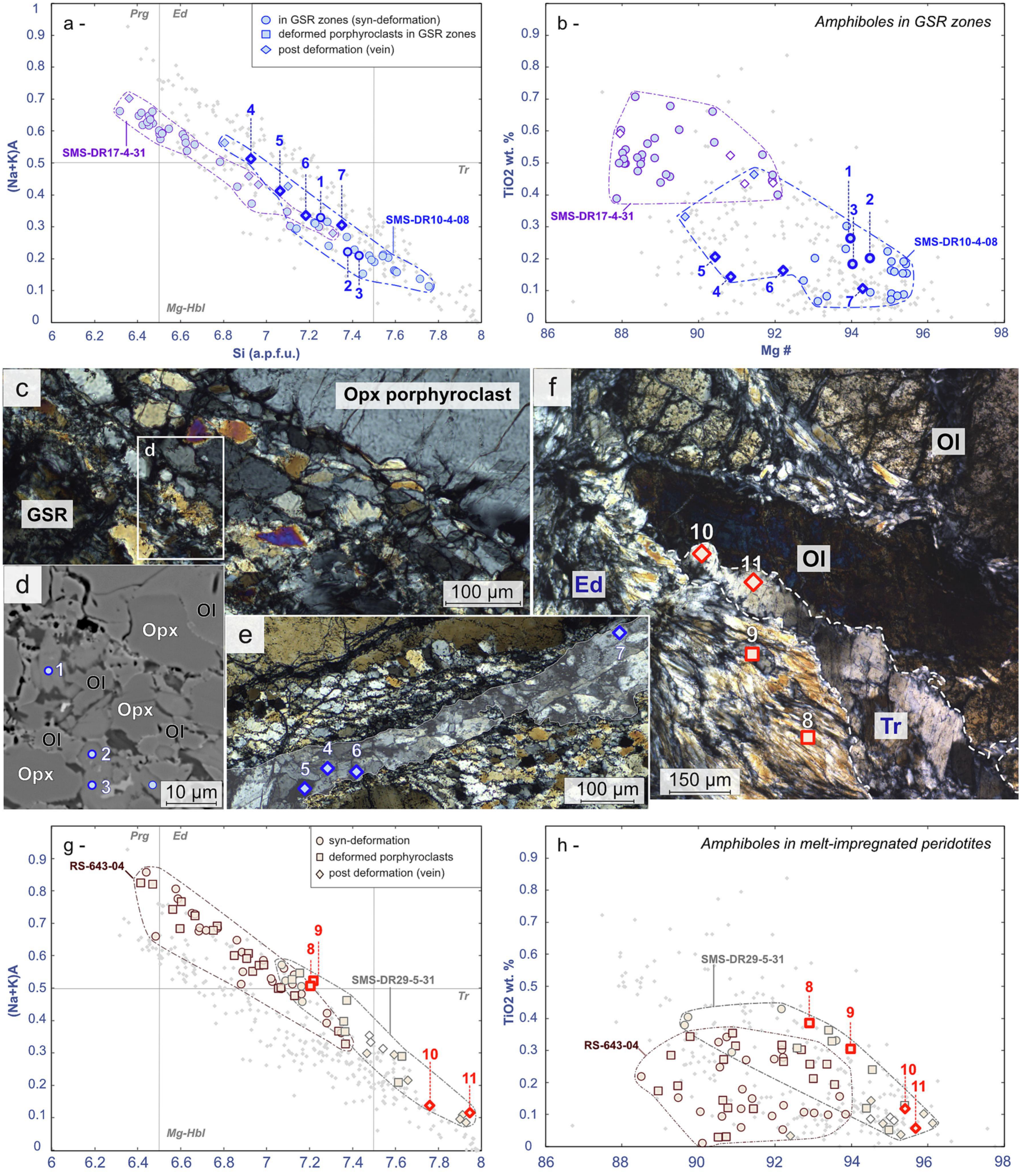

a -
in GSR zones (syn-deformation)
deformed porphyroclasts in GSR zones
post deformation (vein)
Prg
Ed
Mg-Hbl
Tr
SMS-DR17-4-31
SMS-DR10-4-08
(Na+K)A
Si (a.p.f.u.)
b -
Amphiboles in GSR zones
TiO2 wt. %
Mg #
c
Opx porphyroclast
GSR
100 µm
d
Ol
Opx
10 µm
e
100 µm
f
Ol
Ed
Tr
150 µm
g -
syn-deformation
deformed porphyroclasts
post deformation (vein)
RS-643-04
SMS-DR29-5-31
h -
Amphiboles in melt-impregnated peridotites

Figure 7

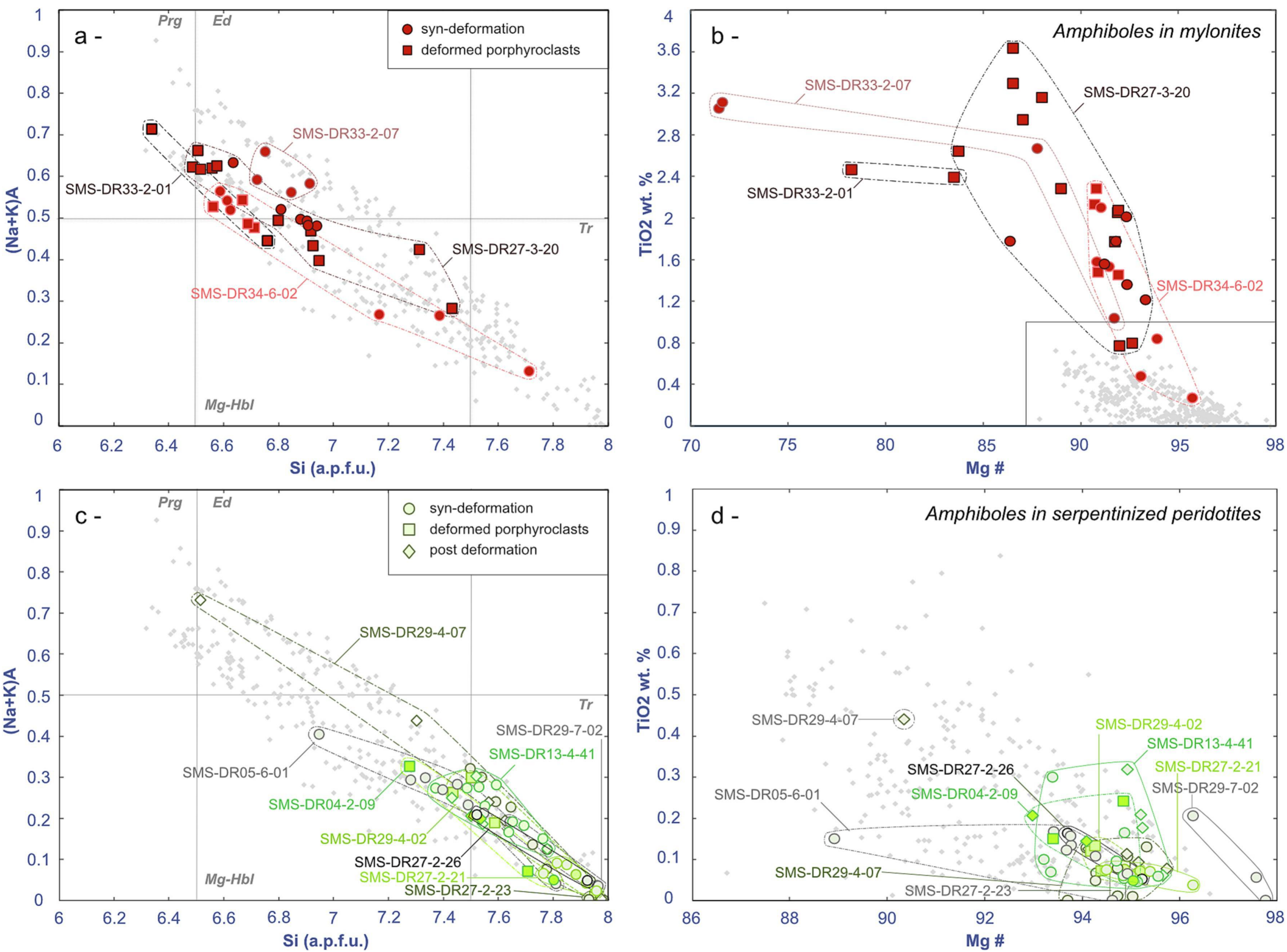

a -
Prg
Ed
Tr
Mg-Hbl
syn-deformation
deformed porphyroclasts
SMS-DR33-2-07
SMS-DR33-2-01
SMS-DR27-3-20
SMS-DR34-6-02
(Na+K)A
Si (a.p.f.u.)
b -
Amphiboles in mylonites
SMS-DR33-2-07
SMS-DR27-3-20
SMS-DR33-2-01
SMS-DR34-6-02
TiO2 wt. %
Mg #
c -
Prg
Ed
Tr
Mg-Hbl
syn-deformation
deformed porphyroclasts
post deformation
SMS-DR29-4-07
SMS-DR29-7-02
SMS-DR13-4-41
SMS-DR05-6-01
SMS-DR04-2-09
SMS-DR29-4-02
SMS-DR27-2-26
SMS-DR27-2-21
SMS-DR27-2-23
(Na+K)A
Si (a.p.f.u.)
d -
Amphiboles in serpentinized peridotites
SMS-DR29-4-07
SMS-DR29-4-02
SMS-DR13-4-41
SMS-DR27-2-26
SMS-DR27-2-21
SMS-DR05-6-01
SMS-DR04-2-09
SMS-DR29-7-02
SMS-DR29-4-07
SMS-DR27-2-23
TiO2 wt. %
Mg #

Figure 8

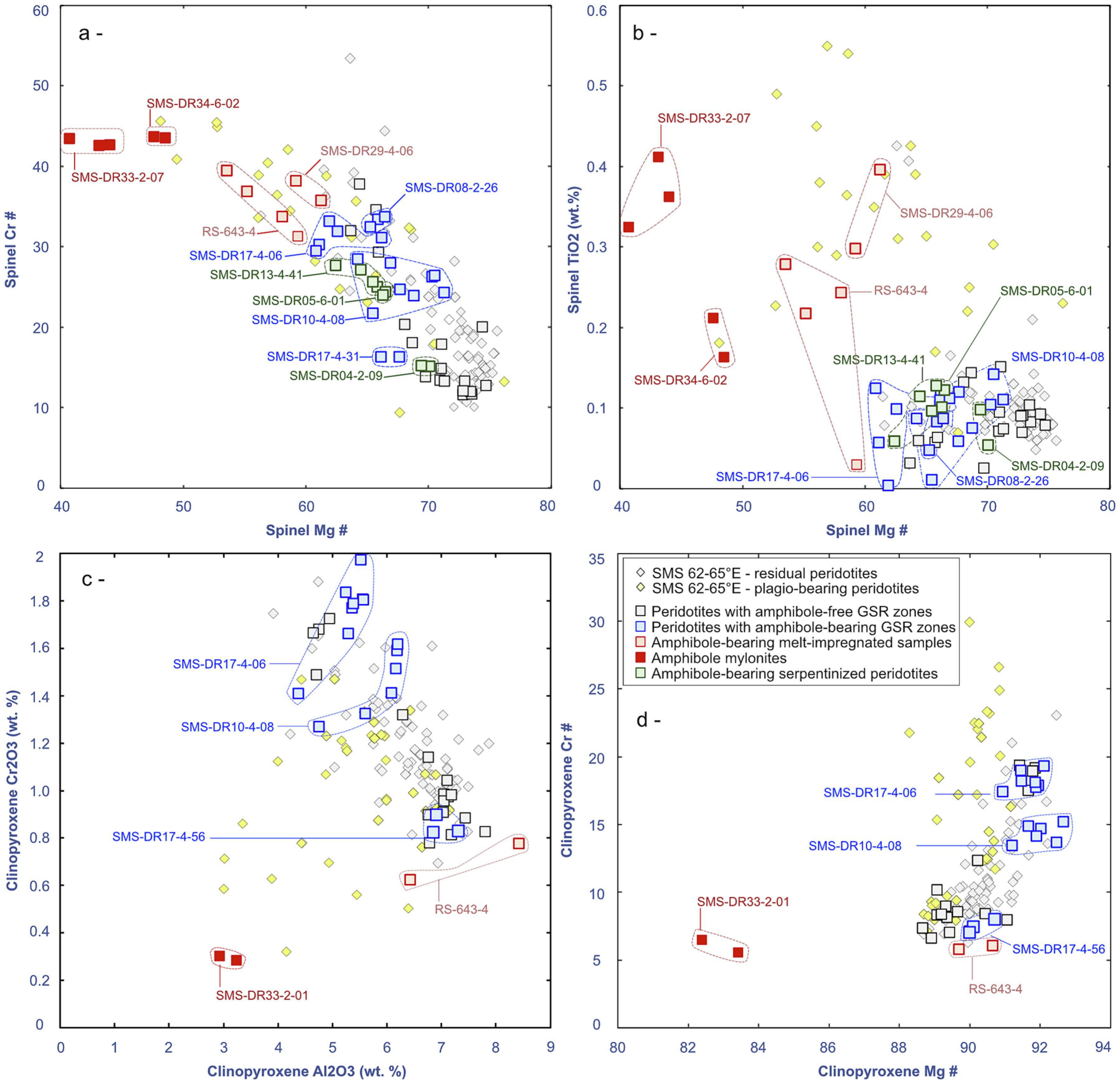
a -
b -
c -
d -
SMS-DR34-6-02
SMS-DR33-2-07
SMS-DR29-4-06
SMS-DR08-2-26
RS-643-4
SMS-DR17-4-06
SMS-DR13-4-41
SMS-DR05-6-01
SMS-DR10-4-08
SMS-DR17-4-31
SMS-DR04-2-09
SMS-DR17-4-56
SMS-DR33-2-01
Spinel Cr #
Spinel Mg #
Spinel TiO2 (wt.%)
Clinopyroxene Cr2O3 (wt. %)
Clinopyroxene Al2O3 (wt. %)
Clinopyroxene Cr #
Clinopyroxene Mg #
SMS 62-65°E - residual peridotites
SMS 62-65°E - plagio-bearing peridotites
Peridotites with amphibole-free GSR zones
Peridotites with amphibole-bearing GSR zones
Amphibole-bearing melt-impregnated samples
Amphibole mylonites
Amphibole-bearing serpentinized peridotites

Figure 9

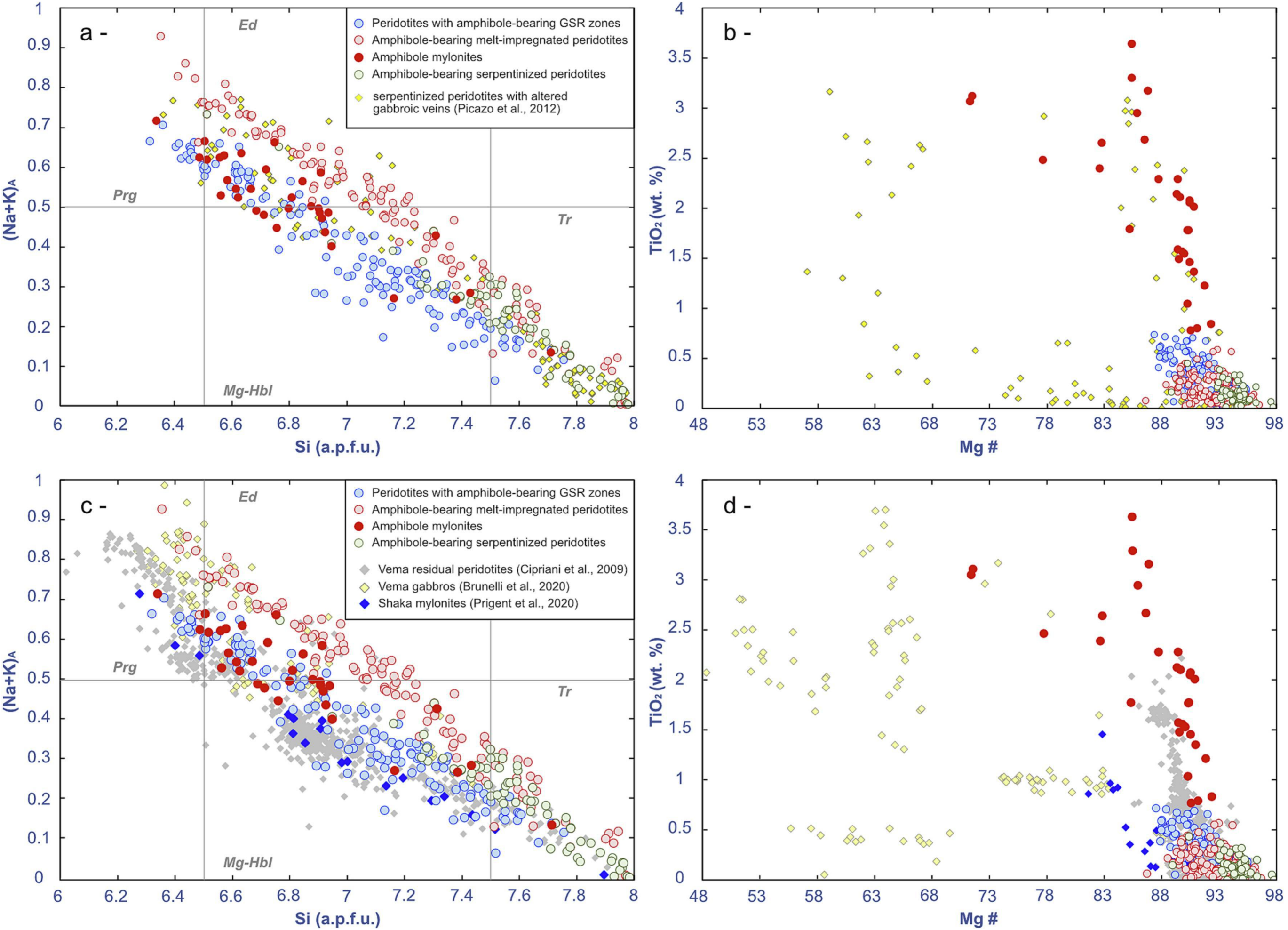
a -
b -
c -
d -
Peridotites with amphibole-bearing GSR zones
Amphibole-bearing melt-impregnated peridotites
Amphibole mylonites
Amphibole-bearing serpentinized peridotites
serpentinized peridotites with altered gabbroic veins (Picazo et al., 2012)
Vema residual peridotites (Cipriani et al., 2009)
Vema gabbros (Brunelli et al., 2020)
Shaka mylonites (Prigent et al., 2020)
Ed
Prg
Tr
Mg-Hbl
(Na+K)A
Si (a.p.f.u.)
TiO2 (wt. %)
Mg #

Figure 10

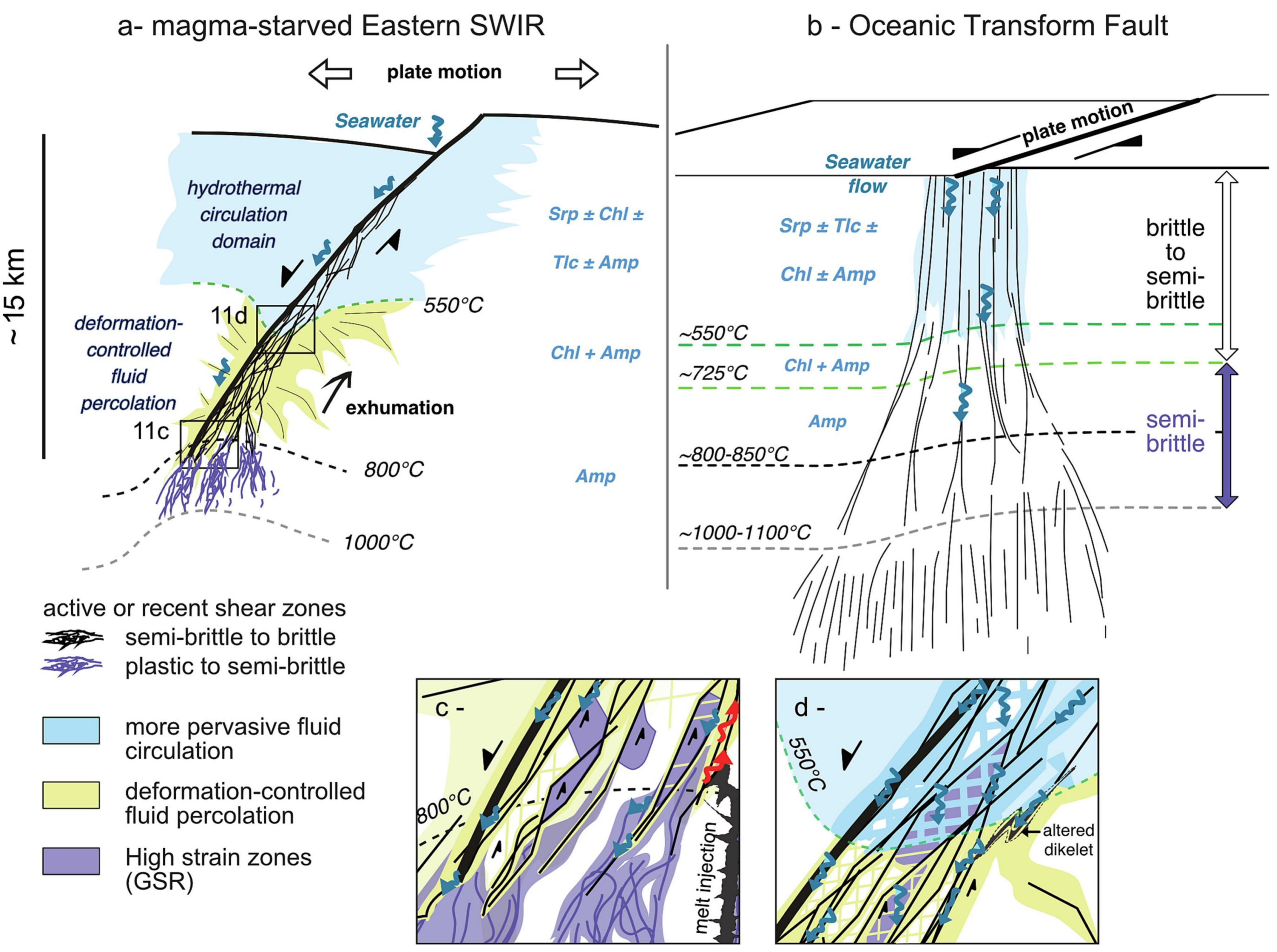

a- magma-starved Eastern SWIR
b - Oceanic Transform Fault
plate motion
Seawater
hydrothermal circulation domain
Srp ± Chl ±
Tlc ± Amp
550°C
11d
deformation-controlled fluid percolation
Chl + Amp
exhumation
11c
800°C
Amp
1000°C
~15 km
plate motion
Seawater flow
Srp ± Tlc ±
Chl ± Amp
brittle to semi-brittle
~550°C
~725°C
Chl + Amp
Amp
semi-brittle
~800-850°C
~1000-1100°C
active or recent shear zones
semi-brittle to brittle
plastic to semi-brittle
more pervasive fluid circulation
deformation-controlled fluid percolation
High strain zones (GSR)
c -
800°C
melt injection
d -
550°C
altered dikelet

Figure 11